ATLAS ELEKTRONIK
A joint company of ThyssenKrupp and Airbus DS

JACOBS UNIVERSITY

# Powerline Transmission System for Underwater Sensor Networks

by

**Vladimir Burstein**

a Thesis submitted in partial fulfillment
of the requirements for the degree of

## Doctor of Philosophy in Electrical Engineering

Approved Dissertation Committee:

**Prof. Dr.-Ing. Werner Henkel**
Jacobs University Bremen

**Dr. rer. nat. habil. Mathias Bode**
Jacobs University Bremen

**Prof. Dr.-Ing. Lutz Lampe**
The University of British Columbia

**Dr.-Ing. Frank Brand**
ATLAS ELEKTRONIK GmbH

Date of Defense: May $15^{th}$, 2017

Computer Science and Electrical Engineering

# Statutory Declaration

(Declaration on Authorship of a Dissertation)

I, Vladimir Burstein hereby declare, under penalty of perjury, that I am aware of the consequences of a deliberately or negligently wrongly submitted affidavit, in particular the punitive provisions of §156 and §161 of the Criminal Code (up to 1 year imprisonment or a fine at delivering a negligent or 3 years or a fine at a knowingly false affidavit).

Furthermore I declare that I have written this PhD thesis independently, unless where clearly stated otherwise. I have used only the sources, the data and the support that I have clearly mentioned.

This PhD thesis has not been submitted for the conferral of a degree elsewhere.

Bremen, May 31, 2017

Signature _____

# Abstract

The major contribution of this work is a novel powerline communication system for underwater acoustical sensor networks. Sonar is the best example of such a network, which has a linear bus topology. There is a number of challenges for a transmission system in this particular application. A high data volume, generated by numerous acoustical sensors, the requirements of high synchronization accuracy and low power consumption, changing channel conditions and a high level of inter-symbol interference, caused by the multi-path nature of a linear bus, are among the problems solved by the suggested multi-carrier transmission system.

Information about the underwater environment is generated by the acoustical sensors. The analysis of the available data sets has shown a pronounced redundancy of this kind of data. Different source coding schemes are proposed to reduce the amount of data to be transmitted. The first step in these methods is the removal of the sample-to-sample correlation. This is done by applying (multidimensional) linear prediction, resulting in un-correlated residuals. Different universal source codes for compression of residuals were studied. The subexponential code was found to be best suited, outperforming the currently used methods.

The underwater environment requires special underwater cabling, which was not well studied before. Using a network analyzer, different cables and cable structures were measured, thus providing real-world characterization of the transmission channel under normal conditions and under high pressure. A cable model was used to simulate the electrical characteristics of standard Cat5e and proprietary underwater cables. Special care was taken in finding the correct model parameters, using a multivariate robust fitting method. The cable structures are consequently modeled applying two-port network theory rules. It was shown that high pressure results in higher attenuation and crosstalk.

Designed as a DC powerline communication system, the exemplary underwater sensor network of a sonar array uses a linear bus topology of the power distribution network for data transmission. An application of time-domain equalization (TEQ) is discussed in this context. Simulations show the advantages of a TEQ-enabled system, both using rate-maximizing or a classical shortening TEQ, in different bus configurations. As a result, the complexity of the corresponding modem implementations could be greatly reduced by using a shorter DFT, while still keeping the high data rate.

Finally, the major system design decisions in the development of a broadband powerline communication sensor network are discussed, with DC power supplies, sensors, and connecting cables located in a harsh environment.

Using an underwater sonar network as an example, the physical layer parameters, system design, and prototype of the new transmission system are introduced.

# Acknowledgments

This work is the result of my industrially focused research project, which was carried out in a collaboration between ATLAS ELEKTRONIK GmbH and the transmission systems group at Jacobs University Bremen.

As such, this work would have been absolutely impossible without the exceptional support of my supervisors Dr.-Ing. Frank Brand and Prof. Dr.-Ing. Werner Henkel. I would like to express my sincere gratitude for their continuous support of my Ph.D. studies and related research, for the patience, motivation, and immense knowledge.

Furthermore, I would like to thank Prof. Dr.-Ing. Lutz Lampe and Dr. rer. nat. habil. Mathias Bode for accepting to join the dissertation committee and their insightful comments and encouragement.

I thank all my fellows and colleagues, both at the transmission systems group and at the company, for valuable discussions and motivation. This would not be such a great time without you.

Finally, I would like to thank my family: my parents, my brothers, and especially my wife, for the enormous patience and incredible support.

# Contents

# Chapter 1

# Introduction

## 1.1 Motivation

The tasks of navigation and the detection of obstacles seem to be not always trivial for a surface vehicle, which can use sources of information in different frequency regions: global navigation satellite systems (e.g. GPS, Galileo, GLONASS), high-frequency radars, eyes and ears of a driver, optical cameras and microphones of a robot. Considering underwater vehicles or ships these tasks become even more complicated: due to an exceptionally high attenuation of signals at higher frequencies, only acoustical signals can provide a reliable source of information about the underwater environment starting at distances of 10-20 m, depending on the water quality. A sonar, which consists of a number of spatially distributed acoustic sensors and operates in a frequency range of a few Hz to hundreds of kHz, is usually the only device capable of sensing the far-field environment under water. The transmission of digitalized acoustic data from outboard sensors to the inboard signal processing units is a serious challenge, as the number of acoustic sensors, the distances between them, and their sampling rate and bit resolution increases. A typical future sonar system consists of hundreds of single sensors producing a data flow of around 10 Mbit/s per node, or 1-2 Gbit/s per system. Such sonar systems do not only mean high data rate and high synchronization requirements (less than 1 $\mu s$) for a data transmission system, but also some mechanical restrictions because of the high pressure conditions under water.

The appropriate data transmission system is forced to be wire-line based. Due to the high attenuation of radio or optical waves under water, a wireless system would be very inefficient [1], especially considering the typical sensor-array lengths of 100 to 500 meters. Furthermore, such a system would have

to deal with a high diversity of channel conditions, because of extremely different water quality (temperature, salinity, turbidity) all over the world. Because of mechanical restrictions, the number of switching nodes (active components) should be kept as small as possible, ideally not using such components outboards at all. It is in fact possible, keeping in mind that the power distribution network, being a linear bus topology, already provides a communication path.

## 1.2 Existing Communication Systems

On the one hand, there are plenty of wire-line transmission systems available on the market, including classical IEEE 802.3 Ethernet [2] and Ethernet-based industrial field bus systems (EtherCAT, ProfiNET to name a few, see [3] for more details), more exotic and application specific ones like SpaceWire [4], or a family of end-user Internet access systems, like Very High Speed Digital Subscriber Line (VDSL) [5]. All these system are point-to-point systems at physical layer, typically utilizing a star, tree, or daisy-chain topology to provide access to multiple peers, using switching nodes.

On the other hand, there are many bus-oriented systems, like FlexRay, RS-485, Multipoint Low-Voltage Differential Signalling (M-LVDS) and Power-Line Communication (PLC). The principles behind PLC conceptually closely matches the above-mentioned requirements, where the others are too low-rate. The commercially available implementations however deal mostly with an in-house AC power wiring (e.g. Homeplug AV, IEEE 1901, G.9960 [6], or a more general approach [7]), which differs greatly from a rather well controlled twisted pair linear bus, in terms of both noise sources and channel attenuation. This potentially results in rather non-optimal power consumption at every node - and of the whole system, especially as the number of nodes grows. All standards typically limit the utilized bandwidth using predefined Power Spectral Density (PSD) masks, because of legal restrictions on using radio frequency spectrum. This is surely a performance limiting factor, especially when using shielded twisted pairs for an underwater cabling system, where the interference with other systems is not an issue. A newer Homeplug AV2 standard [8] has more relaxed bandwidth restrictions (up to 86 MHz) and uses Multiple-Input Multiple-Output (MIMO) technology to improve the performance. It is still, however, designed to be used in 3-wire AC networks, and its usage in a DC-oriented twisted pair infrastructure is therefore non-optimal or even impossible.

Another very promising research direction seems to be the use of PLC solutions for on-board networks on aircrafts [9], [10], [11], ground vehicles

[12], [13], [14], [15], or in mechatronic systems (e.g. robotic) [16], [17]. Common to all these systems is the use of existing (typically DC) low-voltage power distribution network for communication purposes and are all based on Orthogonal Frequency Division Multiplexing (OFDM). Unfortunately, the work in this field mostly concentrates on providing a reliable low throughput (around 10 Mb/s) link, mostly for control data, using the maximum baseband bandwidth of 30 MHz or a passband bandwidth of around 10 MHz [17].

## 1.3 Multi-Carrier Twisted Pair Bus

The ultimate goal of this work is to introduce a full-duplex transmission system, Multi-Carrier Twisted Pair (MC-TP), which achieves the full capacity of a twisted pair linear bus, that is also used to supply power, in an optimal way, with lots of sensors being single nodes on the bus. As the cable system is placed outside a vehicle, this system should adapt to the changing channel conditions, as a result of changing pressure under water or in case of a leakage. The project will carry out research activities, to find a theoretical optimum for a physical Open Systems Interconnection model (OSI) layer, and will try to use these results to scientifically support the development of a real-world prototype in a systematic way. To the best of the author's knowledge, there is no other similar communication system for sensor networks, that provides high throughput, optimal handling of a linear bus channel, and ability to adapt to channel conditions, influenced by environmental factors, like pressure and temperature.

As the name MC-TP suggests, the proposed system uses shielded twisted pair cables, corresponding to at least category 5e of the TIA/EIA-568-B.2 standard, as physical medium, with a differential signaling Physical Interface (PHY). The same cabling should be used as a DC power bus as well, in agreement with actual PLC principles. By optimizing the wiring for both power and data transmission the system is not exactly alike the existing PLC systems, which use a sub-optimum channel of power wiring. Nevertheless, it can be still considered a powerline system, as the data transmission channel is still a compromise due to the power transmission. The twisted pairs are prepared for the underwater use, and are specified to maintain their structure under high pressure (up to 100-200 atm). Nevertheless, it is very hard to impossible to keep the electrical characteristics of wires pressure-independent (see Section 3.4 for more details), so that MC-TP has to detect and adapt to such changes.

Most of above-mentioned wire-line communication systems (but also many

wireless) are based on OFDM (PLC) or Discrete Multi-Tone modulation (DMT) (VDSL). At the time of writing, multi-carrier modulation is the most widely used technology with rather low implementation cost, which achieves a near-capacity performance on frequency-selective channels [18]. It is expected that a linear bus topology with numerous taps results in a very slowly time-varying frequency-selective fading channel, due to its multi-path nature [19]. This will be discussed in more detail in Chapter 3. Thus, using DMT for such a system is a natural choice, helping to deal with a frequency-selective channel without implementing a complicated equalizer.

## 1.4 Document Overview

The well-known diagram in Fig. 1.1 that describes a general digital communication system is a nice starting point to describe the structure of this thesis. Three major topics, marked in the figure, have been extensively studied and will be dealt with in the corresponding chapters of this document. Every chapter starts with the theoretical background for the subject, followed by the research results, which are the main contribution of this work.

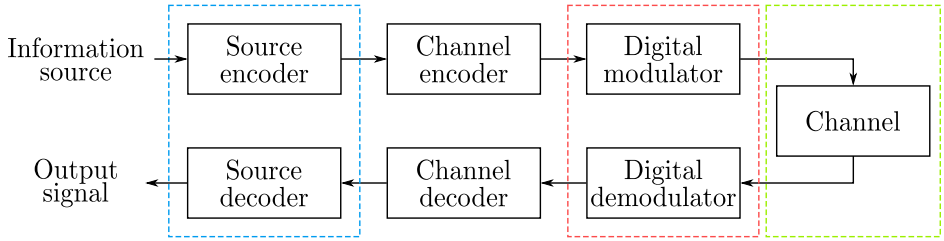


Figure 1.1: Elements of a digital communication system [20]

Generally, source coding is considered to be a very established topic in the communication community. However, the data statistics of some special sources is not well studied and documented – and the data generated by a sonar array is a good example of such an exception. This issue is addressed in Chapter 2, which gives some brief information about sonar array signal processing, linear prediction coding, and variable-length universal source codes. Using the available data from a sonar array, the statistics of acoustical underwater sources is studied and a new compression method based on different variants of linear prediction is introduced.

Using the results of transmission line theory, Chapter 3 concentrates on the characterization and modeling of different types of twisted pair cables and bus structures. Different underwater cable types and bus structures

are measured to obtain cable model parameters and verify the cables' and system's model behavior under different pressure levels for underwater usage – the first study of this kind so far. After investigating the noise sources, the twisted pair channel capacity is calculated using water-filling.

The basics of multi-carrier transmission – including channel partitioning for DMT, the basic concepts behind single-user bit-loading, symbol and sampling frequency synchronization – are provided in Chapter 4. This chapter can be considered to be the state-of-the-art description for the modulation block in Fig. 1.1. The next optimization step for the bus systems is proposed in the Chapter 5, which describes the structure of different types of time-domain equalizers and shows their performance and potential receiver complexity reduction in the multi-user multi-path environment of a DC-PLC sensor network.

This work, supported by ATLAS ELEKTRONIK GmbH, Bremen, would not be complete, if the research results of the previous chapters would not be applied in practice. In parallel to these studies, the architecture of the MC-TP bus and the first transceiver prototype have been developed and are presented in Chapter 6 and are the first step towards the new DC-PLC transmission system, optimized for acoustical sensor networks.

# Chapter 2

# Source Coding for Sonar Data

The purpose of the developed communication system, MC-TP, is to transmit the digitalized data, produced by an array of acoustical sensors. The discrete samples may have natural time and space correlations, such that the transmitted data is expected to be redundant. This chapter concentrates on source coding methods for such sources. The current study is confined to passive sonar arrays described in the first section, but the results can be interesting for any kind of underwater applications.

The source coding process removes the redundancy of the original data, reducing the binary representation size of the compressed data either in a lossless way (the original data can be fully recovered), or discarding some information, generally denoted as lossy compression. The latter is widely used in image, video, or audio applications and the corresponding standards, where the user experience is not affected much by a small loss of data. Text files are, on the contrary, the classical example of an application, which would not tolerate any loss of information and are typically compressed by lossless methods [21].

As one of the requirements for a sonar transmission system is to provide the original sampled (raw) data to a receiver, which performs the signal processing, the research in this project concentrates on the lossless or distortionless coding, further described in the following sections.

## 2.1 Passive Sonar Array

The non-transmitting passive sonar arrays play an important role in localization of sources under water. Particularly in the submarine context, different passive sonars are for tactical reasons the only sources of information during a mission.

In general an array consists of multiple sensors, arranged in a certain way to build the array structure. Most common geometries include linear (Fig. 2.1), circular, and planar (rectangular grid) arrays.

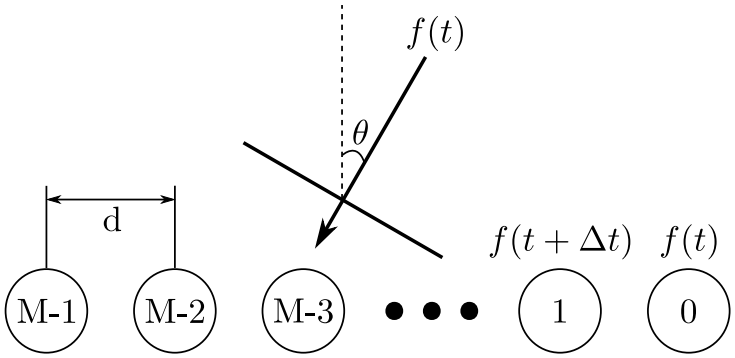


Figure 2.1: Uniform linear array

Using the example of a uniform linear array, widely used in practice (e.g. flank array sonar), the basic signal processing approaches can be explained. A plane wavefront from a single stationary source in Fig. 2.1 arrives at different equidistantly distributed $M$ sensors with an incremental delay $\Delta t$, such that the output of the $s$th sensor ($s \in [0, M-1]$) is $f_s(t) = f(t + s\Delta t)$, assuming $f(t)$ to be a stationary stochastic signal, emitted by the source.

The angle of incidence also known as the direction of arrival (DoA), is the quantity to be estimated[1]. The task of the array signal processing is then to combine the individual sensor outputs, which generally can be corrupted by noise, in an optimum way [22]. A conventional or delay-and-sum beamformer, for example, adds a delay to each input and sums them, thus compensating the sampling delay $\Delta t$ and aligning all signals in time.

The sampled signal from a single sensor can be considered to be a quantized and time-discrete version of the real-valued signal $f(t + s\Delta t)$, which is a time-varying random process. The amount of information or the entropy of this source intuitively depends on the amount of noise and interference: a noiseless case with a single source and constant amplitude represents the minimum non-zero entropy. The opposite case with multiple low amplitude sources in a very noisy environment (or simply the sampled noise) represents the maximum entropy. In other words, the highly correlated samples naturally are more redundant than non-correlated (noisy) samples.

[1]This is the main task of the sonar signal processing, but is less relevant in the scope of this work

## 2.2 Linear Predictive Coding

A well-known assumption of independence and identical distribution (i.i.d.) for a given source is theoretically comfortable, but usually not applicable to the media sources. The statistical dependencies of the input signal are difficult to exploit in an entropy encoder for sources with memory in practice [23]. One of the concepts allowing a rather low complexity solution to this problem is predictive coding.

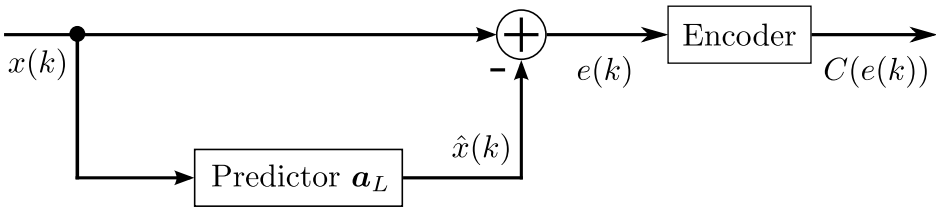


Figure 2.2: Basic structure of lossless predictive coding

The basic idea behind the predictive coding (Fig. 2.2) is to guess the value of the next symbol and to apply an entropy encoding to the difference (also called residual or error) $e(k)$ between the input samples $x(k)$ and their prediction $\hat{x}(k)$[2]

$$e(k) = x(k) - \hat{x}(k) \; . \tag{2.1}$$

Important is that the variance $\sigma_e^2$ of the prediction residual is smaller, compared to the variance $\sigma_x^2$ of the input signal, such that the prediction gain, defined as

$$G_P = \frac{\sigma_x^2}{\sigma_e^2} \; , \tag{2.2}$$

is always bigger than one. Thus, this ratio is the measure of the effectiveness of a prediction.

### 2.2.1 Linear Prediction

Linear prediction is a widely used subclass of predictors, which uses a linear combination of the past values $x(k-i), i \in [1, L]$ to predict the current

[2]Lossy methods usually quantize the value of $e(k)$, before applying an entropy encoding.

sample $x(k)$ [24]. The forward linear predictor [3] of an order $L$ is given by

$$\begin{aligned}\hat{x}(k) &= \sum_{i=1}^{L} a_{L,i} x(k-i) \ , \\ &= \mathbf{a}_L^T \mathbf{x}(k-1) \ ,\end{aligned} \tag{2.3}$$

where $\mathbf{a}_L = [a_{L,1}\ a_{L,2}\ ...\ a_{L,L}]^T$ is a vector, containing $L$ predictor coefficients and $\mathbf{x}(k-1) = [x(k-1)\ x(k-2)\ ...\ x(k-L)]^T$ are the past samples. An optimum linear predictor minimizes the mean-squared error

$$\begin{aligned}MSE(\mathbf{a}_L) &= E\{e^2(k)\} = E\{(x(k) - \hat{x}(k))^2\} \\ &= E\{(x(k) - \mathbf{a}_L^T \mathbf{x}(k-1))^2\} \ .\end{aligned} \tag{2.4}$$

Such a minimization problem can be solved, setting the partial derivatives of the expression in Eq. (2.4) to zero and obtaining a system of linear equations (called normal or Yule-Walker eq.)

$$\mathbf{R}_L \mathbf{a}_L = \mathbf{r}_L \ , \tag{2.5}$$

with $\mathbf{r}_L$ and $\mathbf{R}_L$ defining correlation vector and matrix, respectively, which contain the autocorrelation coefficients $R_{xx}$ of the input signal $x(k)$

$$\begin{aligned}\mathbf{r}_L &= [R_{xx}(1)\ R_{xx}(2)\ ...\ R_{xx}(L)]^T \ , \\ \mathbf{R}_L &= \begin{bmatrix} R_{xx}(0) & R_{xx}(1) & \cdots & R_{xx}(L-1) \\ R_{xx}(1) & R_{xx}(0) & \cdots & R_{xx}(L-2) \\ \vdots & \vdots & \ddots & \vdots \\ R_{xx}(L-1) & R_{xx}(L-2) & \cdots & R_{xx}(0) \end{bmatrix} \ .\end{aligned}$$

In case of backward linear prediction with filter coefficients $\mathbf{b}_L$, the future samples are used, instead of the past, but the normal equations have the same form of

$$\mathbf{R}_L \mathbf{b}_L = \mathbf{J}_L \mathbf{r}_L \ , \tag{2.6}$$

where $\mathbf{J}_L$ is the symmetrical $L \times L$ co-identity matrix, defined as

$$\mathbf{J}_L = \begin{bmatrix} 0 & 0 & \cdots & 0 & 1 \\ 0 & 0 & \cdots & 1 & 0 \\ \vdots & \vdots & \ddots & \vdots & \vdots \\ 0 & 1 & \cdots & 0 & 0 \\ 1 & 0 & \cdots & 0 & 0 \end{bmatrix} \ .$$

[3] The results for the backward prediction will be given without the (analogous) derivations, which can be found, e.g., in [25].

This matrix simply reverses the vector $\mathbf{r}_L$ in Eq. (2.6) and besides can be easily shown to have the property that $\mathbf{R}_L\mathbf{J}_L = \mathbf{J}_L\mathbf{R}_L$ [25].

If the input signal is stationary or locally stationary and not fully deterministic – a valid assumption in sonar signal processing – the correlation matrix is nonsingular (or invertible) and the optimal linear predictor coefficients can be finally determined as

$$\begin{aligned} \mathbf{a}_L &= \mathbf{R}_L^{-1}\mathbf{r}_L \ , \\ \mathbf{b}_L &= \mathbf{R}_L^{-1}\mathbf{J}_L\mathbf{r}_L \ . \end{aligned} \tag{2.7}$$

It is obvious that coefficients for both forward and backward prediction are equal but in reverse order, such that $\mathbf{a}_L = \mathbf{J}_L\mathbf{b}_L$.

The direct method of Eq. (2.7), also called the autocorrelation method, is computationally rather demanding, generally requiring at least $O(L^3) + O(L^2)$ operations, according to [24]. A great complexity reduction can be achieved by exploiting a very regular structure of the correlation matrix $\mathbf{R}_L$, which is in fact a Toeplitz matrix. Robinson, Levinson, and finally Durbin developed a recursive procedure, which requires only $O(L^2)+O(L)$ operations [24] and can be derived as follows.

The minimum mean-squared error (MMSE) $E_L$ for both forward and backward prediction, also called the prediction-error power, can be defined by expanding Eq. (2.4) and using Eq. (2.7) as

$$E_L = R_{xx}(0) - \mathbf{r}_L^T\mathbf{a}_L \ . \tag{2.8}$$

This definition of prediction-error power, combined with Eq. (2.5), results in what is usually called augmented normal equations, given by

$$\begin{aligned} \mathbf{R}_{L+1}\begin{bmatrix} 1 \\ -\mathbf{a}_L \end{bmatrix} &= \begin{bmatrix} E_L \\ \mathbf{0}_{L\times 1} \end{bmatrix} \ , \\ \mathbf{R}_{L+1}\begin{bmatrix} -\mathbf{b}_L \\ 1 \end{bmatrix} &= \begin{bmatrix} \mathbf{0}_{L\times 1} \\ E_L \end{bmatrix} \ , \end{aligned} \tag{2.9}$$

where $\mathbf{R}_{L+1}$ is the augmented correlation matrix

$$\mathbf{R}_{L+1} = \begin{bmatrix} R_{xx}(0) & \mathbf{r}_L^T \\ \mathbf{r}_L & \mathbf{R}_L \end{bmatrix} = \begin{bmatrix} \mathbf{R}_L & \mathbf{J}_L\mathbf{r}_L \\ (\mathbf{J}_L\mathbf{r}_L)^T & R_{xx}(0) \end{bmatrix} \ .$$

To derive the recursive expressions of the Levinson-Durbin algorithm, the augmented normal equations for the forward and backward prediction are first formulated as

$$\mathbf{R}_{L+1}\begin{bmatrix} 1 \\ -\mathbf{a}_{L-1} \\ 0 \end{bmatrix} = \begin{bmatrix} E_{L-1} \\ \mathbf{0}_{(L-1)\times 1} \\ R_{xx}(L) - \mathbf{a}_{L-1}^T\mathbf{J}_{L-1}\mathbf{r}_{L-1} \end{bmatrix} \ , \tag{2.10}$$

and

$$\mathbf{R}_{L+1}\begin{bmatrix}0\\-\mathbf{b}_{L-1}\\1\end{bmatrix}=\begin{bmatrix}R_{xx}(L)-\mathbf{a}_{L-1}^T\mathbf{J}_{L-1}\mathbf{r}_{L-1}\\\mathbf{0}_{(L-1)\times 1}\\E_{L-1}\end{bmatrix}. \tag{2.11}$$

Multiplying Eq. (2.11) by the reflection coefficient, defined as

$$k_L=\frac{1}{E_{L-1}}\left(R_{xx}(L)-\mathbf{a}_{L-1}^T\mathbf{J}_{L-1}\mathbf{r}_{L-1}\right),$$

results in

$$\mathbf{R}_{L+1}\begin{bmatrix}0\\-k_L\mathbf{b}_{L-1}\\k_L\end{bmatrix}=\begin{bmatrix}k_L^2E_{L-1}\\\mathbf{0}_{(L-1)\times 1}\\R_{xx}(L)-\mathbf{a}_{L-1}^T\mathbf{J}_{L-1}\mathbf{r}_{L-1}\end{bmatrix}. \tag{2.12}$$

Subtracting the last equation from Eq. (2.10) gives finally the following expression

$$\mathbf{R}_{L+1}\begin{bmatrix}1\\k_L\mathbf{b}_{L-1}-\mathbf{a}_{L-1}\\-k_L\end{bmatrix}=\begin{bmatrix}(1-k_L^2)E_{L-1}\\\mathbf{0}_{L\times 1}\end{bmatrix}.$$

Comparing this to Eq. (2.9) yields the recursive equations

$$\begin{aligned}\mathbf{a}_L&=-\begin{bmatrix}k_L\mathbf{b}_{L-1}-\mathbf{a}_{L-1}\\-k_L\end{bmatrix}=\begin{bmatrix}\mathbf{a}_{L-1}\\0\end{bmatrix}-k_L\begin{bmatrix}\mathbf{b}_{L-1}\\-1\end{bmatrix},\\E_L&=\left(1-k_L^2\right)E_{L-1}.\end{aligned}$$

The final algorithm has now the following steps

$$\begin{aligned}k_i&=\frac{1}{E_{i-1}}\left(R_{xx}(i)-\mathbf{a}_{i-1}^T\mathbf{J}_{i-1}\mathbf{r}_{i-1}\right),\\\mathbf{a}_i&=\begin{bmatrix}\mathbf{a}_{i-1}\\0\end{bmatrix}-k_i\mathbf{J}_i\begin{bmatrix}-1\\\mathbf{a}_{i-1}\end{bmatrix},\\E_i&=E_{i-1}\left(1-k_i^2\right).\end{aligned} \tag{2.13}$$

Setting the initial value $E_0=R_{xx}(0)$ and evaluating the equations in (2.13) for all $1\leq i\leq L$ results in the optimal coefficients $\mathbf{a}_L$, identical to those directly calculated by Eq. (2.7).

### 2.2.2 Multichannel Linear Prediction

A sonar array is a great example of an application with multiple, possibly highly correlated, channels. The multichannel data can be viewed as a two-dimensional array – with one time and one spatial dimension. It is possible

to apply the previously described linear prediction to both dimensions independently. A better way to take the inter-channel correlation into account is, however, to use the multichannel linear prediction [25].

Adapting Eq. (2.3) from the previous section, the linear prediction residual vector of order $L$ in a multichannel case with $M$ channels is given by

$$\begin{aligned}\hat{\mathbf{x}}_M(k) &= \sum_{i=1}^{L} \mathbf{A}_{L,i}\mathbf{x}_M(k-i) \ , \\ &= \mathbf{A}_L^T \mathbf{x}_{ML}(k-1) \ ,\end{aligned} \tag{2.14}$$

where

$$\begin{aligned}\mathbf{x}_M(k) &= [x_1(k)\ x_2(k)\ ...\ x_M(k)]^T \ , \\ \mathbf{x}_{ML}(k-1) &= \left[\mathbf{x}^T(k-1)\ \mathbf{x}^T(k-2)\ ...\ \mathbf{x}^T(k-L)\right]^T \ , \\ \mathbf{A}_L &= [\mathbf{A}_{L,1}\ \mathbf{A}_{L,2}\ ...\ \mathbf{A}_{L,L}]^T \ .\end{aligned}$$

Following the derivations resulting in equations (2.4) and (2.5), the multichannel version of the normal equations can be shown to be

$$\mathbf{R}_{ML}\mathbf{A}_L = \mathbf{R}_{1/L} \ , \tag{2.15}$$

with the inter-correlation matrix $\mathbf{R}_{1/L}$ and block-Toeplitz covariance matrix $\mathbf{R}_{ML}$ defined as

$$\begin{aligned}\mathbf{R}_{1/L} &= [\mathbf{R}_{xy}(1)\ \mathbf{R}_{xy}(2)\ ...\ \mathbf{R}_{xy}(L)]^T \ , \\ \mathbf{R}_{ML} &= \begin{bmatrix} \mathbf{R}_{xy}(0) & \mathbf{R}_{xy}(1) & \cdots & \mathbf{R}_{xy}(L-1) \\ \mathbf{R}_{xy}(1) & \mathbf{R}_{xy}(0) & \cdots & \mathbf{R}_{xy}(L-2) \\ \vdots & \vdots & \ddots & \vdots \\ \mathbf{R}_{xy}(L-1) & \mathbf{R}_{xy}(L-2) & \cdots & \mathbf{R}_{xy}(0) \end{bmatrix} \ .\end{aligned}$$

The main building block of these matrices is a cross-correlation matrix $\mathbf{R}_{xy}(i)$, which contains autocorrelation coefficients along the main diagonal and generally might not be symmetrical

$$\mathbf{R}_{xy}(i) = \begin{bmatrix} R_{x_1x_1}(i) & R_{x_1x_2}(i) & \cdots & R_{x_1x_M}(i) \\ R_{x_2x_1}(i) & R_{x_2x_2}(i) & \cdots & R_{x_2x_M}(i) \\ \vdots & \vdots & \ddots & \vdots \\ R_{x_Mx_1}(i) & R_{x_Mx_2}(i) & \cdots & R_{x_Mx_M}(i) \end{bmatrix} \ .$$

Similar to Eq. (2.7), the predictor matrix $\mathbf{A}_L$ of size $ML \times M$ can be directly calculated, if the matrix $\mathbf{R}_{ML}$ is nonsingular. It is also possible to reduce the computation cost by applying a generalization of the Levinson-Durbin algorithm to the multichannel case [25].

## 2.3 Source Codes for Memoryless Sources

Besides a predictor, an entropy encoding, shown in Fig. 2.2, is another key component of the (linear) predictive coding. A source symbols sequence (e.g. outcomes of a discrete random process $\mathbf{x} = [x_1\ x_2\ ...]$), generated by the predictor and assumed to have zero inter-symbol correlation, is mapped to a sequence $C(\mathbf{x})$ of codewords, such that the coded message is usually shorter than the original digital representation.

### 2.3.1 Entropy and Redundancy

It is essential to define a reasonable information measure, to be able to qualify a code $C$ and understand its redundancy. Information theory considers the concept of entropy as such an information measure. A common definition (e.g. [26]) of the entropy for a discrete random variable $X$ with a finite alphabet $\chi$, measured in bits, is

$$H(X) = -\sum_{x\in\chi} p(x)\log_2(p(x))\ , \tag{2.16}$$

with $p(x)$ being the probability $\Pr\{X = x\}$ that $x$ is the random outcome of $X$ for all possible $x$ in the alphabet. For some finite source sequence, where the probability distribution is fixed, the entropy is a lower bound for the average length of a code (in bits per sample)

$$L_C(X) = \sum_{x\in\chi} p(x) l_{C(x)}\ , \tag{2.17}$$

with $l_{C(x)}$ being the length of a corresponding codeword. The code is optimal, if the average code length is equal to the entropy of the sequence – also meaning the redundancy to be zero. The ideal length of an individual codeword is then given by

$$l^{id}_{C(x)} = \log_2\left(\frac{1}{p(x)}\right)\ . \tag{2.18}$$

### 2.3.2 Variable-Length Universal Codes

The basic idea behind any entropy encoding is to map fixed-length input symbols to variable-length codewords, such that the most probable source symbols become the shortest codes. The Huffman code is a classical example of an asymptotically optimum entropy code. This variable-length code is used in many applications (e.g. JPEG or MP3), especially if no assumptions about

the probability distribution can be made. The PMF of the source is then either estimated once or block-by-block (adaptive) in the first coding step, followed by the Huffman codeword tree generation, based on the estimated symbol frequencies. More details about Huffman codes and another very popular form of entropy coding – arithmetic coding – can be found in [27] or [28].

In contrast to Huffman or arithmetic coding, universal codes can be used without the exact knowledge of the PMF, if the ranking of symbols' priorities is non-increasing and known a priori. A universal code assumes some fixed probability distribution, such that encoding and decoding complexities are quite low. However, the code is only optimum, if the assumed distribution matches the actual one of the source symbols. Observing Eq. (2.18), this can be formulated as

$$2^{-l_{C(x)}} \stackrel{!}{=} p(x) \; . \tag{2.19}$$

The residuals of the linear prediction usually have a quite static decreasing PMF, close to a geometric distribution, with large values being less probable, providing a good potential for different types of parametrized universal codes, described in the following sections.

### Prefix Codes

A general variable-length encoder can be rather easily implemented – it just replaces the source symbols by the corresponding codewords, using a static table or computing the codes dynamically. These codewords are then concatenated and build the output bit stream.

Even assuming that the code is uniquely decodable (e.g. has unique codewords for each symbol in the alphabet), a decoder is intuitively slightly more complex. Because the codewords have different lengths, it has to know either where each codeword ends or their individual lengths. An important prefix property of the practical variable-length codes states that no codeword is the prefix of any other codeword. The simplification of decoding for such prefix-free codes results from the fact that the decoder does not have to evaluate the bit stream any further to decode the current symbol, as soon as it has recognized a single codeword.

The unary code $C_U(s)$ of an integer $s$ is a classical example of prefix-free codes. It encodes a positive integer $s$ as $s$ bits of value 1, followed by a zero bit, i.e. $C_U(0)$='0', $C_U(1)$='10', $C_U(2)$='110', $C_U(3)$='1110', some other examples can be found in Table 2.1. Also the equivalent bit-inverted version of this code can be used. The 0 at the end of all the codewords acts as a separator, such that the unary code can also be called comma code. The length of a unary codeword is $l_{C_U(s)} = s + 1$ bits, such that this code

is optimum for a source distribution $p(s) \approx 2^{-l_{C_U(s)}} = 2^{s+1}$, according to Eq. (2.19). This means that the unary code has redundancy comparable to the Huffman code for the sources with exponential probability distribution [28].

Although rarely used alone, the variable-length unary code is an important part of other codes, described below.

### Golomb-Rice Codes

The original Golomb family of universal codes was proposed for sources with a geometric distribution [29] and uses a single parameter $m$ to better match the actual distribution of the source. Generally, to encode a positive integer $s$, it is first divided by $m$ and the result is rounded to an integer $q$, which represents the quotient information (number of times, $m$ fits into $s$). The rest information (the remainder $r$) is an integer less than $m$ and thus can be represented in $\log_2 q$ bits as a fixed-length binary number. The two-fold quotient/remainder (prefix/suffix) structure is very common for universal codes in general and particularly for the other codes in this section.

Even though the variable-length unary code is used for $q$, the complete codeword keeps the constant length for all values of $s$ within some range, until the remainder $r$ gets zero. This is the reason for the piecewise uniform distribution function of the codeword lengths with each part distributed geometrically (e.g. shown below in Fig. 2.13). Obviously, the parameter $m$ controls the length of the uniform pieces – number of codewords in a *code bank* – and thus their distribution.

More precisely, in the Golomb-Rice code a source symbol $s$ (a non-negative integer) is mapped to a bit-valued codeword $C_G(s, m)$ in two steps, corresponding to prefix and suffix parts (see Fig. 2.3):

- The **prefix part** of a Golomb code is the value of the quotient

$$q = \left\lfloor \frac{s}{m} \right\rfloor ,$$

  encoded in the unary fashion as a $q + 1$ bits long $C_U(q)$

- The **suffix part** consists of the remainder

$$r = s - mq ,$$

  coded as an unsigned integer in binary representation (denoted here as a beta code $C_\beta(r)$) with a bit-length $l_{C_\beta}$ depending on the value of $m$. If $m$ is a power of 2, then the remainder will always be represented

by $\log_2(m)$ bits and has a constant length $l_{C_\beta} = \log_2(m)$. Otherwise the encoding (and decoding) is more complicated and codeword length depends on the value of $r$. Let $c = \lceil \log_2 m \rceil$ bits, which would be the upper bound to accommodate all possible values of $r$. It is possible, though, to use one bit less for the values of $r$ between 0 and $2^c - m$ (corresponding to the binary range of $\lfloor \log_2 m \rfloor$ bits), such that

$$\begin{aligned} l_{C_\beta(r)} &= c - 1, && r \in [0,\ 2^c - m]\ ; \\ l_{C_\beta(r)} &= c, && r \in [2^c - m + 1,\ 2^c - 1]\ , \end{aligned}$$

A final $m$-parameter Golomb codeword for a symbol $s$ is the concatenation of prefix and suffix parts $C_G(s, m) = \{C_U(q),\ C_\beta(r)\}$, as shown in Fig. 2.3.

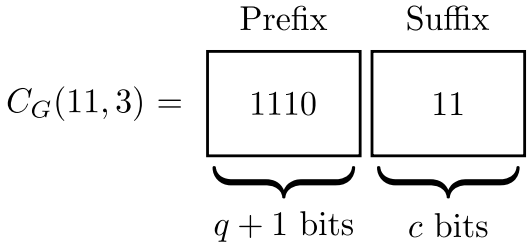


Figure 2.3: Golomb code example with $s = 11$ and $m = 3$. The quotient value for prefix is calculated as $q = \left\lfloor \frac{11}{3} \right\rfloor = 3$, resulting in the unary code '1110'. The remainder for the suffix is $r = 11 - 3 * 3 = 2$. Choosing $m = 3$ yields $c = 2$, such that $r = 2 \in [2^2 - 3 + 1,\ 2^2 - 1]$, and the binary code of $r + 1$ of length $c = 2$ bits for the suffix is given by '11'.

The decoding is again quite straightforward, if $m$ is a power of 2. Starting from the left, the ones in $C_G(s, m)$ are counted, until a zero bit occurs. The number of ones corresponds to the value of $q$. As the value of $m$ is known to the decoder and the codeword has the fixed length of $q + 1 + \log_2(m)$, it assigns $\log_2(m)$ bits after the first zero to $r$. The original symbol is then easily decoded as $\hat{s} = mq + r$.

A slightly more complicated case of non-integer $\log_2(m)$ is decoded in a similar way. The value of $q$ is exactly known after counting the leading ones. A preliminary value of $r$ is calculated from the $c - 1$ bits following the zero delimiter bit. If $r < 2^c - m$, then the total length of the codeword is $q + 1 + (c - 1)$ bits and the value of $r$ is correct. Otherwise, the codeword is $q + 1 + c$ bits long, such that the integer value of $r$ is recalculated, adding one additional bit from the input stream to the already assigned $c - 1$ bits. The final decoding step $\hat{s} = mq + r$ is identical in both cases.

Obviously, a great simplification of the original Golomb code can be achieved by choosing the parameter $m = 2^k$ for some non-negative $k$. In

| $s$ | $C_U(s)$ | $C_\beta(s)$ | $C_G(s,2)$ | $C_G(s,3)$ | $C_G(s,4)$ |
|---|---|---|---|---|---|
| 0 | 0 | 0 | 0\|0 | 0\|0 | 0\|00 |
| 1 | 10 | 1 | 0\|1 | 0\|10 | 0\|01 |
| 2 | 110 | 10 | 10\|0 | 0\|11 | 0\|10 |
| 3 | 1110 | 11 | 10\|1 | 10\|0 | 0\|11 |
| 4 | 11110 | 100 | 110\|0 | 10\|10 | 10\|00 |
| 5 | 111110 | 101 | 110\|1 | 10\|11 | 10\|01 |
| 6 | 1111110 | 110 | 1110\|0 | 110\|0 | 10\|10 |
| 7 | 11111110 | 111 | 1110\|1 | 110\|10 | 10\|11 |

Table 2.1: Some alpha, beta and Golomb-Rice codes

this case the second part of the Golomb code, $C_\beta(r)$, does not need any additional calculations, it is simply the $k$ least significant bits of the binary representation of $s$, as can be seen in Table 2.1. The length of a codeword $C_R(s,2^k) = \{C_U(q),\ C_\beta(r)\}$ is then $l_{C_R(s,2^k)} = 1 + k + \left\lfloor \frac{s}{2^k} \right\rfloor$ and the average length for a random variable $X$ can be calculated by Eq. (2.17).

This was recognized by Rice in [30], who developed an algorithm for such codes, now known as Golomb-power-of-2 (GPO2), Golomb-Rice, or simply Rice codes. Because of its implementation simplicity, this kind of codes is widely used in various applications (e.g. JPEG-LS), but even more frequently for audio compression (Shorten, FLAC, and MPEG-4 ALS to name a few). The Laplace distribution of the residuals, produced by a linear predictor in these audio-codecs, motivates the usage of Rice codes, known to be suitable for this type of distributions [21].

The uniform pieces (code banks) of the codeword length distribution have a constant number of codewords ($2^k$) and start at minimum length of $k+1$. The difference between two neighboring uniform steps is exactly one bit. This results from the truncation of the length $l_{C_R(s,2^k)} = 1 + k + \left\lfloor \frac{s}{2^k} \right\rfloor$, which increases by one each time $s$ is a power of 2.

The optimum parameter for a Rice code $C_R(s,2^k)$ can be shown to be dependent on the mean value $\mu_s$ of the input sequence

$$\hat{k}_f(\mu_s) = \max\{0, \lfloor \log_2(\mu_s + f) \rfloor\}\ , \tag{2.20}$$

with $f \approx 0.382$ for purely geometric sources. The complete derivation of this approximation (original paper suggest an exhaustive evaluation of the average code length for different $k$) and the performance for different distributions is given in [31]. The examples of both codes with different parameter values can also be found in [21].

### Exp-Golomb Codes

The Golomb codes as well as the Rice codes provide quite effective low redundancy coding for geometric (e.g. Laplace) distribution sources. However, changes in the source distribution can lead to a very quick redundancy growth. The more robust parametrized Exp-Golomb codes (also called Elias-Teuhola [32]) have a very similar structure to the Golomb codes and supposed to better fit exponential sources:

- The variable-length **prefix part** is a unary code of

$$d = \left\lfloor \log_2 \left(1 + \frac{s}{2^k}\right) \right\rfloor \ .$$

- The **suffix part** of the length $d+k$ bits is the binary representation of

$$r = s - 2^k \left(2^d - 1\right) \ , \quad r \in \left[0, 2^{d+k}\right] \ .$$

  This part has constant length if $d$ does not change. Similar to the suffix of the Golomb-Rice code, it represents the "rest" information (remainder), not included in $d$.

The decoding of this code is very straightforward and similar to the Rice code. Counting ones from the left until the first zero bit appears yields the value of $d$. The following $k+d$ bits are then the binary representation of $r$. The value if $s$ can now be calculated as $\hat{s} = r + 2^k \left(2^d - 1\right)$.

The length of a codeword $C_{EG}(s, 2^k) = \{C_U(d),\ C_\beta(r)\}$ is given by $l_{C_{EG}(s,2^k)} = 1 + k + 2\left\lfloor \log_2 \left(1 + \frac{s}{2^k}\right)\right\rfloor$. Due to truncation of the logarithm, the length increases by 2 (logarithmically) each time $s$ is a power of 2. Unlike the Rice code, the uniform pieces of the codeword length distribution are not of the constant size and grow with $s$, as can be seen in Table 2.2.

The exponential source distribution is the optimum for this code but it is much more robust to deviations than the Rice code, as shown in [33]. Similar to the Rice codes, Eq. (2.20) provides an estimate for the parameter $k$.

### Subexponential Codes

The subexponential codes may seem to be just another set of Rice codes. They also depend on a non-negative parameter $k$ and consist of two parts. In contrast to the previous codes, all integer symbols with values smaller than $2^k$ are coded in binary and mapped to fixed-length codewords of length $l_{C_{SE}(s,k)} = k + 1$. For larger values of $s$ the code length increases logarithmically, similar to the Exp-Golomb code.

| $s$ | $C_{EG}(s,0)$ | $C_{EG}(s,1)$ | $C_{EG}(s,2)$ | $C_{SE}(s,1)$ | $C_{SE}(s,2)$ | $C_{SE}(s,3)$ |
|---|---|---|---|---|---|---|
| 0 | 0 | 0\|0 | 0\|00 | 0\|0 | 0\|00 | 0\|000 |
| 1 | 10\|0 | 0\|1 | 0\|01 | 0\|1 | 0\|01 | 0\|001 |
| 2 | 10\|1 | 10\|00 | 0\|10 | 10\|0 | 0\|10 | 0\|010 |
| 3 | 110\|00 | 10\|01 | 0\|11 | 10\|1 | 0\|11 | 0\|011 |
| 4 | 110\|01 | 10\|10 | 10\|000 | 110\|00 | 10\|00 | 0\|100 |
| 5 | 110\|10 | 10\|11 | 10\|001 | 110\|01 | 10\|01 | 0\|101 |
| 6 | 110\|11 | 110\|000 | 10\|010 | 110\|10 | 10\|10 | 0\|110 |
| 7 | 1110\|000 | 110\|001 | 10\|011 | 110\|11 | 10\|11 | 0\|111 |
| 8 | 1110\|001 | 110\|010 | 10\|100 | 1110\|000 | 110\|000 | 10\|000 |
| 9 | 1110\|010 | 110\|011 | 10\|101 | 1110\|001 | 110\|001 | 10\|001 |
| 10 | 1110\|011 | 110\|100 | 10\|110 | 1110\|010 | 110\|010 | 10\|010 |
| 11 | 1110\|100 | 110\|101 | 10\|111 | 1110\|011 | 110\|011 | 10\|011 |

Table 2.2: Some Exp-Golomb and Subexponential codes

- The variable-length **prefix part** is either zero, if $s < 2^k$, or otherwise a unary code of $d$

$$d = \left\lfloor \log_2 \left( \frac{s}{2^{k-1}} \right) \right\rfloor \ , \quad s \geq 2^k \ .$$

- The **suffix part** has the same dependency on the value of $s$ as the prefix: it is either the $k$ bits long binary representation of $s$ if $s < 2^k$, or $d + k - 1$ bits long remainder $r$:

$$r = s - \left(2^{d+k-1}\right) \ , \quad s \geq 2^k \ .$$

  Similar to the Exp-Golomb code, this remainder has constant length if $d$ does not change.

Hence, the structure of the codewords is slightly more complicated, than the previous codes and depends on the value of $s$:

$$\begin{aligned} C_{SE(s,k)} &= \{'0', C_\beta(s)\} \ , & s < 2^k \ ; \\ C_{SE(s,k)} &= \{C_U(d), C_\beta(r)\} \ , & s \geq 2^k \ . \end{aligned}$$

Consequently, the codeword lengths are then given by

$$\begin{aligned} l_{C_{SE}(s,k)} &= k + 1 \ , & s < 2^k \ ; \\ l_{C_{SE}(s,k)} &= 2d + k \ , & s \geq 2^k \ . \end{aligned}$$

As a consequence of this two-fold structure, also the optimal source distribution consists of two parts: the uniform part for the sample values smaller than $2^k$ corresponds to the uniform distribution due to the fixed length of the codewords; the exponential part for the $s \geq 2^k$ behaves exactly like the Exp-Golomb codes.

Despite the more complicated structure of the subexponential code, the decoding is as simple as for the Exp-Golomb codes. If the left topmost bit is zero, the $k$ following bits represent the sample value $s$. Otherwise, the decoding is exactly the same as for the Exp-Golomb code, because all the other codewords start with at least one non-zero bit ($d > 0$).

### Start-Step-Stop Codes

The Start-Step-Stop codes can be considered a generalization of the variable-length codes, introduced above, with three non-negative parameters: *Start*, *Step*, and $Stop = Start + k_{max} \cdot Step$ [34]. The codes are organized in code banks, with $k \in [0, k_{max}]$ being a bank number. The typical two-parts code structure in every bank consists of a unary coded $k$ as a prefix and of a suffix that contains the $Start + k \cdot Step$ least significant bits of a source symbol $s$. The parameters *Start* and $k_{max}$ control the starting and the maximum suffix length, respectively. The parameter *Step* specifies how many bits ($2^{Step}$) are added to the suffix length at every code bank $k$[4]. Following these rules, the parameter triplet $k$,0,$\infty$ generates the Rice codes (they add exactly $2^0 = 1$ bit at every code bank), whereas $k$,1,$\infty$ – the Exp-Golomb codes ($2^1 = 2$ bits, as was shown above) [21].

The lower $l(k)$ and upper $h(k)$ boundaries of a code bank number $k$ are given by [35] as

$$\begin{aligned} l(k+1) = h(k) &= \frac{2^{Start+(k+1)\cdot Step} - 2^{Start}}{2^{Step} - 1} , && Step > 0 , \\ l(k+1) = h(k) &= (k+1) \cdot 2^{Start} , && Step = 0 , \end{aligned} \tag{2.21}$$

such that an input symbol $s$ will get a codeword from a code bank $k$ if $l(k) \leq s < h(k)$. The largest $k$, satisfying the equation $l(k) \leq s$, identifies the code bank containing the codeword for $s$

$$\begin{aligned} k(s) &= \left\lfloor \frac{\log_2\left(s \cdot \left(2^{Step} - 1\right) + 2^{Start}\right) - Start}{Step} \right\rfloor , && Step > 0 , \\ k(s) &= \left\lfloor \frac{s}{2^{Start}} \right\rfloor , && Step = 0 . \end{aligned} \tag{2.22}$$

[4]A code bank corresponds to a uniform segment of the codeword length distribution function, as has been discussed at the beginning of this section

Using the definitions above, any Start-Step-Stop code can be written as

$$C_{Start,Step,Stop}(s) = \{C_U(k(s)), C_\beta(s - l(k(s)))\} \ .$$

For some discrete random variable X with a finite alphabet $\chi$, the average code length can be shown to be

$$L_{C_{Start,Step,Stop}}(X) = \sum_{x \in \chi} p(x) \cdot (k(s) \cdot (Step + 1) + Start + 1) \ , \qquad (2.23)$$

with $k(s)$ given by Eq. (2.22). Finding the optimum parameters for the triplet $(Start, Step, Stop)$ that minimize the average length in a closed form is only possible, if the analytical expression for the PMF of $X$ is known. Otherwise, the concave nature of the function in Eq. (2.23) can be explored, if the distribution is a non-increasing function. If no assumptions about the source distribution can be made and only the observations of $X$ are present, an exhaustive search can be performed, under the constrain $h(k_{max}) \geq N$ (the last code bank can accommodate the maximum value of $s$), where $N$ is the largest expected integer value of a source symbol [35]. It should be pointed out that finding the optimum parameters for these general codes is in fact equivalent to choosing the most suitable parametrized fixed code (e.g. Golomb, Rice, Elias, etc.).

## 2.4 Optimized Source Coding for Sonar Data

Most of the existing approaches for the reduction of amount of data, produced by a sonar, consider the final image after the signal processing is done and thus concentrate on image compression techniques, such as based on wavelet transform [36], discrete cosine transform [37], or even inspired by compressive sensing [38]. There are only a few examples for using the well-established compression methods for the raw sonar data [39], [40].

These lossy image compression methods can be considered feature extraction methods, as they try to keep only the relevant source information. They clearly depend on the array processing being used and cannot provide the unaltered raw data for alternative processing (e.g. adaptive beamforming). This is only possible with lossless source coding, which maps the discrete source symbols into codewords in a fully reversible manner.

### 2.4.1 Sonar Data Properties

Typically, sound waves propagate through a very inhomogeneous medium, resulting in sound scattering and attenuation. The variations of sound speed

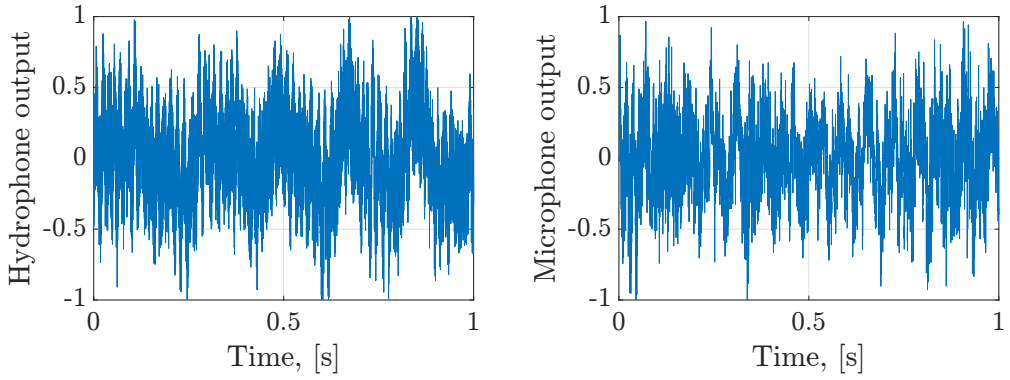


(a) Hydrophone (b) Microphone

Figure 2.4: Random output sequence of a single hydrophone in a flank array (2.4a) and a microphone (2.4b). The samples have 16-bit signed integer normalized representation, sampling rate is 7.8125 kHz. Hydrophone data is a simulated submarine mission, while the microphone data is recorded in a noisy environment with multiple speakers

at different depths significantly impact the profile of a sound channel. Many sources of noise (sea state, thermal, traffic, biological, etc.) corrupt the attenuated source signals, which then quite often appear to be below the noise floor.

Despite all the differences between underwater acoustics and audio data, they both are obviously band-limited, suffer from reverberation and noisy environment (more so under water), and include periodic signals from multiple simultaneously transmitting sources. A simple example in Fig. 2.4 shows the periodic patterns occurring in an audio and in a sonar data stream. This is by far not a comprehensive analysis of both data sources, but it gives some initial motivation for applying of audio source coding in sonar context.

Within the scope of this work two sonar datasets have been used. Both resulted from simulating different scenarios of a submarine mission with multiple moving targets, very close, but not identical to the real world classified data. Each set contains 2 hours of raw data from 96 single hydrophones of a flank array (linear array, Fig. 2.1), sampled at $T = 7.8125$ kHz and uniformly quantized at 16 bit.

Each hydrophone of the sonar array generates discrete source symbols and can be represented as a random process $X_s = \{X_s(n)\}$, where the random variables of the set $\{X_s(n)\}$ map the sampled outcomes $n$ to a signed 16 bit integer

$$X_s(n) = Q(f_s(nT + s\Delta t)),$$

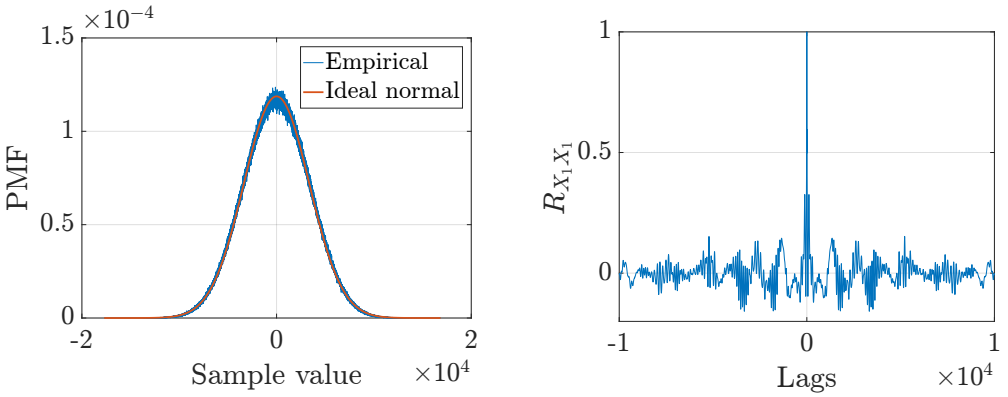


(a) PMF (b) Autocorrelation

Figure 2.5: Probability mass function estimate and autocorrelation function of the first hydrophone in the array. Both functions are calculated over the entire dataset. The bins in (a) correspond to the source alphabet ($2^{16}$ symbols) and the lags in (b) are limited to $\pm 10^4$ samples

with $Q(.)$ being the uniform quantization function and $s$, $f_s$, and $\Delta t$ defined earlier in Sec. 2.1.

Compared to the underwater survey data in, e.g., [39] or typical speech data [41], the empirical probability distribution of $X_s$ in Fig. 2.5a, based on the above described datasets (assuming the ergodicity of the random process), tends to be very close to an ideal normal distribution. This holds for all sensors (Fig. 2.6) in both data sets. The non-uniformity of the source PMF already indicates some potential for the source coding[5]. It does not, however, take into account the memory of the source, resulting from sample-to-sample correlation.

As can be already seen in Fig. 2.4a, the periodicity in the hydrophone signal means the samples are not quite independent. This is even more evident in Fig. 2.5b, where the autocorrelation of the source sequence is far from being close to the $\delta$ function. Before the actual coding occurs, some kind of de-correlation would be appropriate.

This is exactly the situation the transform coding approach was developed for. Its steps include applying some linear transform to produce uncorrelated data, then quantize and (entropy) encode this data [42]. Obviously, quantization is the only step introducing noise, such that avoiding it results in

[5]A uniformly distributed *discrete* random variable is known to have the maximum entropy, as all the possible values are equally likely. Any other distribution would result in a less entropy and potentially redundant representation. Rather surprising, this is not the case for *continuous* or differential entropy, which is maximum for the normal distribution.

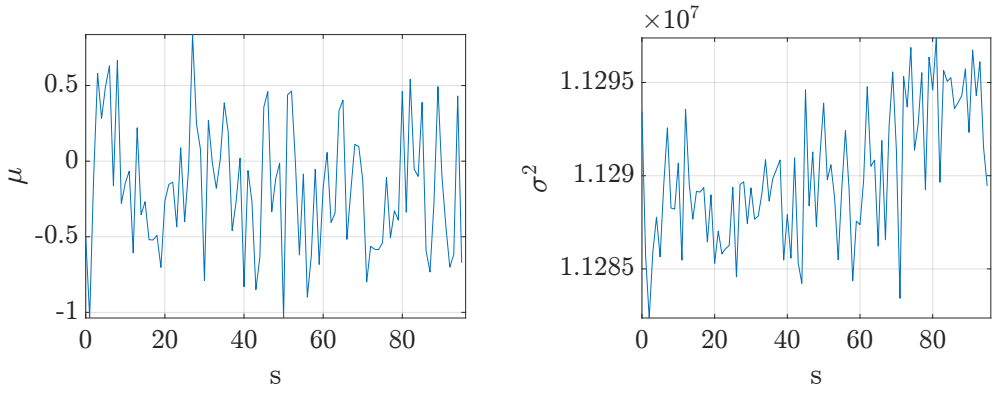


(a) Mean (b) Variance

Figure 2.6: Best fitted mean and variance values of an ideal Gaussian distribution for each sensor ($s \in [0, M-1]$). The results are shown for a single data set, but the other one produces very similar results

a lossless transform coding. This method is widely used in lossy image and video coding, where the optimum Karhunen-Loeve transform, a sub-optimum but efficiently implementable DCT [23] or wavelet transform [43] are used. The latter can also be used in a lossless way [44]. A possibly more suitable approach for this purpose, concerning general data sources and specifically audio signals, is, however, the linear predictive coding described earlier in Section 2.2.

### 2.4.2 Linear Prediction of Acoustic Signals

Applying linear prediction to acoustic signals, described above, is rather straightforward. The optimum prediction parameters, satisfying Eq. (2.7) can be calculated either for the whole data set, assuming the ideal stationarity of the source or for the blocks of data. The latter approach is widely used in practice, as real sources are seldom perfectly stationary and are better modeled as locally block-stationary processes.

The dependency of the prediction gain on different block sizes $B_{LP}$ and predictor order is shown in Fig. 2.7a. Larger blocks are expected to suffer from non-stationarity, but this has a very limited influence on the prediction gain for the provided acoustical data. The block sizes larger than $B_{LP} = 10^{12}$ show exactly the same behavior. As far as the precision of the predictor coefficients is concerned, switching to a lower bit-width resolution (8 instead of 16) does not result in a dramatic performance lost, as can be seen in Fig. 2.7b, such that the 8-bit coefficients will be used for all the following

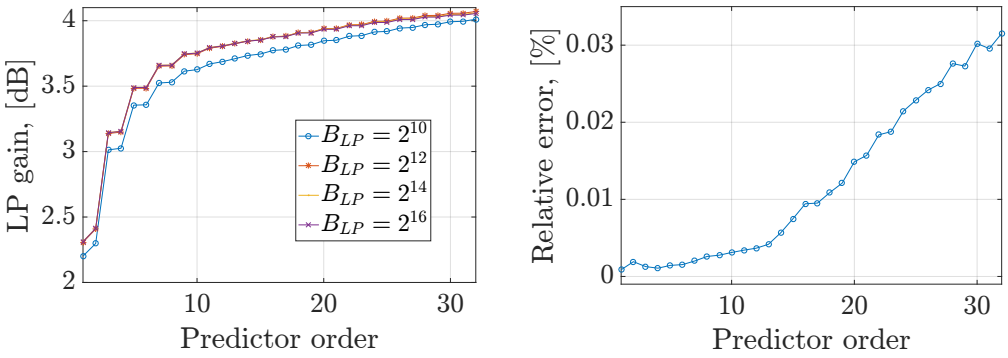


(a) Mean prediction gain

(b) Mean gain relative error

Figure 2.7: Influence of the block size and prediction coefficients resolution on the expected value of the prediction gain over all blocks and all channels in both data sets. The relative error in Fig. 2.7b is calculated as a difference between the gains, calculated by 16-bit LP and 8-bit LP.

simulations. The results in Fig. 2.7 and most of the following figures (2.8 and 2.9) are mean values for the first data set only, as the behavior is essentially the same for all channels and both data sets, received for testing purposes.

The mean gain in Fig. 2.7a, calculated as the average over gains for all channels, approaches the flat region (the upper bound is known as asymptotic prediction gain, given in e.g. [23]) at the LP order of roughly 25, getting as high as 4 dB. This result means that applying linear prediction narrows the bell-shaped part of the actual distribution and thus promises a higher compression gain due to a stronger limitation of the actually used range of values.

Perfect prediction of a discrete random variable means also a perfect match of its PMF. This is not the case for provided acoustical data, as can be seen in Fig. 2.8a for LP of order 16. The predictor output has roughly the same expected value of zero but a slightly different standard deviation of $\sigma_{LP} \approx 2575.1$, compared to $\sigma_{raw} \approx 3360.6$ for raw data in this example. The resulting PMF of the residuals is a linear combination of both, according to Eq. (2.1), and appears to be a mixture of two normal distributions. Despite the form of PMF with two separate peaks, the residual PMF is actually a unimodal distribution, according to the test given in [45]. An interesting observation is that increasing the order of predictor results in the progressing separation of peaks and to a switch to a bimodal distribution at some point. This behavior can be observed in Fig. 2.8b. Although the variance of the residuals is decreasing, meaning improvement of the prediction gain, it is

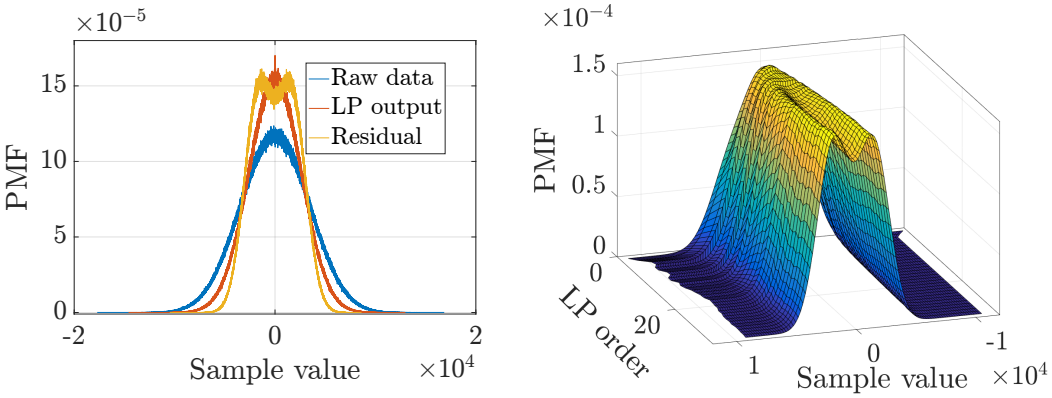


(a) PMF for fixed LP order (b) Residual PMF for variable LP order

Figure 2.8: Probability mass functions for the fixed LP order (16), and linear predictor output PMF for different order values

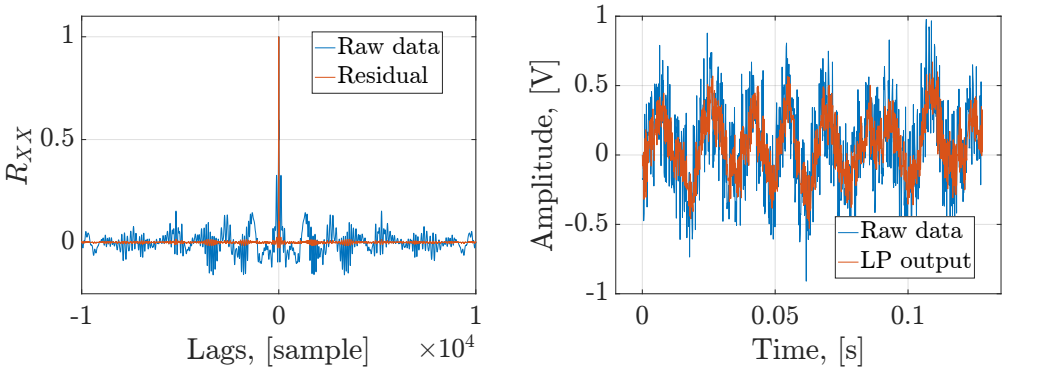


(a) Autocorrelation (b) Time-domain signal

Figure 2.9: Autocorrelation function of residual signal and time-domain signal of the first sensor before and after applying linear prediction of order 16

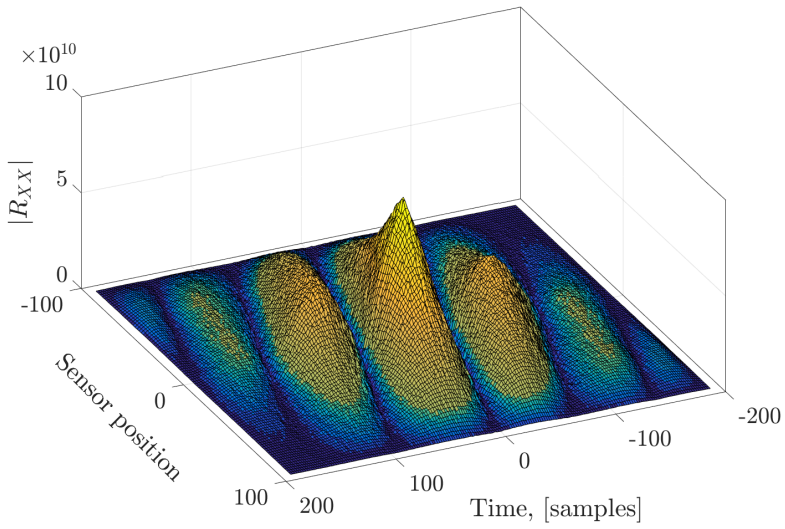


Figure 2.10: 2-D autocorrelation of sonar data. The array consists of 96 sensors and the time frame of 192 samples is used for calculations

difficult to find a matching variable-length code for this kind of distribution, as will be shown in the next section.

Despite a slight difference in probability distribution, applying linear prediction of rather moderate orders (up to 32) results in significant reduction of the time-domain correlation of the acoustic data, received by a sonar. The autocorrelation function of the residuals in Fig. 2.9a has a single peak at the origin, meaning the absent periodicity in the noise-alike residual sequence. The linear predictor in fact filters the periodical part of the signal, as can be seen in Fig. 2.9b.

### Multichannel prediction

A very similar behavior of all channels in the given sonar array suggests that some degree of multichannel correlation should be present. The two-dimensional autocorrelation function in Fig. 2.10 clearly supports this assumption. The correlation along the spatial dimension is not periodical, in contrast to the time dimension, and decreases almost linearly with increasing offset with a maximum at a constant angle to the spatial axis. The structure of a linear array from the first section (Fig. 2.1) is the reason for this behavior. In the case of a single source, the cross-correlation between the sampled sequences of different sensors is maximum at an offset (or lag), corresponding to the delay $(s_i - s_j) \cdot \Delta$ , $i, j \in [1, M-1]$, resulting in the

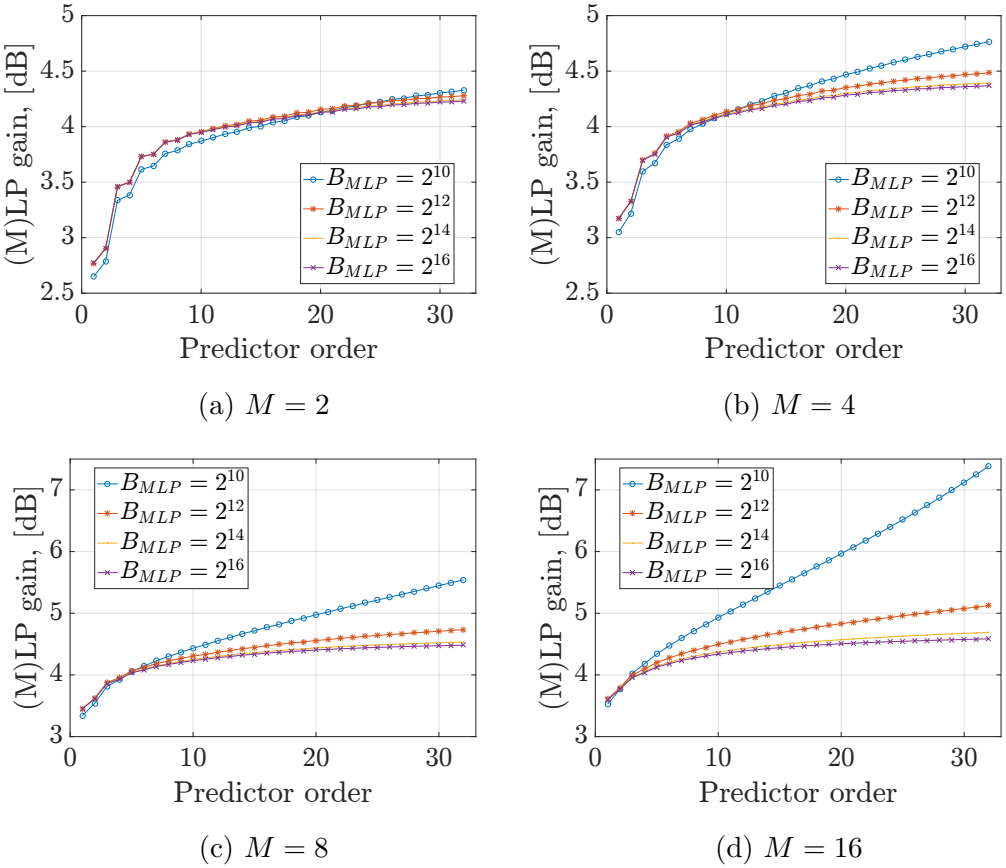


(a) $M = 2$ (b) $M = 4$

(c) $M = 8$ (d) $M = 16$

Figure 2.11: Mean prediction gain for different MLP configurations

constant autocorrelation function value at a constant spatial angle. In the presence of multiple sources and noise, the function, presented in Fig. 2.10, is decreasing and the angle is a superposition of the multiple directions of arrival.

The cross-correlation between the sensors can now be exploited by the multichannel linear prediction (MLP) from Section 2.2.2. Besides the block size $B_{MLP}$, the number of channels (sensors) $M$ is an additional parameter of the MLP, used to generate Fig. 2.11. A more pronounced dependency on the block size with increasing $M$ – smaller blocks are better – can be explained as a direct consequence of non-stationarity.

An additional dimension clearly improves the performance of the linear prediction in Fig. 2.12a. However, the comparison with a simple LP may not be fair, due to the different effective prediction order. The linear prediction order $L$ corresponds to the total number of the filter coefficients in case

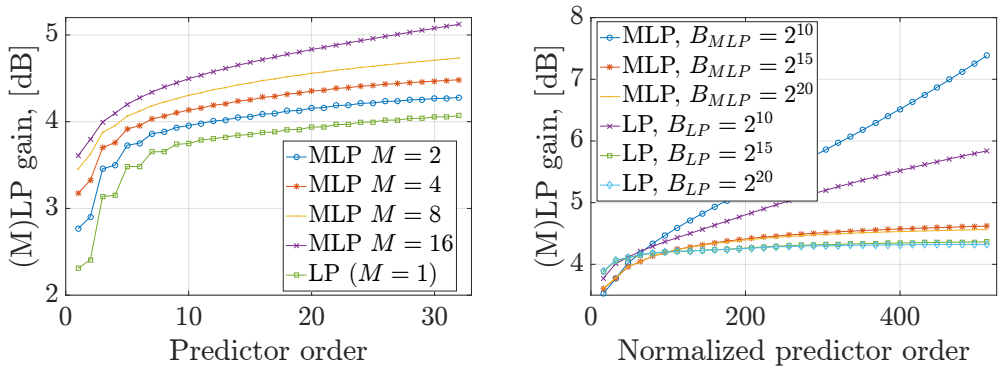


(a) Non-normalized order, $B_{MLP} = 2^{12}$ (b) Normalized order

Figure 2.12: Mean prediction gain of single- and multichannel linear predictors

of the single-dimensional LP. The number of the coefficients for the multi-dimensional case is, however, given by $L \cdot M^2$, where $L$ represents only the time dimension. In Fig. 2.12b the (normalized) prediction order is redefined as the total number of coefficients. The higher performance of the MLP ($M = 16$) is well recognizable only with orders higher than 50 ($L \approx 3$). Increasing the value of $M$ and keeping the constant order results in a decreasing time component, represented by $L$. The higher autocorrelation in the time-domain cannot be compensated by adding more spatial dimensions with progressively lower cross-correlation, which is demonstrated in Fig. 2.12b.

The prediction gain tends in general to be higher, using MLP with high orders and small block sizes. However, the interaction with an entropy encoder can be a challenge, as it is typically more efficient on larger blocks. Besides, the high number of coefficients will decrease the effective compression ratio, such that an optimum multichannel linear predictor will not necessarily result in an optimum linear predictor coding, which also includes a source code.

### 2.4.3 Optimal Code for Residual Compression

The final stage of the linear predictive coding, discussed in Section 2.2, is an entropy encoder. Although the well-established Huffman code is known to be optimum for any probability distribution, the encoder and decoder can be optimized in terms of implementation complexity, when one of the fixed universal codes of Section 2.3 is used. Their redundancy could be very close to zero, if the probability distribution of the code is perfectly matched to

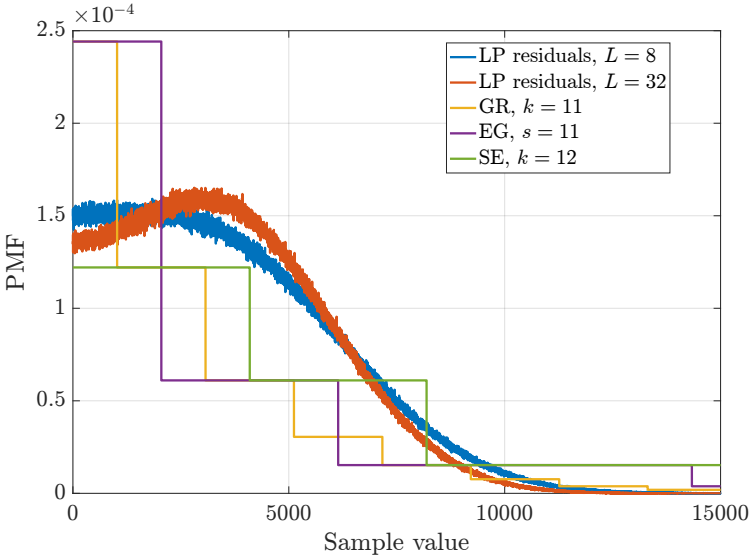


Figure 2.13: Probability mass functions of linear prediction residuals (block size $B_{LP} = 10^{16}$) and different variable-length entropy codes

that of the source.

The PMFs of the codes, with parameters best-fitted to the distributions of LP residuals of the available data sets, are shown in Fig. 2.13. The residuals were first mapped to nonnegative integers by bijection [21], which first multiplies the absolute value of input by a factor of two and then adds one to the output, if the input was a positive integer. Calculation of the optimum parameters of the Golomb-Rice (GR), Exp-Golomb (EG), and subexponential (SE) codes is given in Section 2.3 and is rather straightforward. The resulting triplet of parameters for the Start-Step-Stop code is fully equivalent to the Golomb-Rice code in this case. The original description of the optimization procedure for these codes is unfortunately not complete. This optimum solution can, however, be calculated by replacing equations (1) and (2) in the original paper [35] by equations (2.21) and (2.22), respectively, given in Section 2.3.

In general, the subexponential code achieves the closest match to the source PMF. Its structure has a very useful property for the given source distributions – the code PMF can be divided into uniform and exponential parts. The uniform part is in fact the best fit for the source PMFs up to the sample values of roughly 3000. The tendency of the residual PMF to form two peaks with increasing predictor order, as discussed in the previous section, is handled quite well by this code: at low values of predictor order

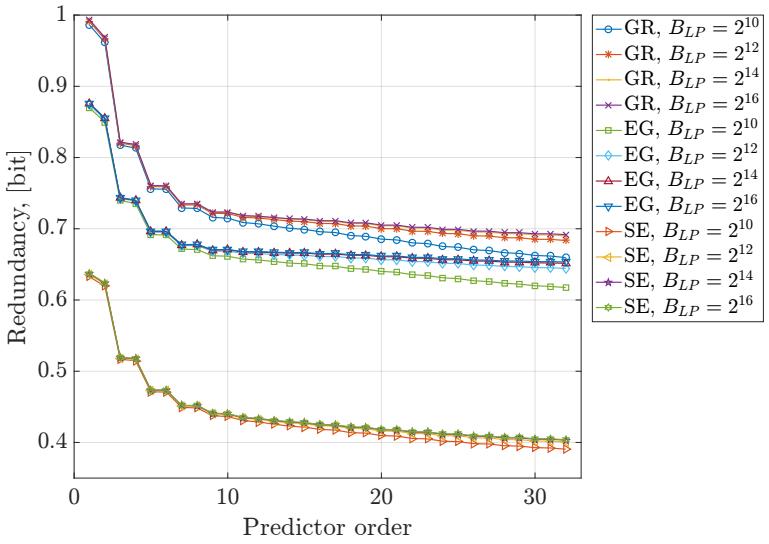


Figure 2.14: Mean redundancy over all channels of different variable-length entropy codes

it is close to optimum and the redundancy at higher values is rather low, compared to other codes, which all assume a non-increasing PMF.

Indeed, the results in Fig. 2.14 prove that the better the PMF match, the more effective the code is. The redundancy, calculated as the difference between the corresponding average code length, and the entropy of the source (LP residuals), given by Eq. (2.16), is lowest for the subexponential code by a margin of roughly 0.3 bit per sample, compared to the Golomb-Rice code. Nevertheless, all the codes perform rather well, with the redundancy being less than 1 bit – comparable or even better than the theoretically worst performance of the Huffman code. The minimum redundancy is achieved by choosing the smallest block size and the maximum available predictor order, as the smooth non-increasing curves suggest.

Following the trend for the prediction gain, smaller block sizes result in a better performance for all codes. However, the subexponential code behaves better even here – the dependency is very slight, compared to other codes, which means flexibility and better performance in terms of compression ratio.

The compression ratio is an ultimate performance measure for the final application, which also takes the overhead into account, introduced by the $L_N$ (normalized order) LP coefficients of length $b_{LP}$ bits and variable number of source coding parameters $P$ (e.g. single parameter $k$ of the subexponential code) of the length $b_{par}$ bits. Essentially, this is a ratio of the compressed

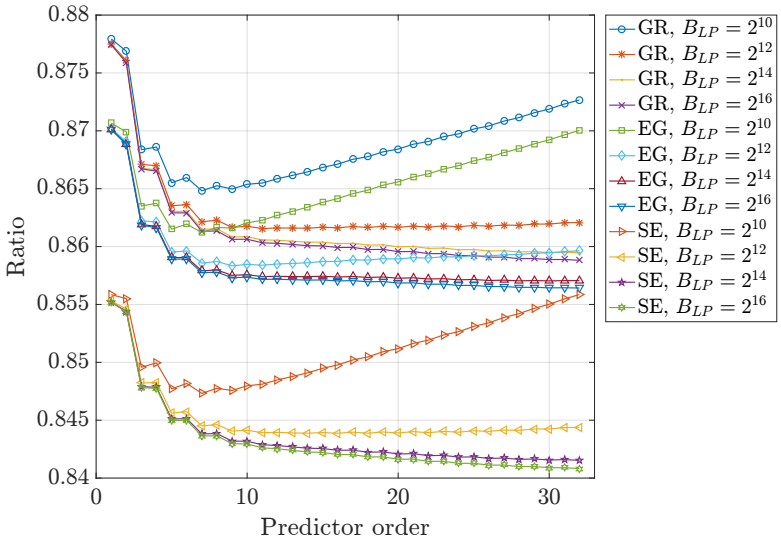


Figure 2.15: Mean compression ratio over all channels of different variable-length entropy codes

block size to its original size $B_{LP}$, defined as

$$CR_{C(S)} = \frac{\sum_{s \in S} l_C(s) + L_N \cdot b_{LP} + P \cdot b_{par}}{B_{LP}} , \tag{2.24}$$

where $S$ is the source sequence of an arbitrary size $B_{LP}$ bits.

Opposite to the redundancy behavior, the ratio is smaller and thus the performance is better, when larger block sizes are used, as shown in Fig. 2.15. Obviously, this is due to the overhead of transmitting the LP coefficients. As a function of the predictor order, the ratios will have a single minimum (which is also the global optimum) not necessarily at the highest value of order. Again, the subexponential code performs best and is used in the following simulations. It should however be noted that the performance is not very spectacular, compared to the best examples of text or speech coding. The acoustical signal, sampled by a sonar, is generated in a very noisy environment and hence has less potential for lossless source coding, compared to those examples. Nevertheless, roughly 15% data rate reduction is a welcomed improvement.

Comparing both available data sets and different channels in Figs. 2.16a and 2.16b shows a rather uniform behavior. The variances of both redundancy and compression ratio over the channels are very low. This is not very unexpected, as the channels spatially sample the same noisy wave front.

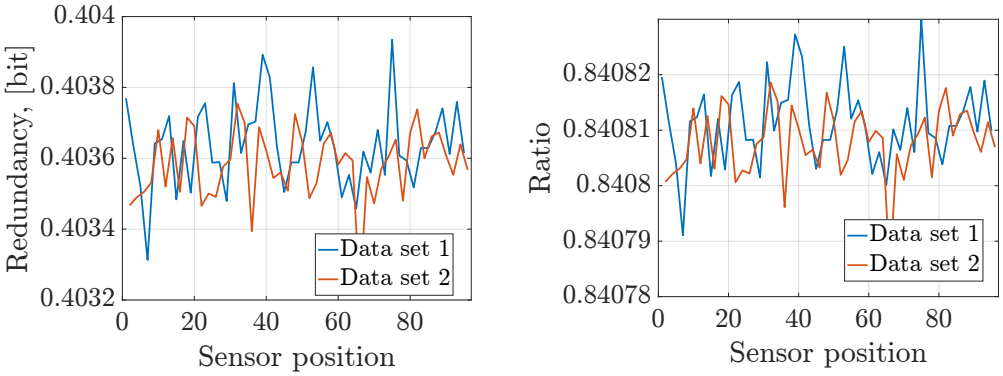


(a) Redundancy

(b) Compression ratio

Figure 2.16: Redundancy and compression ratio of the subexponential code; both data sets and all sensors are shown. The linear predictor of order $L = 32$ and block size $B_{LP} = 10^{16}$ is used.

Even better performance in terms of redundancy can be achieved by applying multichannel linear prediction, as can be seen in Fig. 2.17a. Also here the smaller block sizes are preferred and can reduce the mean redundancy of a 16-channel $M$-LPC to be very close (0.1-0.2 bit per sample) to the entropy. The very low redundancy does not necessarily result in the lowest compression ratio in Fig. 2.17b, as was also the case for the single channel LPC. The comparison between single and multichannel version of LPC are now also fair as a function of non-normalized predictor order, as this is already included in Eq. (2.24). The number of the coefficients, and thus the overhead, grows exponentially with $L$ for $M$-LPC, which results in a low performance at high values of $L$ and small block sizes. As the block size increases, $M$-LPC outperforms LPC by a small margin. Increasing $L$ does not automatically decreases the minimum ratio, such that the optimum value is around 10.

Reducing the number of channels in $M$-LPC (see Fig. 2.18) results in a slightly increased compression ratio. Although the best performance can only be achieved with more channels, using less channels for $M$-LPC has an advantage of lower implementation complexity and higher flexibility in terms of the block size. It is usually limited in practice by memory or initial delay requirements, such that the encoder has to be used under not optimum conditions. It can be seen in Fig. 2.18 that reducing the block size for $M = 4$ does not increase the ratio by a large margin, as it is the case for $M = 16$. Still, compared to the single channel LPC, the 4-channel $M$-LPC performs noticeably better.

The comparison of different source codes, including popular dictionary

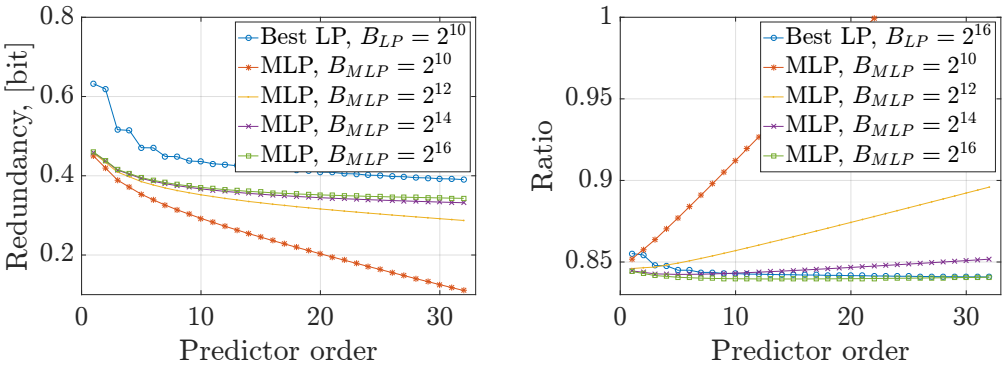


(a) Redundancy

(b) Compression ratio

Figure 2.17: Mean redundancy and compression ratio of the subexponential code, used with the multichannel ($M = 16$) linear predictor

methods (e.g. ZIP and BZIP2) and the lossless audio-codec FLAC [21], given in Table 2.3, clearly indicates that the combination of linear prediction and subexponential codes has an application potential in sonar data transmission. The multichannel prediction shows a better performance in absolute numbers, but this fact is rather of theoretical interest, as the implementation complexity would outweigh its advantages in practice.

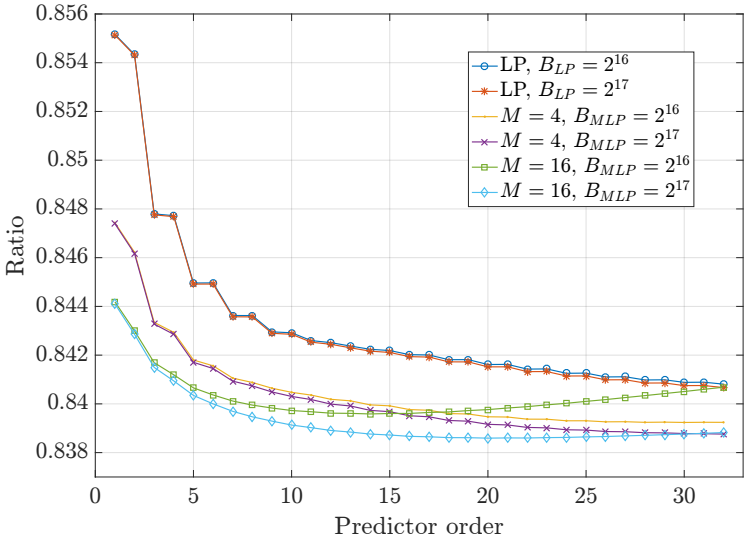


Figure 2.18: Mean compression ratio of the subexponential code, used with the multichannel linear predictor and larger block sizes

| Compression method | block size | max. compression ratio |
|---|---|---|
| ZIP | n.a. | 0.932 |
| BZIP2 | 100 kbit | 0.908 |
| BZIP2 | 900 kbit | 0.888 |
| FLAC | 130 kbit | 0.859 |
| FLAC | 1 Mbit | 0.858 |
| LP+SE | 130 kbit | 0.841 |
| LP+SE | 1 Mbit | 0.840 |
| 4-MLP+SE | 130 kbit | 0.839 |
| 16-MLP+SE | 130 kbit | 0.838 |
| 16-MLP+SE | 1 Mbit | 0.837 |

Table 2.3: Mean compression ratios of different source codes

# Chapter 3

# The Twisted Pair Bus Channel

Any communication system uses a channel to pass information from transmitter to receiver. In order to build an optimum system, it is important to know how such channel behaves, prior to making a decision, how the system components will look like. When using electromagnetic waves as an information carrier, the electrical properties of the medium describe the channel behavior. In that sense, this chapter provides the basis for all future work on MC-TP, starting first with theoretical basics for electromagnetic modeling of two parallel wires, followed by modeling of a bus structure. The model parameters are found, fitting the model curves to measurements. Using the modeled channel and knowing the noise sources it is then possible to calculate the channel capacity and to investigate the influence of termination impedances on it.

## 3.1 Transmission Line Theory

In the context of this work, a copper twisted pair is used as a transmission medium. From the electro-magnetics point of view, such a two-conductor structure is called a wave guide, or in this case a transmission line, because of the capability of guiding Transverse Electro-Magnetic (wave) (TEM) waves. Other examples of transmission lines with TEM or quasi-TEM fundamental propagation mode are coaxial lines and micro strips.

The physical background behind any transmission line is described by four vector fields (electric and magnetic field, electric displacement, and magnetic induction) in Maxwell's equations. For more information and derivation, the reader is referred to [46] and [47]. Important is that in case of TEM waves on a transmission line, the electromagnetic fields can be related to currents and voltages. Given this fact and dividing the line into a large number

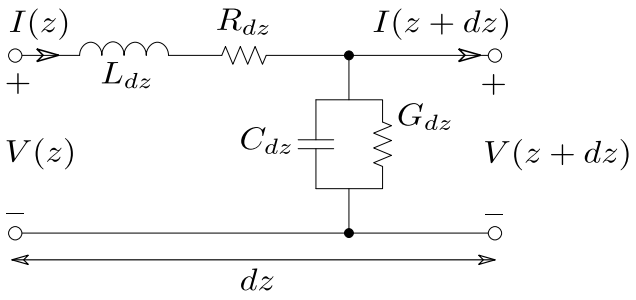


Figure 3.1: Element $dz$ of a transmission line

of small segments, shorter than the wavelength, it is possible to derive a lumped equivalent circuit for each short element, which can be analyzed by Kirchhoff's laws [46].

Assuming time-harmonic signals, the analysis of the equivalent circuit, consisting of a series inductance $L$, a series resistance $R$, a shunt capacitance $C$ and a shunt conductance $G$ per unit length, shown in Fig. 3.1 results in wave equations [48]

$$\frac{\delta^2 V(z)}{\delta z^2} - \gamma^2 V(z) = 0 \quad \frac{\delta^2 I(z)}{\delta z^2} - \gamma^2 I(z) = 0, \tag{3.1}$$

where $\gamma = \alpha + j\beta$ is the so-called complex propagation constant. A superposition of forward (subscript $+$) and reverse (subscript $-$) voltage and current waves is a solution to these equations

$$V(z) = V_0^+ \exp^{-\gamma z} + V_0^- \exp^{\gamma z} \quad I(z) = I_0^+ \exp^{-\gamma z} + I_0^- \exp^{\gamma z}. \tag{3.2}$$

The characteristic impedance of the transmission line is then defined as:

$$Z_0 = \frac{V_0^+}{I_0^+} = \frac{V_0^-}{I_0^-}.$$

The $RLGC$ parameters are also called the primary parameters, whereas $\gamma$ and $Z_0$ are called the secondary parameters of a transmission line. Assuming the homogeneity of a used cable, either set of parameters is sufficient to fully characterize its electrical behaviour.

## 3.2 Cable Parameter Modeling

A cable model typically tries to describe (or predict) its electrical characteristics, defining the primary or secondary parameters.

Existing cable models can be arranged in the three major groups: analytical models, which use the physical background and take into account material properties and geometry (Kelvin, VUB, RLGC(f) [49], [50]); rational functions, which try to fit some measured curves without any physical modeling; and semi-empirical models (BT, KPN, and MAR [51]), which are physical models, improved by some less-physical heuristics [52]. The second and third groups can have problems in time-domain simulations, because of non-causal behavior [53]. The real and imaginary part of the impedances in these models are typically independent, whereas they must correspond to Hilbert transforms, the model to be causal. In case of the MAR model this was taken into account, so that the MAR model is in fact causal [54]. Besides, an existing non-causal model can be corrected to respect the causality conditions [55].

All mentioned models assume a uniform transmission line and thus a uniform cable, which is usually not true, especially in case of a twisted pair cable. The modeling methods in [56] and [57] try to take longitudinal variations into account, dividing the cable into small sections, characterized by their ABCD matrix, and calculating an ABCD matrix of the whole cable, using cascade property of ABCD matrices. The computational complexity of these methods is clearly much higher, than that of uniform models, if the objective is to improve accuracy by increasing the number of sections. Although the model in [56] is an analytical solution, it is still demanding in a computational sense and cannot predict all cable discontinuities.

Using results in [52], the MAR model is a good choice, as it is efficient, easy to estimate, and causal. It has already been used to model an Austrian cable in [58]. The MAR model uses the following equations, to model the series impedance and shunt-admittance:

$$Z_s(f) = j\omega L_\infty + R_0 \left( \frac{1}{4} + \frac{3}{4} \cdot \sqrt{1 + \frac{as(f)(s(f)+b))}{s(f)+c}} \right)$$
$$Y_p(f) = \omega C_f \cdot (j + \tan\delta) = j\omega C_{1MHz} \cdot (jf \cdot 10^{-6})^{\frac{-2\delta}{\pi}}, \qquad (3.3)$$

where

$$\omega = 2\pi f, \quad s(f) = \frac{\mu_0 jf}{0.75^2 R_0}, \quad C_f = \frac{C_{1MHz}}{(f \cdot 10^{-6})^{2\delta/\pi}}.$$

This model has seven parameters:

- $L_\infty$ is the high frequency inductance per km [H/km],
- $R_0$ is the DC resistance per km [Ω/km],
- $a$, $b$, and $c$ are skin effect coefficients,

- $\delta$ is the shunt capacity loss angle (constant),

- $C_{1MHz}$ is the capacitance per km at 1 MHz [F/km].

A typical method of estimating the appropriate values of these parameters is fitting (also called regression) the model values to the measurement values at given frequency points. The MATLAB simplex minimization routine can be used for this (non-linear) task in a following way: a function (called an objective function), which value should be minimized, is defined as an error calculating function, assuming the error to be zero mean and normally distributed. The most popular example is probably the method of Ordinary Least-Squares (OLS), where the objective function calculates the sum of squared errors, with an error (also called residual) defined as a difference between measured and modeled value at any frequency point [59]. Other examples include Least Squares Percentage (LSP) and Mean Absolute Percentage Error (MAPE) regressions, see [60] for more details.

The problem of OLS is the lack of robustness: a single outlier (not a seldom event in measurement data) can have a large effect on the estimate. There are plenty of examples of another approach, generally called robust regression, which is supposed to overcome the problems of non-robust methods: Least Median of Squares (LMS) regression and M-Estimation, to name a few [59], [61]. The last one minimizes the objective function, where the contribution of each residual is regulated by some weight function. Throughout this work, the M-Estimation with Huber weight function is used, being more robust than OLS and due to its computational simplicity and fast convergence.

## 3.3 Transfer Function of Linear Bus Structures

A linear bus topology, as depicted in Fig. 3.2, is an example of a multipath channel, as it has taps and branches, which provide multiple paths for signal propagation: not only the direct path between a receiver and transmitter has to be considered, but also the additional paths, generating echoes as a result of reflections at impedance discontinuities. Such a channel is also typical in PLC systems.

There are two approaches for modeling a multi path channel in a powerline environment. The first, developed in [19] and [62], uses the following

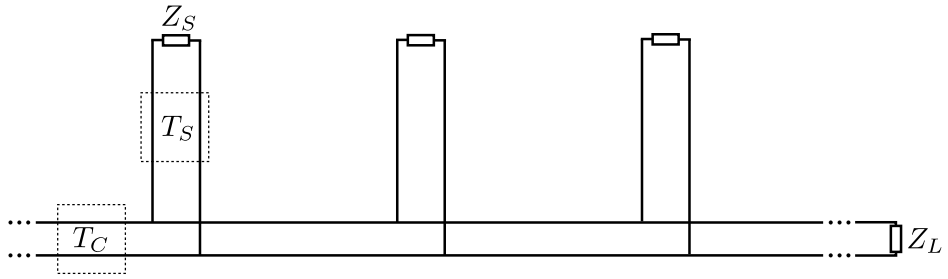


Figure 3.2: Linear bus topology

equation for the transfer function to model multi-path propagation:

$$H(f) = \sum_{i=1}^{N} g_i \cdot e^{-(a_0 + a_1 f^k) d_i} \cdot e^{-j2\pi f (d_i/\nu_p)}$$

The model parameters (parameters description in [62]) are estimated, using the measurements of the whole system, which is no easy task in a complex system. Even knowing individual system components, it is hard to predict system behavior.

Another approach is to split the system in Fig. 3.2 into two-port network sections, represented by their ABCD matrices, and then calculate the ABCD matrix $T_{Sys}$ of the whole system (which is also a two-port network) and its transfer function, using the cascade property [63]. A cable of length $l$ (or actually, a transmission line) can easily be represented as a two-port network, using its secondary parameters $\gamma$ and $Z_0$:

$$T_C = \begin{bmatrix} \cosh \gamma l & Z_0 \sinh \gamma l \\ \frac{1}{Z_0} \sinh \gamma l & \cosh \gamma l \end{bmatrix} \tag{3.4}$$

A branching connection can be modeled as a shunt impedance across the main line:

$$T_S = \begin{bmatrix} 1 & 0 \\ 1/Z_{in} & 1 \end{bmatrix} \tag{3.5}$$

with $Z_{in} = \frac{AZ_S + B}{CZ_S + D}$, calculated from two-port network ABCD parameters of the branch, terminated by impedance $Z_S$. The system ABCD matrix is then a simple multiplication of $N$ segment matrices from equations (3.4) and (3.5), according to the cascade property [64], [65]:

$$T_{Sys} = T_C^{(1)} \cdot T_S^{(1)} \cdot T_C^{(2)} \cdot T_S^{(2)} \cdot \quad \cdots \quad \cdot T_C^{(N)} \cdot T_S^{(N)}$$

The transfer function $H_{model}(f)$ of the bus system can then be calculated from the ABCD matrix $T_{Sys}$, assuming a known output impedance of the

transmitter $Z_S$ and the input impedance of the receiver $Z_L$ as

$$H_{model}(f) = \frac{Z_L}{AZ_L + B + CZ_SZ_L + DZ_S}. \tag{3.6}$$

Similar to the system transfer function above, the insertion loss (the ratio between voltage on the load without and with the bus structure) of the system can easily be calculated:

$$IL_{model}(f) = -20\log\left(\frac{Z_L + Z_S}{AZ_L + B + CZ_SZ_L + DZ_S}\right) dB. \tag{3.7}$$

The latter is usually used for performance calculations, rather than the transfer function (the difference between them is 3 dB, if the reference impedances are equal and purely resistive), because the power constrains typically apply to the power actually transferred into the system [64].

For the purpose of time-domain simulations, the discrete frequency transfer function from Eq. 3.6 can be converted into an impulse response, using the Inverse Discrete Fourier Transform (IDFT). During this process, the band-limiting of the response and possibility for time-aliasing should be taken into account, see [66] for more details. Another possibility is to directly model the channel in time-domain [67], [68].

## 3.4 Cable and Bus Structure Measurements

In previous sections, the models of a single twisted pair cable and a bus structure were introduced. In the case of twisted pair cables, the model parameters can be found in a fitting process, which requires data from single loop measurements. The bus system model, based on ABCD concatenation, in its turn can be verified through a corresponding bus system measurement. This section deals with such measurements and first describes the measurement set-up and calibration or de-embedding methods, followed by the actual measurement results of single cables and two-port measurements of the test structures. The focus here is, also, to learn, how the cables behave under high pressure conditions.

### 3.4.1 One-Port Cable Measurements

#### One-Port Set-Up

The single twisted pair cable High-Frequency (HF) electrical characteristics (e.g. transmission line parameters) as well as a linear bus structure

transfer function or insertion loss can generally be measured using a Vector Network Analyser (VNA) [1]. The primary and/or secondary transmission line parameters of a twisted-pair cable can be determined indirectly using the proposed one-port measurement set-up given in Fig. 3.3. It is supposed to support high frequency measurements up to 100-200 MHz, where it is still possible to provide reliable open or short circuit termination conditions.

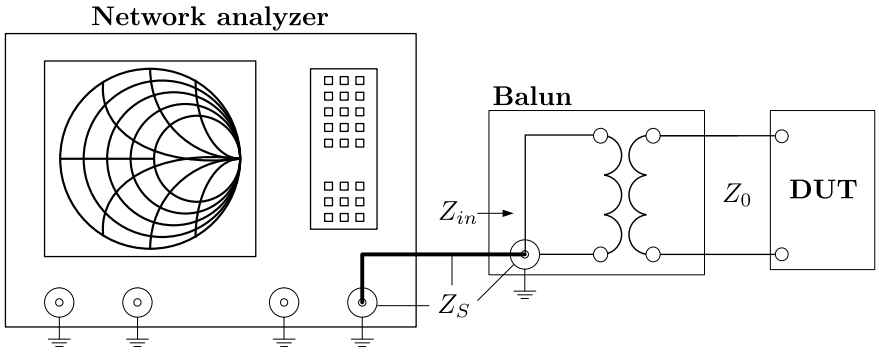


Figure 3.3: One-port measurement set-up

The VNA (Rohde&Schwarz ZVR) unbalanced measurement ports are asymmetric Bayonet Neill-Concelman connector (BNC) connectors with $Z_s = 50\ \Omega$ (source port characteristic impedance). The twisted-pair cables used in this work are balanced (symmetrical) electrical elements with characteristic impedance $Z_0 \approx 100\ \Omega$. A special HF transformer, the so-called balun, is used in this set-up to match impedance on both sides and for balanced/unbalanced conversion. The unbalanced balun port is connected to the network analyzer port, using a 50 Ω coaxial cable. On the other side, the balun provides a balanced port with 100 Ω characteristic impedance, which is used to attach a Device Under Test (DUT), which can be a twisted-pair cable, a connector, or a more complex structure. Similar set-ups have extensively been used for measurements of the Asymmetric Digital Subscriber Line (ADSL) copper loop parameters, for instance in [71], [72], and [73].

This set-up can be schematically represented as a generator with its internal impedance connected to a two-port network, shown in Fig. 3.4.

Let $a_1$, $b_1$ represent incident (generated) and reflected waves on the input port of the two-port network, respectively. They can be represented in terms of two-port network input voltage $V_1$ and current $I_1$ as follows:

[1]For more information about fundamental principals of vector network analysis the reader is referred for instance to [69], [70]

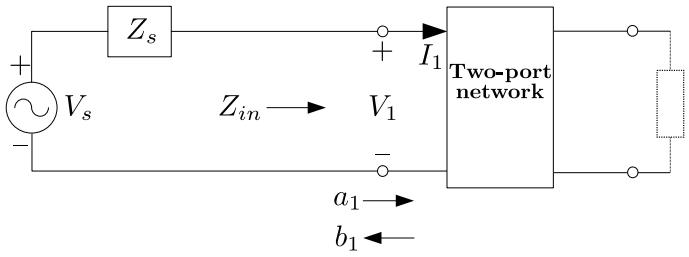


Figure 3.4: Two-port network connected to a generator

$$a_1 = \frac{V_1 + Z_s I_1}{2\sqrt{Z_s}}, \qquad b_1 = \frac{V_1 - Z_s I_1}{2\sqrt{Z_s}}. \tag{3.8}$$

The ratio of the amplitude of the reflected wave $b_1$ to the amplitude of the incident wave $a_1$ is called a reflection coefficient $\Gamma$:

$$\Gamma = \frac{b_1}{a_1} \tag{3.9}$$

The reflection coefficient $\Gamma_{in}$ is directly measured by network analyzer on the input port of the balun.

Using definitions in (3.8) and (3.9) for a two-port network input port of Fig. 3.4, and keeping in mind that $\frac{V_1}{I_1} = Z_{in}$, input reflection coefficient can be expressed in terms of the source and input impedances as

$$\begin{aligned} \Gamma_{in} = \frac{b_1}{a_1} &= \frac{V_1 - Z_s I_1}{V_1 + Z_s I_1} = \frac{\frac{V_1}{I_1} - Z_s}{\frac{V_1}{I_1} + Z_s} \\ &= \frac{Z_{in} - Z_s}{Z_{in} + Z_s}\ , \end{aligned} \tag{3.10}$$

where $Z_{in}$ represents the input impedance of the measured DUT. This can be calculated from the measured $\Gamma_{in}$ using Eg. (3.10) and can later be used to characterize the connected two-port network:

$$Z_{in} = Z_s \frac{1 + \Gamma_{in}}{1 - \Gamma_{in}} \tag{3.11}$$

with $Z_s = 50\ \Omega$. Measuring the input reflection coefficient and calculating the (generally complex) input impedances for different terminations (e.g. open/short circuit conditions), connected to the output port of any two-port network, gives the possibility to calculate the transmission line parameters or ABCD parameters for any passive two-port network.

A twisted-pair cable, with a physical length $l$ comparable[2] to the wave length $\lambda$ (which depends on the measurement frequency range), behaves like a transmission line. According to transmission line theory ([47], Chapter 10), any line can be completely characterized by its complex propagation constant $\gamma = \alpha + j\beta$ and characteristic impedance $Z_0$. The input impedance $Z_{in}$ of a transmission line, loaded by termination impedance $Z_L$ is given by

$$Z_{in} = Z_0 \frac{Z_L + Z_0 \tanh(\gamma l)}{Z_0 + Z_L \tanh(\gamma l)}, \tag{3.12}$$

where the secondary transmission line parameters are the unknown variables, if $Z_{in}$ is known from measurement, according to equation (3.11). Thus, one needs two independent measurements with different values for $Z_L$ to get an equation system, which can then be solved, to find the unknown secondary transmission line parameters. The system has a simple solution, if the values $Z_L = 0$ (short circuit) and $Z_L = \infty$ (open circuit) are used. Using Eq. (3.12)

$$Z_{in}^S = Z_{in}|_{Z_L=0} = Z_0 \tanh(\gamma l), \tag{3.13}$$

$$Z_{in}^O = Z_{in}|_{Z_L=\infty} = \frac{Z_0}{\tanh(\gamma l)}, \tag{3.14}$$

then the secondary transmission line parameters can be calculated as

$$Z_0 = \sqrt{Z_{in}^S Z_{in}^O} \cdot \exp^{jn\pi}, \quad n \in [0,1] \ , \tag{3.15}$$

$$\gamma = \operatorname{atanh}\left(\sqrt{\frac{Z_{in}^S}{Z_{in}^O}} \cdot \exp^{jn\pi}\right) + jm\pi, \quad n \in [0,1], m \in N_0 \ , \tag{3.16}$$

where the terms with multiples of $\pi$ represent the two solutions of square root and the periodicity of inverse hyperbolic tangent, accordingly. These parameters can easily be converted to primary transmission line parameters, keeping in mind that

$$\gamma = \alpha + j\beta = \sqrt{(R + j\omega L)(G + j\omega C)} \ , \tag{3.17}$$

$$Z_0 = \sqrt{\frac{R + j\omega L}{G + j\omega C}}, \tag{3.18}$$

where $R, L, G$, and $C$ are the primary parameters per unit length.

All measurements were done, using the following parameters of the network analyzer:

[2] As a rule of thumb, when $l \geq \lambda/10$

- Source power: -10 dBm
- Start frequency: 250 kHz
- Stop frequency: 125 MHz
- Number of frequency points: 2001
- Frequency sweep scale: logarithmic

Every measurement was repeated 3 times and an average calculated. No outliers were allowed, every measurement with visible outliers was repeated.

### Measurements and Modeling Results under Normal Pressure

This and the next sections introduce the results of measurements on different underwater cables, using one-port measurement set-up, described above in Section 3.4.1. The measurement curves were then used to fit the parameters of the so-called MAR-Model [54]. The cables have been measured under normal (1 bar) pressure and their performance (fitted curves of attenuation and characteristic impedance) was compared to that of a typical shielded network cable of category 5e (in terms of TIA/EIA-568-B.2, see [74]).

The cables used during the measurements were:

- 12m UW100 (Black/White, Red/White, Braun/White)
- 8m UW130 (Blue/White, Violet/White, Braun/White)
- 8m UW083 (Blue/Black, Violet/Black, Blue/White)
- 2m UW083 (Blue/Black, Violet/Black, Blue/White)
- 6m Cat5e AWG26 (Blue, Braun, Orange)

All the cables, listed above, have multiple data line pairs. Additionally, all cables introduce dedicated power lines. These wires will not be used in any of future usage scenarios. Three data pairs of each cable were measured, to save time and still have some statistics. The colors of these pairs are given in the parenthesis. The pairs are chosen such, that two of them have the smallest distance in between and the third has the largest distance. This allows some comparison in terms of crosstalk.

All underwater cables are produced by LEONI and correspond to the cables typically used to build an underwater sonar system. The UW130 cable is actually the next generation of UW083 cable, so the direct comparison is of interest.

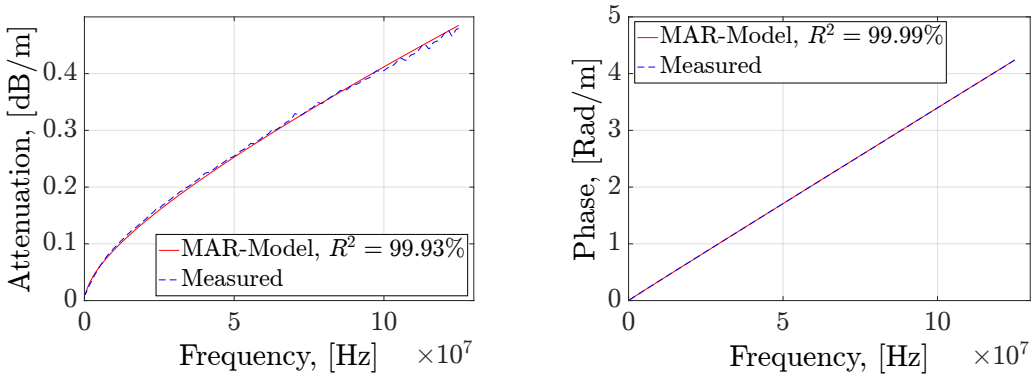


(a) Attenuation $\alpha$ (b) Phase $\beta$

Figure 3.5: Propagation constant of UW100 cable under normal pressure

The propagation constant (with real part $\alpha$ and imaginary part $\beta$, according to Eq. (3.17) and characteristic impedance of all the cables were calculated directly from calibrated measurements and modeled using the MAR-Model with parameters found by a numerical non-linear minimization (Nelder-Mead algorithm [75]) in MATLAB. The measurement results for each of three pairs of every cable were very similar, and the fitting was done using the mean of three measurements for each cable type. The minimization function is a least-squares one with outlier minimization, using the Huber method [61]. The results can be seen in figures 3.5 and 3.6 for the cable UW100. To characterize the quality of model, a $R^2$ statistical coefficient of determination is used [76]. It shows, how well the modeled curve corresponds to the measured one, and takes values in the range of 0 to 100%, with 100% characterizing a perfect fit.

The measured characteristic impedance in Fig. 3.6 shows some unexpected behavior starting at roughly 2 MHz, both in magnitude and phase, where a rather flat curve was expected. Such behavior can be seen at high frequencies, measuring rather short cables (also found for instance in [77]) and can have several explanations. First, the difference of electrical length of short and open termination due to parasitic capacitances violates the assumption behind equations (3.15), used to calculate secondary line parameters. This causes errors, especially at frequency points, where the cable length corresponds to odd multiples of $\lambda/4$. Using measurement standards other than open and short for cable measurement, for instance 50 Ω and 150 Ω, shows much better results at $(2m+1)\lambda/4$ points. This can be also seen in Fig. 3.6a, black curve. Still, $m \cdot \lambda/2$ points are however definitely out of range. The downside of such measurements is lower accuracy at low frequen-

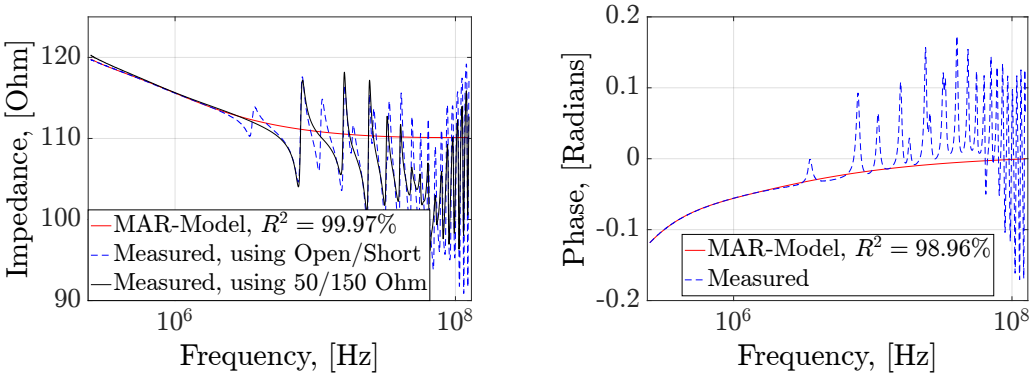


(a) Magnitude of $Z_0$ (b) Phase of $Z_0$

Figure 3.6: Characteristic impedance of UW100 cable under normal pressure

cies, which is due to lower precision of termination resistors. The second reason could be the non-uniformity of the measured transmission line, which in all calculations above is assumed to be perfectly homogeneous. Nevertheless, the used model is physically-based and allows the prediction of the characteristic impedance at higher frequencies using only the lower frequency part of measured impedance and the whole curve of propagation constant. The $R^2$ parameter is in this case calculated only for the used lower frequency part of measured $Z_0$. In this case the modeled high-frequency values of magnitude and phase of characteristic impedance show the physically expected behavior: flat magnitude curve, having its floor roughly from 50 MHz, and zero phase floor. In the following sections only the modeled curves will be shown, with corresponding $R^2$ factors.

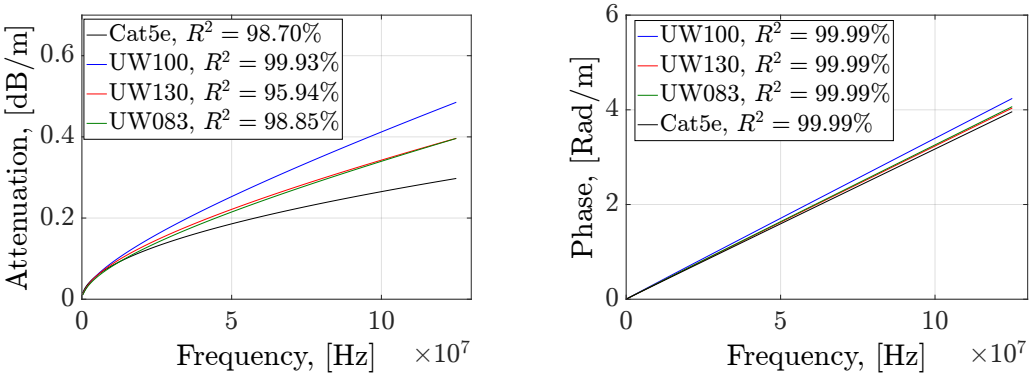


(a) Attenuation $\alpha$ (b) Phase $\beta$

Figure 3.7: Propagation constant of different cables under normal pressure

The modeling results for other cables can be seen in Figures 3.7 and 3.8.

In terms of attenuation, seen in Fig. 3.7a, both generations of the same cable are very similar. The thin UW100 cable has a slightly higher attenuation (roughly 0.1 dB/m at 125 MHz), despite the fact that all measured cables have the same AWG26 gauge. The Cat5e cable shows the lowest attenuation, starting at 12 MHz and getting increasingly better with increasing frequency, compared to underwater cables, with roughly 0.1 dB/m at 125 MHz. In terms of quality of model parameters fit, it seems that the UW130 cable of new generation is rather difficult to model, compared to other tested cables. Still, the value of $R^2 = 95.94\,\%$ means the model precision better than 5 %.

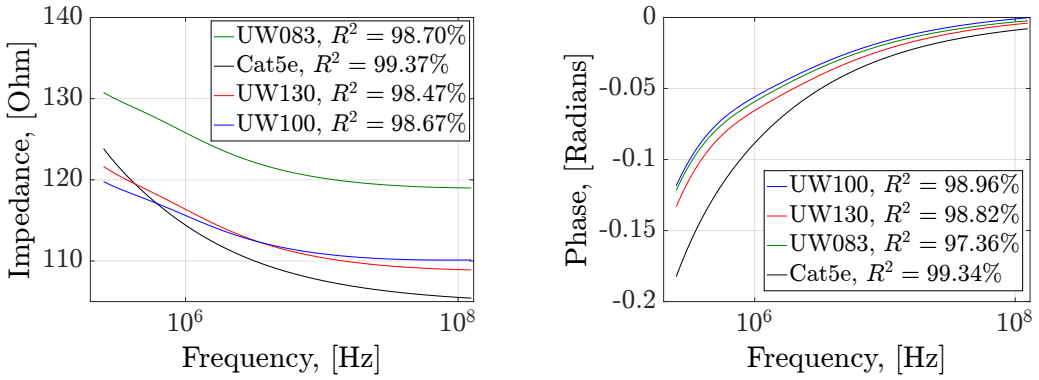


(a) Magnitude of $Z_0$ (b) Phase of $Z_0$

Figure 3.8: Characteristic impedance of different cables under normal pressure

Interesting enough, the characteristic impedance, shown in Fig. 3.8a, is quite different for all measured cables. While UW130 and UW100 tend to have almost the same impedance, roughly 110 Ω at 100 MHz, UW083 (an old version of UW130) shows the impedance of $Z_0 \simeq 120\Omega$. Taking into account that UW100 is used to build the data network, the newer version of the main bus cable appears to be better matched. Nevertheless, all cables' impedances, including Cat5e cable, are within specifications.

### High Pressure Measurements

To study the behavior of underwater cables under high pressure, the Atlas own water-filled pressure tank was used. The tank is usually used to test the integrity and some electrical characteristics of underwater components under high pressure.

The cables were mounted inside the tank, with 0.5 m cable ends outside the tank, to allow for the measurements. This required an additional post-measurement de-embedding, to remove the influence of these 0.5 m cable ends.

After the tank door was closed, all the cables were measured at four pressure steps: 11, 31, 51, and 71 bar, corresponding to sea depth 100, 300, 500, and 700 meters respectively. Unfortunately, the tank control equipment has a quite low pressure precision (±5 bar), especially at low pressure, and has no automatic control. The measurement results can be interpreted relatively, showing the trend, but a precise mathematical description of physical phenomena cannot be achieved due to these inaccuracies.

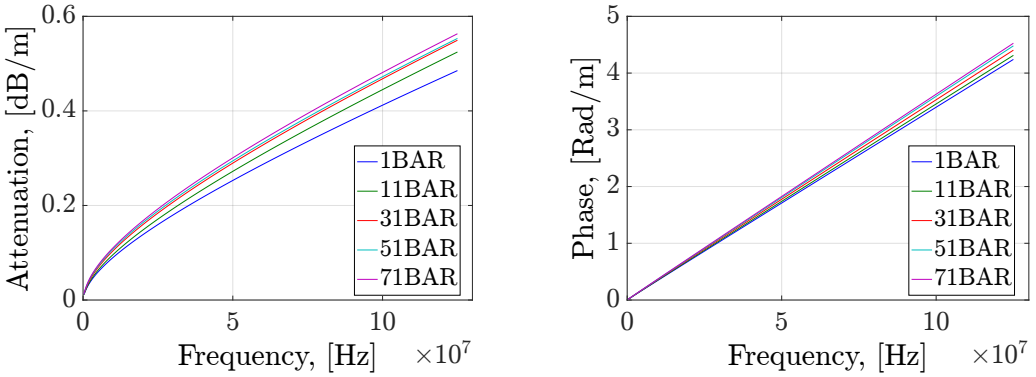


(a) Attenuation $\alpha$ (b) Phase $\beta$

Figure 3.9: Propagation constant of UW100 cable under pressure

The behaviour of the propagation constant under pressure can be studied with the example of the UW100 cable, Fig. 3.9. Both the attenuation and the phase constant are increasing with increasing pressure. This effect is quite pronounced with an about 16 % higher attenuation under 71 bar, compared to normal pressure attenuation, measured at 100 MHz, and shall be taken into account in channel modelling.

The parameters of a twisted pair cable, which is essentially a two-wire transmission line, can be defined as a function of its geometry (Chapter 10 in [47], also Chapter 2 in [46]):

$$\begin{aligned} C &= \frac{\pi\epsilon_0\epsilon_r}{\operatorname{acosh}(D/d)}\,, \qquad L = \frac{\mu_0\mu_r}{\pi}\operatorname{acosh}(D/d)\,, \\ Z_0 &= \frac{1}{\pi}\sqrt{\frac{\mu_0\mu_r}{\epsilon_0\epsilon_r}}\operatorname{acosh}\left(\frac{D}{d}\right), \end{aligned} \tag{3.19}$$

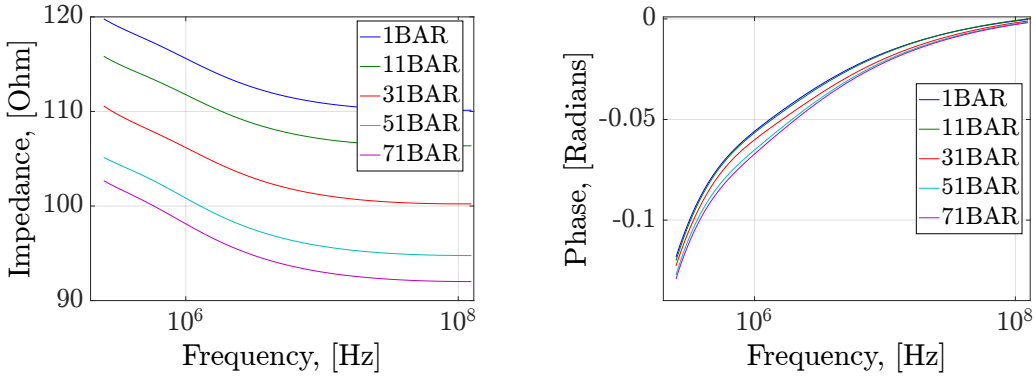


(a) Magnitude of $Z_0$

(b) Phase of $Z_0$

Figure 3.10: Characteristic impedance of UW100 cable under pressure

with primary transmission line parameters $C$ and $L$, characteristic impedance $Z_0$, relative permittivity $\epsilon_r$ and permeability $\mu_r$ of the isolator between the wires with diameter $d$, separated by a distance $D$.

Assuming the constant permittivity and permeability, as well as nearly constant wire diameter [3], the only parameter that can change strongly is the distance between the wires $D$. Rising pressure can possibly only reduce the distance between the conductors, decreasing the value of $D$. The expression for $Z_0$ in (3.19) depends on the inverse hyperbolic cosine, which decreases with decreasing argument $D$. Thus, the theoretically predicted behavior would be a decreasing characteristic impedance with increasing pressure. As can be seen in Fig. 3.10a, this is actually the case with UW100.

Similar to UW100 example, also the other underwater cables were measured. The results are depicted in a more compact form in figures 3.11 and 3.12, where propagation constant and magnitude of characteristic impedance at 100 MHz are shown. The behavior at other frequencies is very similar and this compact form allows easy comparison between different cable types.

All the cables have shown increased attenuation and phase constant under pressure, UW100 and UW130 seem to reach the floor at 50 bar - depending on materials and mechanical structure used, the cables are already compressed to some minimum and one does not see an effect from a further pressure increase.

Two pieces of UW083 type cable of different lengths were used to study the influence of calibration and de-embedding inaccuracy on the final mea-

[3] Or at most getting reduced very slightly in case of stranded wires, which could be a reason for higher attenuation under pressure. Besides, the measurements under normal pressure afterwards have shown, that this change is not residual.

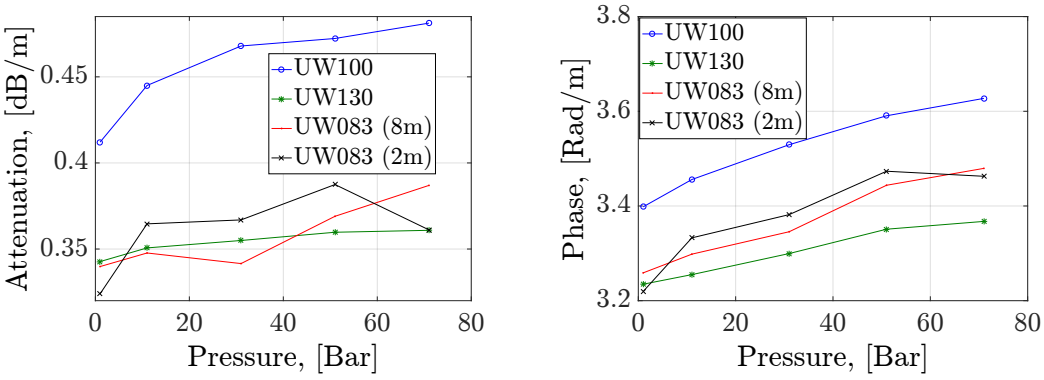


(a) Attenuation $\alpha$ (b) Phase $\beta$

Figure 3.11: Propagation constant of different cables under pressure at 100 MHz

surement result. The attenuation of a longer piece is almost linearly increasing with the pressure, except for one point at 30 bar, where it does not seem to reach its floor. The shorter piece shows a completely different, quite unexpected, trend. This can be a sign of an inaccurate de-embedding: half of the cable should be eliminated from the measurements and only a 1 m piece experiences high pressure. The 30 bar point outlier can be seen both in Fig. 3.11a and Fig. 3.11b, the possible explanation could be a sudden pressure loss, while the measurement was taken.

The characteristic impedance of different underwater cables in Fig. 3.12 shows a similar trend for all cable types. Comparing UW130 and UW083 (8 m piece) it is obvious, that the newer version has better mechanical properties, resulting in the characteristic impedance less dependent on the pressure. Starting from 50 bar both cables have almost the same $Z_0$, but the change of impedance value is about 17 % for UW083 and under 10 % for UW130, compared to starting values.

The outlier at 30 bar, seen in Fig. 3.11 for UW083, cannot be found in Fig. 3.12, which is quite strange, if a sudden pressure loss would have occurred. At the time of writing, there is no other plausible explanation for this behavior.

### 3.4.2 Two-Port Linear Bus Structure Measurements

While a single cable can be measured, using the method of the previous subsection, where the VNA was measuring the reflection factor (corresponds to S11), the measurements of a more complex structure, like a bus system,

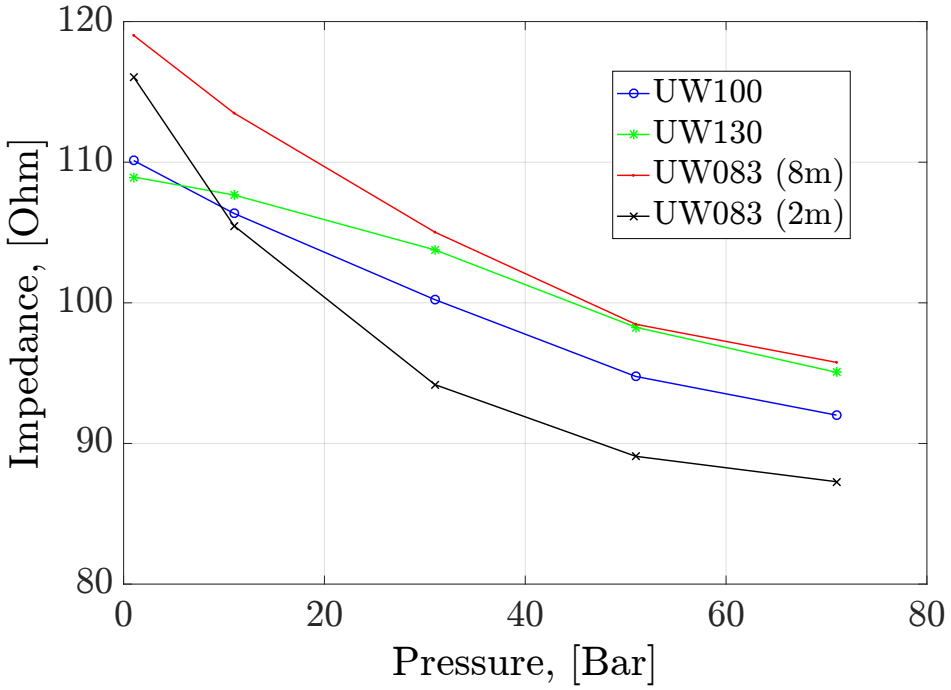


Figure 3.12: Magnitude of $Z_0$ of different cables under pressure at 100 MHz

require two-port VNA measurements of all scattering parameters. The S-parameter matrix $\mathbf{S} = \left(\begin{smallmatrix} S11 & S12 \\ S21 & S22 \end{smallmatrix}\right)$ describes any two-port network completely, similar to ABCD parameters. The measurement of these parameters requires matched terminations instead of open and short conditions a the DUT terminals, which are difficult to achieve at high frequencies.

### Two-port Set-Up and Calibration

The previously used VNA can directly measure S-parameters. However, similar to the one-port set-up, one needs baluns to provide impedance and balance-unbalance conversion. The whole two-port set-up, depicted in Fig. 3.13, naturally uses two baluns of the same type at two BNC ports of VNA.

The following parameters of the network analyzer are used for all two-port measurements:

- Source power: -10 dBm
- Intermediate (mixer) frequency: 1 kHz

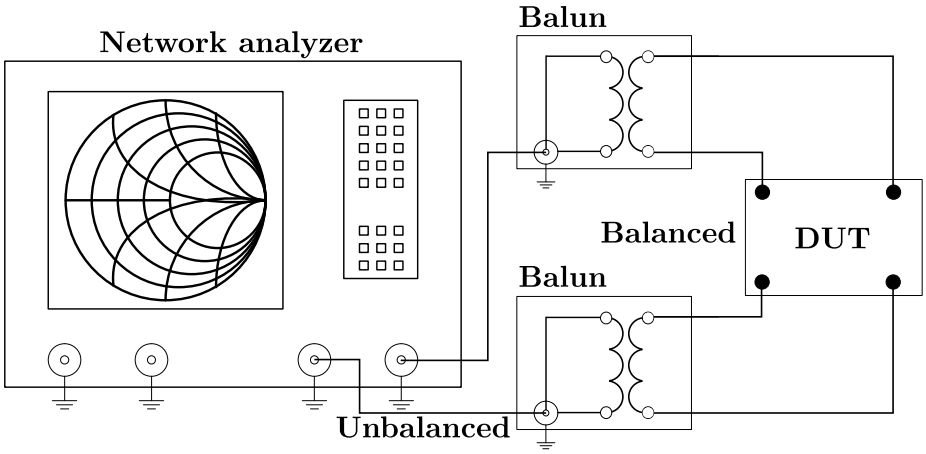


Figure 3.13: Two-port measurement set-up

- Start frequency: 250 kHz
- Stop frequency: 125 MHz
- Number of frequency points: 2001
- Frequency sweep scale: logarithmic

For the two-port calibration, a well-known Short-Open-Load-Through (SOLT) method is used, utilizing a 12-term error model [78]. A more recent method from [79], already mentioned in the one-port calibration subsection, could also be used at this point. However it does not seem to provide better accuracy than SOLT at the frequencies of interest. Besides, the math behind is more complicated and the choice of equations is not obvious, depending on used standards. In any case, all four S-parameters need to be measured, even if the interest is in only one of them, e.g., $S_{21}$ (insertion loss).

### Measurement and Modeling Results

For model verification purposes two similar bus structures, each with three taps (or nodes), have been measured. Figure 3.14 shows the general schematics of both structures. The difference between the two is the used cable and segment lengths: while the first is build using usual Cat5e cable, the second uses two underwater cables (UW083 and UW100), already measured in previous subsection.

The measured $S_{21}$ parameter can be directly interpreted as insertion loss (expressed in dB here), because both ports use the same, purely resistive

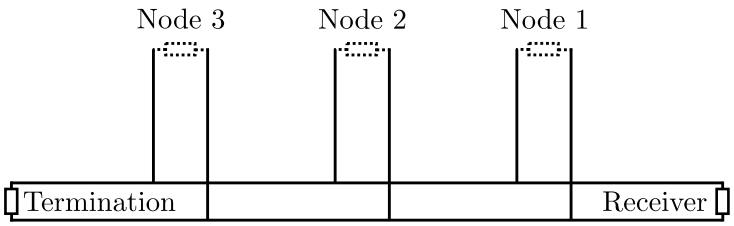


Figure 3.14: Bus system structure, used for model verification

reference impedance of 100 Ω:

$$S_{21(\text{meas})}(f) = -20\log_{10}(|S_{21}|) \quad \text{dB}$$

The measured insertion loss is then compared to the modeled one, using Eq. (3.7) from Section 3.3. The ABCD model is developed, using the previously measured and fitted cable models, with the corresponding segment lengths.

The first bus system measurement and modeling results can be seen in Fig. 3.15a. The segment cable length are as follows: 1 m between stubs, 0.2 m branch cable, 1 m from last stub to termination and from first stub to receiver. One port of the VNA was always connected to the receiver node (see Fig. 3.14), another port was connected to one of the source nodes, with others being terminated by 100 Ω resistors. The connectors, used to build up the system were not taken into account. This could be a reason for insertion loss modeling error in Fig. 3.15b, especially at higher frequencies. Nevertheless, the maximum absolute error of about 0.3 dB can be considered a good result, also $R^2$ factors all exceeding 96%.

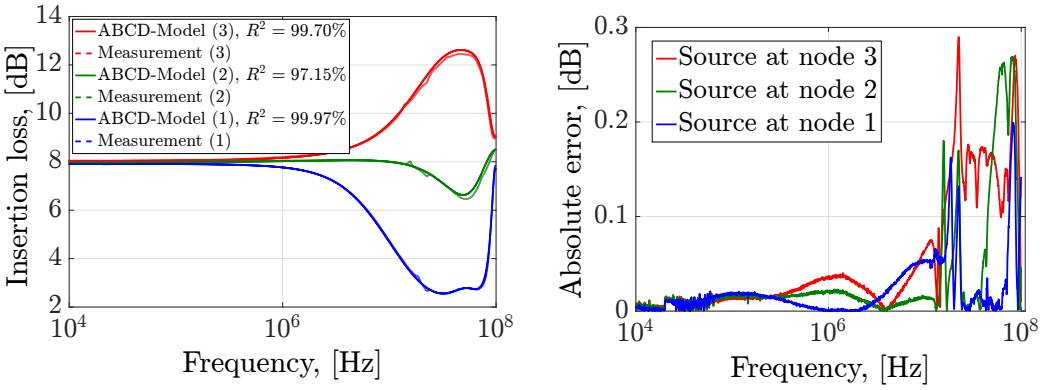


(a) Insertion loss

(b) Insertion loss absolute error

Figure 3.15: Modeling of the bus structure with 3 stubs

Another measured and modeled bus structure is a segment with 3 stubs of an actual underwater cabling, having 32 stubs. This real-world example is less homogeneous, than the first bus structure: it has 2.5 m UW083 cable between the stubs and 2 m from last stub to the cable end and from first stub to the receiver. First and second branches are made of 0.7 m UW100 cable and the third one is 5 m long. All the measurements are done between the receiver connector and the third (longest branch) source node, while other nodes are left open and the end of the line is not terminated.

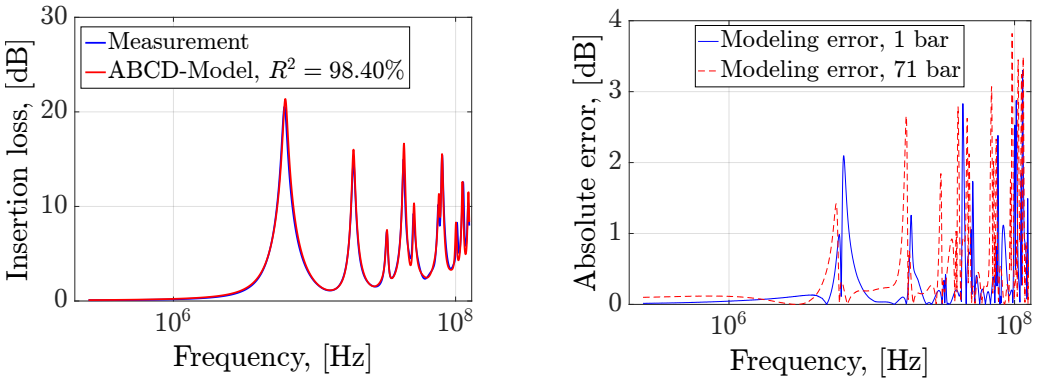


(a) Insertion loss

(b) Insertion loss absolute error

Figure 3.16: Modeling of the underwater bus structure with 3 stubs at normal pressure

The channel has an obvious frequency selectivity, as can be seen in Fig. 3.16, with notches because of the bridge taps. Under normal pressure this channel can be fairly well modeled, even though the maximum absolute error can be as high as 3 dB. These error peaks occur at the notches - regions of high attenuation - so that the relative error is still under 10%. The connectors and moreover the splices can be the source of these errors, similar to the first example.

The same measurement under pressure (71 bar) shows similar behavior in Fig. 3.17. The absolute error is slightly higher than under normal pressure. The reason for this could be the impedance mismatch between cables of different types, connectors and splices. The mismatch is getting higher with increasing pressure and neglecting connectors and splices in the model produces higher error levels under pressure.

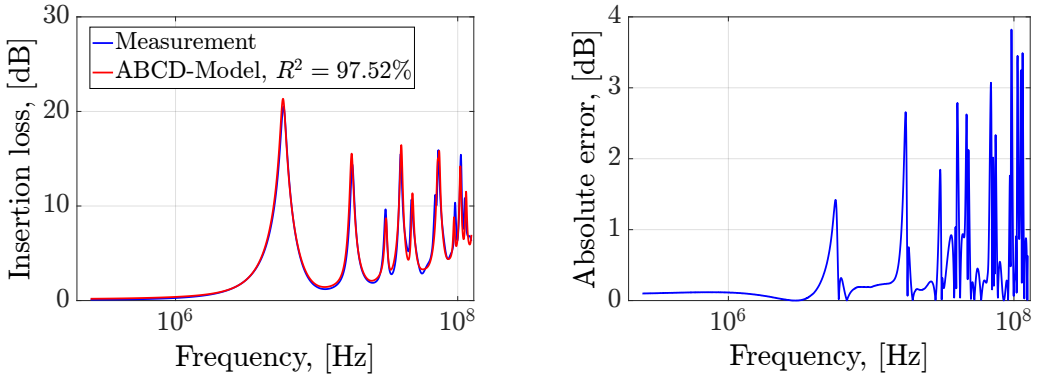


(a) Insertion loss

(b) Insertion loss absolute error

Figure 3.17: Modeling of the underwater bus structure with 3 stubs at high pressure (71 bar)

### 3.4.3 Crosstalk Measurements

Crosstalk describes the possible coupling between different pairs in a cable. This section deals with characterizing this coupling through measurements. First, a measurement set-up, using the VNA is introduced, as well as near-end and far-end crosstalk definitions, followed by the measurement results of underwater cables under normal and high pressure, compared to crosstalk in Cat5e cables.

As stated in the previous section, a typical underwater cable has multiple twisted pairs. These wires can be used as parallel channels for different sensors, as redundant channels, or as a mixture of both strategies – channel bonding. In all these cases the crosstalk becomes a source of noise, which is measured here. The future applications can possibly take advantage of this knowledge by applying MIMO or spectrum management algorithms.

#### Crosstalk Measurement Set-Up

A non-ideal twisted-pair cable, even used in a differential mode, radiates electromagnetically and thus induces signals in neighboring twisted pairs [80]. This signal is called crosstalk and is one of the noise sources in a communication system. Figure 3.18 illustrates two types of crosstalk, Near-End Crosstalk (NEXT): a signal, produced by near-end transmitter, which affects a near-end receiver; and Far-End Crosstalk (FEXT): a signal, produced by near-end transmitter, which affects a far-end receiver or vice versa.

To measure the levels of both NEXT and FEXT, a two-port measurement set-up is needed. To the measurement set-up from Section 3.4.1, a second

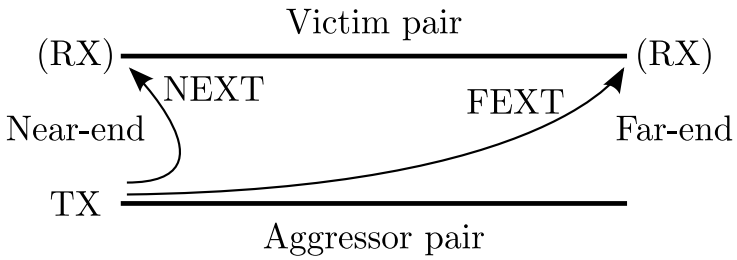


Figure 3.18: NEXT and FEXT Crosstalk

balun is added, with both baluns connected to two "external" ports of the network analyzer. During a NEXT measurement, one of twisted pairs (a 'victim') is connected to any one of the baluns, while another twisted pair on the same cable side (an 'aggressor') is connected to the other balun's balanced port. The far-end of both pairs are terminated with 100 Ω resistors. A FEXT measurement is analogue to NEXT measurement, the second balun is simply connected to an "aggressor" twisted pair on the far-end cable side, instead of connecting it on the same side, as the 'victim' is connected to its balun. The so-called Equal-Level Far-End Crosstalk (EL-FEXT) is the FEXT divided by the cable's transfer function.

Before these measurements can be evaluated, the set-up needs to be calibrated. A simple method of calibration in this case is a through-calibration, which includes only one measurement of both baluns, with balanced ports connected. Thus, the transfer function of both baluns is measured. The true measurement result can then easily be calculated by dividing a raw measurement by the calculated transfer function of both baluns.

### Measurement Results

The cables used during the crosstalk measurements were:

- 12m UW100 (B/W, R/W, Br/W)
- 8m UW130 (Bl/W, V/W, Br/W)
- 8m UW083 (Bl/B, V/B, Bl/W)
- 6m Cat5e AWG26 (Bl, Br, O)

with pair colors given in brackets.

A typical example of NEXT and FEXT as functions of frequency is given in Fig. 3.19. The general increase of coupling with frequency is a well-known phenomena, also taken into consideration by crosstalk models [80]. It is besides obvious that the crosstalk level between blue-white and violet-white

pairs is much higher than between other pairs. This is an expected behavior, as exactly these pairs are next to each other in a cable, such that the coupling could be expected to be high. Similar results were obtained with other underwater cables.

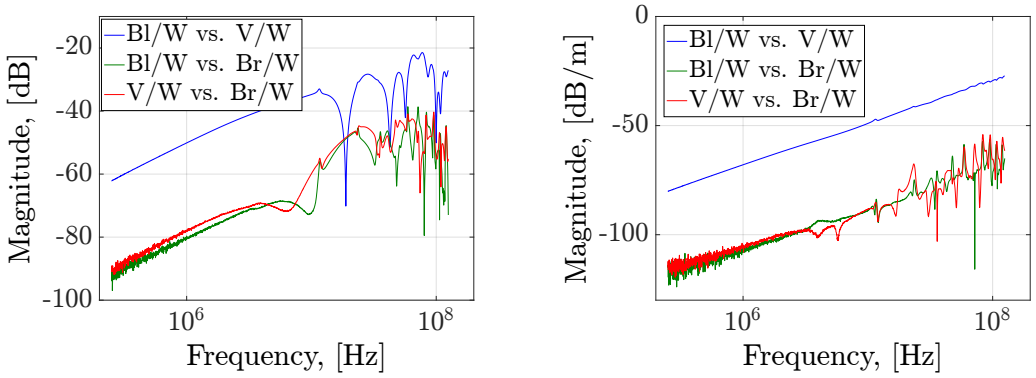


(a) Magnitude of NEXT (b) Magnitude of (EL-)FEXT

Figure 3.19: Crosstalk in UW130 under normal pressure

Unexpected, on the other hand, is the crosstalk level in underwater cables under pressure. Intuitively, pressing the pairs together should increase the coupling, analogue to the decreasing characteristic impedance through decreasing the distance between the wires in Section 3.4.1. This is only very slightly the case, as can be seen in Fig. 3.20. Other cables have shown a very similar behaviour and will not be shown here.

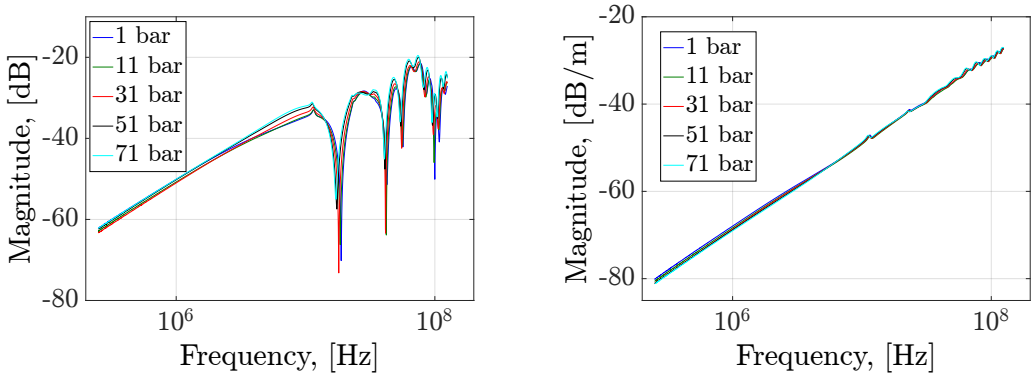


(a) Magnitude of NEXT (b) Magnitude of (EL-)FEXT

Figure 3.20: Crosstalk in UW130 under pressure

To produce a more compact readable form, only one, typically with high-

est magnitude, FEXT/NEXT curve for each cable type is considered in the following. Comparing the crosstalk magnitudes of the underwater cables under pressure to those of a standard Cat5e cable (see Figure 3.21), the conclusion is that the network cable has a considerably lower coupling between its pairs. It is well known, that the pairs in a Cat5e cable have different and variable twisting periods to avoid crosstalk. The tested underwater cables apparently do not try to avoid the coupling. Nevertheless, the crosstalk is quite different in these cables: while the UW130 cable is the worst of all, both in terms of higher NEXT and FEXT magnitudes, the UW083 cable has lower FEXT coupling and the UW100 cable has lower NEXT magnitude, almost comparable to the Cat5e cable.

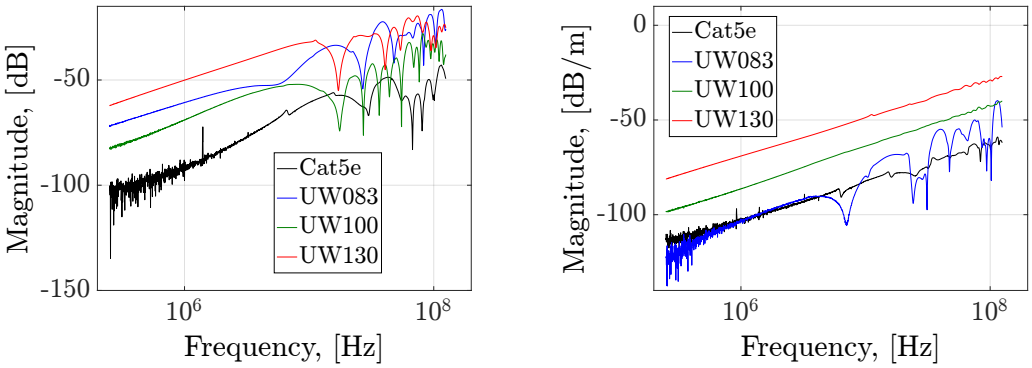


(a) Magnitude of NEXT

(b) Magnitude of (EL-)FEXT

Figure 3.21: Crosstalk of different cable types

### 3.4.4 Noise and its Modeling

One of the capacity limiting factors in any communication system is noise, which along with power constraints and channel distortion determines the Signal-to-Noise Ratio (SNR) at the receiver.

Different types of noise can be found in PLC systems ([81], [9]): colored background noise with low PSD, periodic and aperiodic impulsive noise, synchronous and asynchronous to the mains frequency. Originally the study of the PLC noise environment concentrated on in-house alternating current (AC) systems ([62], [82]), where the impulse noise due AC/DC converters and switching transients in the network is more pronounced. In recent years the direct current (DC) PLC in-vehicle systems became more popular. The main sources of impulsive noise in such systems are DC/DC converters and electric engines [83]. The in-vehicle noise and channel characterization has been

carried out in [84], [85], [86], and [83]. Similar results have been obtained for a spacecraft DC PLC differential system in [87].

An empirical model of the background colored Gaussian noise

$$N_{OMEGA} = \frac{1}{f^2} + 10^{-15.5} \text{ mW/Hz},$$

with $f$ - frequency in Hz is proposed for in-house PLC systems in [88], based on observations of real systems. Another model

$$N_A = -25 \cdot \log(f \cdot 10^{-6}) - 94 \text{ dBm/Hz}, \tag{3.20}$$

can be found in [89], which is much more pessimistic, as can be seen in Fig. 3.22. Even compared to the impulse noise measurement results in [83], this model has a similar PSD shape and level. Before the noise measurements of the real hardware are available, the model from Eq. (3.20) will be used in capacity calculations. The early noise measurement attempts shown in Fig. 3.23 suffer from a rather high noise floor due to the used spectrum analyzer setup. Nevertheless, it can be concluded that the used model does not exactly describe the actual noise environment, especially the high-frequency peaks.

Another classical noise source is crosstalk, due to coupling between different data lines. This type of noise is of great importance in VDSL systems, with many telephone pairs bundled into one cable. There are just a few publications (e.g. [90]), concerning crosstalk in PLC systems. In the in-house systems, which are unbalanced with respect to ground, this issue is rather an Electro Magnetic Interference (EMI) problem. The PSD masks limit the available bandwidth, thus reducing the interference. In currently developed in-vehicle DC PLC differential systems the cables are usually not bundled and crosstalk is negligible, also because of low-bandwidth operation.

Any digital multi-carrier system has practical constrains on the resolution of used Analog-to-Digital (A/D) and Digital-to-Analog (D/A) converters and transform logic (e.g. Fast Fourier Transform (FFT) blocks). The limited dynamical range of the components results in clipping of the time-domain signal, which is known to be a Gaussian random process with a high peak-to-average ratio. The overload and a quantization error in A/D-D/A converters can be considered to be additive overload and quantization pseudo-noise [91], [92]. In [93] an optimum value for the clipping ratio depending on the bit resolution for both uniform and non-uniform quantization is obtained, which optimizes the SNR. A simple model for both overload noise $N_o$ and (uniform) quantization pseudo-noise $N_q$, given in [94], assuming the amplitude

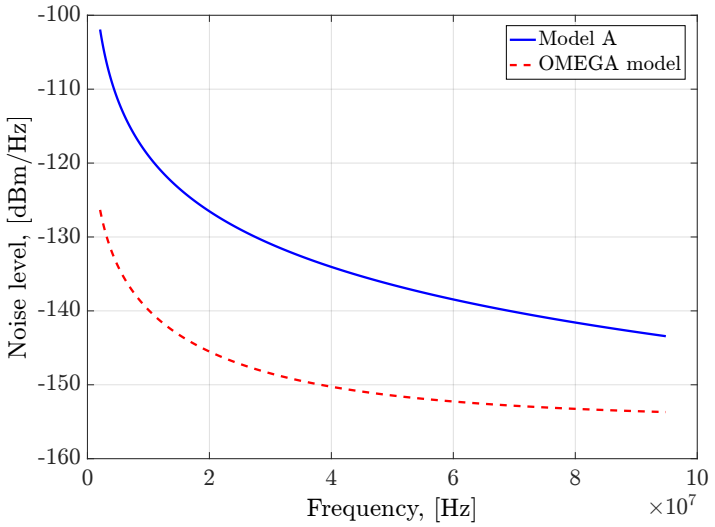


Figure 3.22: Background noise models

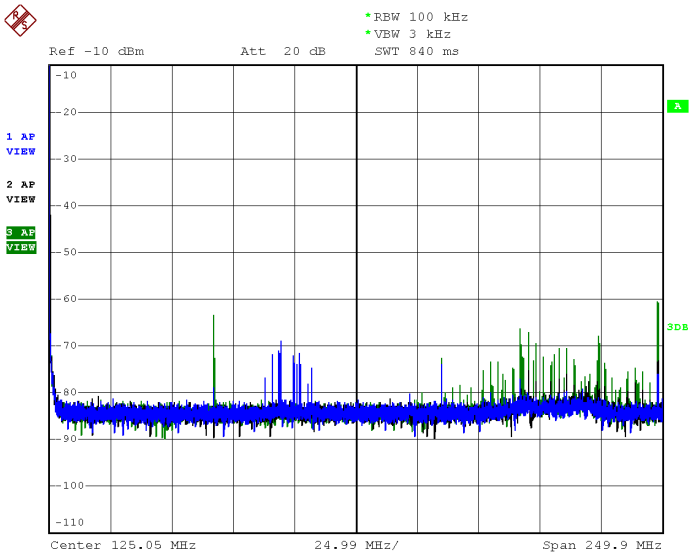


Figure 3.23: Background noise measured on a prototype board

distribution of multi-carrier time-domain signal to be Gaussian is

$$N_q = \frac{(k \cdot \sigma)^2}{3 \cdot M^2}, \quad N_o = \sqrt{\frac{2}{\pi}} \cdot \frac{\sigma^2}{k} \cdot \left(1 + \frac{2 \cdot k^2}{3 \cdot M^2}\right) \cdot e^{-k^2/2}, \tag{3.21}$$

where $\sigma$ is the standard deviation of the voltage waveform, $k$ is the number of standard deviations passed (voltage amplitude larger than $k \cdot \sigma$ results clipping in the A/D converter), and $M$ is the number of quantizer levels.

## 3.5 Channel Capacity of a Twisted Pair Linear Bus

The transfer function measurements and simulations of the twisted pair linear bus structures in Section 3.4.1 have revealed the frequency selectivity of such channels due to their multi-path nature ([62], [19]). Moreover, the Gaussian noise in PLC systems is generally non-white. A frequency-selective channel can be converted to an equivalent set of ($N_c \to \infty$) non-interfering Additive White Gaussian Noise (AWGN) flat sub-channels, called a parallel channel, assuming the independent noise across the sub-channels [95]. The calculation of the capacity $C_{N_c}$ for such a parallel channel is an optimization problem [27]

$$C_{N_c} = \max_{P_1, \cdots, P_{N_c}} W_i \sum_{i=1}^{N_c} \log\left(1 + \frac{P_i |H_i|^2}{N_i W_i}\right) , \tag{3.22}$$

$$\sum_{i=1}^{N_c} P_i = P, \quad P_i \geq 0, i \in [1, N_c] , \tag{3.23}$$

where $P_i$ is the power, allocated to each sub-channel, $H_i, N_i$, and $W_i$ are sub-channel transfer function, noise and bandwidth, respectively, and $P$ is the overall power constraint. The solution to this problem, using Lagrangian methods, is the optimal power allocation, usually referred to as water-filling [95], which converges to

$$P(f) = \left(\frac{1}{\lambda} - \frac{N_i W_i}{|H(f)|^2}\right)^+ ,$$

where the constant $\lambda$ satisfies

$$\sum_{i=1}^{N_c} P_i = P .$$

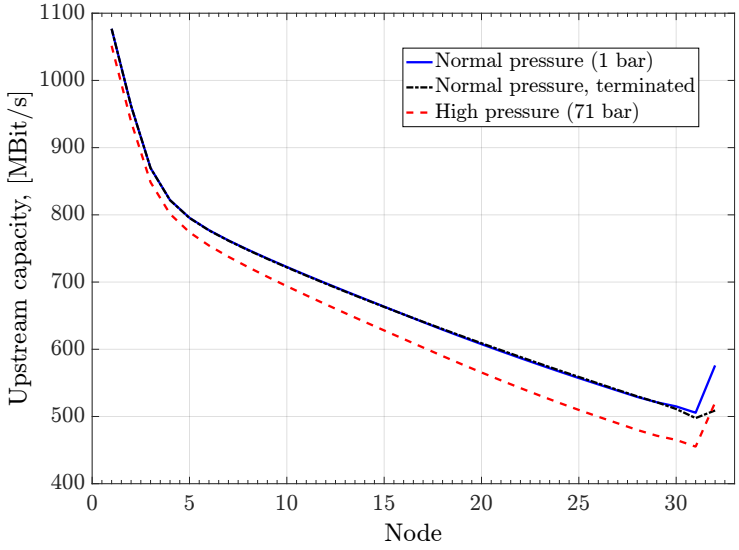


Figure 3.24: Capacity of the upstream channel

The capacity of a twisted pair linear bus was studied, using the water-filling algorithm, implemented in MATLAB, with transfer function and noise modeling, according to (3.4.1) and (3.4.4), respectively. The modeled linear bus structure has 32 taps, connecting 32 nodes to the base station, and uses 1 m underwater cables from Section 3.4.1 between the taps and as branches. The cable length between the base station and the first node is 60 m. The calculated capacities for each node are depicted in Fig. 3.24 for the upstream (2-100 MHz bandwidth) and in Fig. 3.25 for the downstream (0.2-1 MHz bandwidth). The common power constraint in both cases is $P = 0.1$ W for any transmitter. The capacities for the upstream channel are calculated assuming TDMA sharing: transmitter at the currently used node and the receiver (base station) have an input/output impedance of 100 Ω, while the other nodes have the high input impedance (125 kΩ). The downstream channel is a broadcast channel: all nodes (receivers) have an input impedance of 20 kΩ, while base station transmitter has an output impedance of 100 Ω, which matches roughly the characteristic impedance of the used cables.

The cable on the far end (from base station's point of view) is not terminated. Although this is usually done in baseband unmodulated bus systems to prevent and attenuate reflections, this also results in a power loss due to the voltage divider. A multi-carrier system takes the multi-path effects (e.g. Inter-Symbol Interference (ISI)) already into account and the capacities

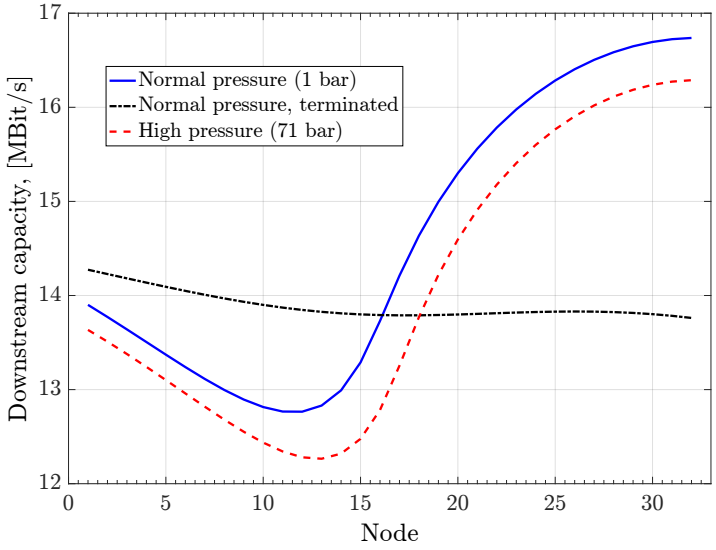


Figure 3.25: Capacity of the downstream channel

in a non-terminated system compared to the terminated one of the same configuration in the download path (at high frequencies) are almost identical, as can be seen from Fig. 3.24. The downstream path (at low frequencies) is more homogeneous in the terminated system, with comparable or slightly higher overall capacity in the non-terminated system (Fig. 3.25).

The available capacities in the underwater bus system are reduced under high pressure, as can be seen from figures 3.24 and 3.25. The capacity loss depends not only on the pressure, but it is also proportional to the distance between a node and the base station: the pressure influence, investigated in Section 3.4.1, is more pronounced, as the cable length (or equivalently the number of segments) increases.

# Chapter 4

# Fundamentals of Multi-Carrier Modulation

Multi-carrier systems are known to be well suited for a channel with ISI [96], and thus the primary transmission system candidate for the multipath channel of a linear bus structure from the previous chapter. The basic idea behind any multi-carrier (sometimes called multi-channel) system is to partition the available channel bandwidth into a set of independent narrow-band sub-channels, transmitting a large number of bits in parallel at a low symbol rate. This chapter describes the basics of the multi-carrier data transmission, essential for any practical implementation.

## 4.1 Multi-Carrier Channel Partitioning

Channel partitioning methods play a key role in any multi-carrier system, dividing a given channel into a set of $N$ parallel, ideally independent, sub-channels. Every sub-channel can be considered an individually modulated single-carrier channel. The number of sub-channels $N$ should be large enough, so that the frequency response across the bandwidth of each sub-channel is flat - this eliminates ISI and thus the need for complex equalization [97].

The partitioning can be done using any set of so-called orthonormal basis functions $\phi_i(t)$, characterized by

$$\int_{-\infty}^{\infty} \phi_m(t)\phi_n(t)dt = \delta_{mn}, \text{ where } \delta_{mn} = \begin{cases} 1 & m = n \\ 0 & m \neq n \end{cases},$$

and using single carriers with the frequencies $f_k = k/T,\ k = 0,..N$ for the sub-channels in a baseband system, with symbol period $T$, assuming equal

sub-channel bandwidths. In this basic multi-tone system a generic modulator in the transmitter modulates the vector output by the corresponding basis functions $\phi_k(t)$, creating Quadrature Amplitude Modulation (QAM) (or Pulse Amplitude Modulation (PAM)) sub-symbols. In the demodulator, a matched filter is used to process each sub-channel as a baseband signal, followed by a maximum-likelihood detector to independently reconstruct the transmitted sub-symbols [98].

An optimal choice of basis functions, remaining orthogonal for an AWGN channel, is shown to be the set of eigenfunctions of the channel [98]. Being theoretically optimal, the eigenfunctions (or modes) are not well suited as basis functions for a practical system: as the eigenfunctions of different channels differ, the basic hardware should be flexible and reconfigurable and thus complicated. Besides, such design would require an infinite delay [97]. For this reason, practical systems use partitioning methods that do not depend on the channel and can be efficiently implemented, like the Discrete Fourier Transform (DFT) or Discrete Cosine Transform (DCT).

### 4.1.1 DFT-Based Partitioning for OFDM/DMT

Orthogonal Frequency Division Multiplexing (OFDM) and its baseband variant Discrete Multi-Tone modulation (DMT) are two most frequently used multi-carrier modulation methods, used in both wire-line (e.g. ADSL) and wireless (e.g. Long-Term Evolution (LTE)) transmission systems, respectively. Both use a cyclic prefix, prepending the last $\nu$ time-domain samples at the beginning of each symbol, consisting of $N$ samples, such that $s_{-k} = s_{N-k}$ , for $k = 1, ..., \nu$. When the cyclic prefix is longer than the channel impulse response, the received time-domain sequence $\mathbf{r}$, distorted by the channel, can be represented as

$$\mathbf{r} = \tilde{\mathbf{H}}\mathbf{s} + \mathbf{n} \tag{4.1}$$

with a cyclic channel (convolution) matrix $\tilde{\mathbf{H}}$, which has an important property that Singular Value Decomposition (SVD) can be replaced by the eigendecomposition

$$\tilde{\mathbf{H}} = \mathbf{M}\mathbf{\Lambda}\mathbf{M}^H , \tag{4.2}$$

with a single unitary vector coding matrix $\mathbf{M}$ ($\mathbf{M}\mathbf{M}^H = \mathbf{M}^H\mathbf{M} = \mathbf{I}$) for both receiver and transmitter and a square diagonal eigenvalue matrix $\mathbf{\Lambda}$. In case of both DMT and OFDM [98], the vector coding matrix $\mathbf{M}$ corresponds to

a normalized IDFT matrix $\mathbf{F}^H$, given by

$$\mathbf{F}^H = \frac{1}{\sqrt{N}} \begin{bmatrix} 1 & 1 & 1 & \cdots & 1 \\ 1 & e^{-j\frac{2\pi}{N}} & e^{-j\frac{2\pi}{N}2} & \cdots & e^{-j\frac{2\pi}{N}(N-1)} \\ 1 & e^{-j\frac{2\pi}{N}2} & e^{-j\frac{2\pi}{N}4} & \cdots & e^{-j\frac{2\pi}{N}2(N-1)} \\ \vdots & \ddots & \vdots & \vdots & \vdots \\ 1 & e^{-j\frac{2\pi}{N}(N-1)} & e^{-j\frac{2\pi}{N}2(N-1)} & \cdots & e^{-j\frac{2\pi}{N}(N-1)^2} \end{bmatrix} . \tag{4.3}$$

Keeping in mind that the QAM-modulated input $\mathbf{x}$ and output $\mathbf{y}$ of an OFDM/DMT system are explicitly related to the corresponding time-domain sequences as

$$\begin{aligned} \mathbf{s} &= \mathbf{F}^H\mathbf{x} \quad \text{(Transmitter IDFT)} \\ \mathbf{y} &= \mathbf{F}\mathbf{r} \quad \text{(Receiver DFT)} , \end{aligned}$$

the system description of Eq. 4.1 can be rewritten as

$$\begin{aligned} \mathbf{y} = \mathbf{F}\mathbf{r} &= \mathbf{F}\tilde{\mathbf{H}}\mathbf{s} + \mathbf{F}\mathbf{n} = \\ &= \mathbf{F}\mathbf{F}^H\mathbf{\Lambda}\mathbf{F}\mathbf{F}^H\mathbf{x} + \mathbf{F}\mathbf{n} = \\ &= \mathbf{\Lambda}\mathbf{x} + \mathbf{F}\mathbf{n} , \end{aligned}$$

exploiting the relation in Eq. 4.2. For each sub-carrier, the $N \times N$ diagonal matrix $\mathbf{\Lambda}$ contains channel coefficients in DFT-domain, such that the channel is partitioned in independent sub-carriers, usually denoted as channel diagonalization. The use of a cyclic prefix and the cyclic extension of the channel results thus in a simple and efficient implementation (e.g. FFT realization of DFT), and can eliminate ISI, when the channel impulse response is shorter than the cyclic prefix length.

For the channel input signal $\mathbf{s}$ to be real, the input sequence $\mathbf{x}$ has to be conjugate symmetric. In practice, this means that the DFT size should be twice the length of $\mathbf{x}$, that is $2N$, in the case of the baseband transmission.

An alternative basis function set, proposed in [99], is based on the DCT instead of the DFT. It requires just half the bandwidth, compared to a DFT, but only if the input data sequence $\mathbf{x}$ is real, obtained by real-valued modulation (e.g. PAM, Binary Phase Shift Keying (BPSK)) [100]. It has, however, no real advantage when using higher order complex-valued modulation schemes (e.g. QAM), which are expected to be possible on a low-noise twisted-pair bus channel with relatively low attenuation.

## 4.2 Bit-Loading in DMT Systems

The baseband DMT and OFDM systems can use the fixed constellation size (or the equal number of bits $b_n$) across the $N$ sub-channels, or the bits $b_n$

and energy $\epsilon_n$ distribution can be optimized for a given channel. An example of such a bit-loading algorithm is the water-filling from Section 3.5, which is in fact known to calculate the optimum distribution.

Depending on the objective, a bit-loading algorithm typically either maximizes the data rate under total power and bit-error ratio (BER) constraints (rate-adaptive bit-loading, Eq. (4.4)) or minimizes the total energy $E$ at desirable data rate and BER (margin-adaptive bit-loading, Eq. (4.5)) [98]. Yet another possibility, proposed in [101], is to minimize the error probability. There are also algorithms with multiple objectives like in [102], [103].

$$\left.\begin{aligned} \max_{P_n} b &= \sum_{n=1}^{N} b_n \ , \\ \text{subject to } P &= \sum_{n=1}^{N} P_n \ , \end{aligned}\right\} \quad \text{Rate-adaptive} \tag{4.4}$$

$$\left.\begin{aligned} \min_{P_n} P &= \sum_{n=1}^{N} P_n \ , \\ \text{subject to } b &= \sum_{n=1}^{N} b_n \ , \end{aligned}\right\} \quad \text{Margin-adaptive} \tag{4.5}$$

Typically, a SNR Shannon gap approximation $\Gamma$

$$\Gamma = \frac{1}{3}\left[Q^{-1}\left(\frac{SER}{4}\right)\right]^2 \ , \ Q(x) = \int_x^\infty \frac{e^{-u^2/2}}{\sqrt{2\pi}} du \ , \tag{4.6}$$

at the desired symbol error ratio (SER) for QAM constellations [98] (also exists for $M$-ary Phase Shift Keying (PSK), see [104]) is used to calculate values for $b_n$:

$$b_n = \frac{1}{2}\log_2\left(1 + \frac{P_n g_n}{\Gamma}\right) \ ,$$

where $g_n$ is a sub-channel gain.

Without coding, it is impossible to implement an encoder/decoder for fractional bits, resulting from the optimum water-filling. A number of sub-optimal discrete units bit-loading algorithms, approximating the water-filling distribution, has been developed to overcome this problem. On the one hand, there are algorithms, adopting water-filling results (e.g. rounding gap-based bit-loading) to get the finite bit granularity. Chow's algorithm is one of the first examples [105], [106]. On the other hand, there are optimum discrete loading algorithms, based on greedy methods. An approach, first suggested

in [107] and significantly improved in [108]. As the greedy methods are already optimum (at least in a margin-adaptive case), the research in this field concentrates on introducing less computationally complex algorithms ([109], [110], [111]), possibly utilizing unequal-BER requirements across the sub-channels [112].

## 4.3 PAR Reduction

A well-known drawback of multi-carrier modulation methods (e.g. DMT), is a high Peak-to-Average Ratio (PAR), defined as

$$20 \log_{10} \left( \frac{V_{peak}}{V_{RMS}} \right) \text{ dB} ,$$

where $V_{peak}$ is the peak voltage of the time-domain waveform and $V_{RMS}$ is the Root Mean Square (RMS) of that waveform [97]. The time-domain signal is a sum of $N$ random variables and can be considered to be a Gaussian random process, according to the central limit theorem [98]. In a DMT system with many sub-carriers and possibly large constellations the PAR is estimated to be around $20 \log_{10}(\sqrt{3}N)$ dB [91]. A VDSL2 system with $N = 2000$ has thus a theoretical PAR of roughly 38 dB. All analog components, such as amplifiers and filters should remain linear within the wide range of input levels and the line driver has to be capable of accommodating the peak power.

In practice, components with lower power input range are used. The probability of very large values in a Gaussian distribution is very small and in such events signal clipping is just tolerated, taken into account as noise. Increasing the quantization step size in A/D-D/A converters can help avoid clipping, but introduces higher quantization noise. An optimum trade-off between clipping and quantization noise is described in Section 3.4.4.

Over the years, many methods for PAR reduction have been introduced (e.g. Selected Mapping, Partial Transmit Sequences [113]), which would reduce clipping probability. Currently, tone injection and reservation methods, originally studied by Tellado [114] and extended in [115] and [116], are widely used in practice, mostly due to their low complexity. The basic idea behind the tone reservation is to define a subset of available sub-channels that are used to produce a Dirac-like signal, which iteratively reduces the time-domain peaks, generated by the remaining data sub-channels [97].

## 4.4 Channel and Noise Estimation

The bit-loading algorithms above expect the sub-channel's SNR to be known. While the information about the channel conditions can be a priori known in a simulated environment, a real system needs to estimate the sub-channel gains and noise levels. Typically, a repeated sequence of $M$ symbols known to both the transmitter and receiver is used in a process, known as training, for channel identification. For a fully periodic training signal, the receiver averages the time-domain sequence $\mathbf{y_m}$

$$\bar{\mathbf{y}} = \frac{1}{M} \sum_{m=1}^{M} \mathbf{y_m} \ ,$$

and estimates each sub-channel frequency response $\hat{H}_n$, using the DFT of the averaged time-domain signal $Y_{m,n}$ as

$$\hat{H}_n = \sum_{n=1}^{M} \frac{Y_{m,n}}{X_{m,n}} \ , \tag{4.7}$$

where $X_{m,n}$ is the DFT of the $m$'th training symbol $x_m$ on sub-channel $n$ [97].

Noise estimation, assuming that the noise is zero-mean, is similar to the frequency response identification [97]. Using previously estimated $\hat{H}_n$, a residual error $E_{m,n}$ on sub-channel $n$ is defined as

$$E_{m,n} = Y_{m,n} - X_{m,n}\hat{H}_n \ .$$

Transmitting $M + 1$ training symbols (the first symbol flashes the channel and is not taken into account) and estimating the variance of error $E_{m,n}, m = 2, ..M + 1$, results in the noise variance estimate on sub-channel $n$

$$\hat{\sigma}_n^2 = \frac{1}{M} \sum_{m=2}^{M+1} |E_{m,n}|^2 \ . \tag{4.8}$$

Clearly, for both channel and noise estimation increasing the number of symbols $M$ in the training sequence results in a better SNR estimation accuracy. The ADSL G.992.1 standard recommends, for instance, a pseudo-random sequence of 16384 symbols for channel estimation, while [97] shows that less than 500 symbols could be enough to limit the error to 0.1 dB.

As soon as the channel is known, a simple frequency-domain equalizer (Frequency-domain Equalizer (FEQ)) compensates for scaling and rotation

due to sub-channel gains. It uses a single complex multiplication

$$\hat{X_n} = Y_n \frac{1}{\hat{H}_n} .$$

to zero the noise-free error between the input $X_n$ and $\frac{Y_n}{H_n}$ [98].

## 4.5 Synchronization in Multi-Carrier Systems

A baseband multi-carrier system, DMT, needs two synchronization tasks to be solved: symbol (or frame) and sampling frequency synchronization.

The symbol synchronization ensures that the incoming symbol fits into an FFT window. The FFT can only produce meaningful results if all the data samples in the time domain belong to one symbol, otherwise the orthogonality is violated. The absolute position of the first sample within the symbol is almost arbitrary, as an offset in the time domain introduces a phase shift in the frequency domain, which can easily be corrected by the FEQ. The methods of symbol boundary acquisition can be either blind or data-aided. In data-aided methods, a special training sequence (a preamble), preceding a data frame, is constructed at the transmitter and the receiver can search for the predefined sequence to obtain the symbol start position $\theta$. The preamble-based timing synchronization is known to be more robust [117], [118], [119], but also requires additional bandwidth for the preamble transmission. The blind synchronization ([120], [121]) uses redundancy of the cyclic prefix, only. Also a mix of two worlds has been proposed in [122]. In all cases, either the Minimum Mean-Squared Error (MMSE), the Maximum Likelihood (ML), or Maximum Correlation (MC) methods can be used [123].
The maximum correlation method uses a coefficient

$$\gamma(m) = \sum_{k=m}^{m+\nu-1} r(k) r^*(k+N) , \tag{4.9}$$

where $N$ and $\nu$ are the symbol length and the length of cyclic prefix in samples, respectively, and $r(k)$ represents the received signal, to define an MC estimator [124]

$$\hat{\theta}_{MC} = \arg\max_m \gamma(m) .$$

The ML and MMSE estimators ([121], [125]) are given by

$$\hat{\theta}_{MMSE} = \arg\max_m |\gamma(m)| - \Phi(m) ,$$

$$\hat{\theta}_{ML} = \arg\max_m |\gamma(m)| - \rho\Phi(m) ,$$

with $\gamma(m)$ given in (4.9) and $\Phi$ and $\rho$ defined as

$$\Phi(m) = \frac{1}{2} \sum_{k=m}^{m+\nu-1} |r(k)|^2 + |r(k+N)|^2 \ ,$$
$$\rho = \frac{\mathrm{SNR}}{\mathrm{SNR}+1} \ .$$

Depending on the duration of the channel impulse response, the performance of blind methods can degrade, because the cyclic prefix will be more corrupted by ISI and does not strictly represent the copy of last $\nu$ samples of the symbol any more. The maximum correlation in this case does not necessarily points to the start sample and the synchronization is not precise. This is usually the case in multi-path dispersive channels, for which robust blind methods have been proposed, for instance, in [117] and [126].

Another source of synchronization inaccuracy is, of course, noise, which is not taken into account by any of the above-mentioned estimators. In practice, averaging over some DMT symbols is used to obtain a clearer indication of the symbol boundaries [97].

The sampling frequency synchronization can be done after the initial coarse symbol sync and also uses the correlation coefficient from Eq. (4.9). The frequency offset $\epsilon$ between the receiver and transmitter sampling clocks is then estimated as

$$\hat{\epsilon} = -\frac{1}{2\pi} \angle\gamma(\hat{\theta}) \ .$$

It should be noted that the above methods are mostly used for the coarse, or initial, synchronization. Fine timing acquisition and tracking are discussed in [127] in more detail.

# Chapter 5

# Time-Domain Equalization

The Time-domain Equalizer (TEQ) in DMT systems concentrates on shortening the impulse response, reducing the required length $\nu$ of the cyclic prefix and is placed at the receiver, as shown in Fig. 5.1. Without an equalizer, the required length of the cyclic prefix leads on many channels to a high data rate loss, defined as $\nu/N$, with $N$ carriers. Increasing $N$ would minimize the excess-bandwidth but would also result in increased hardware complexity and latency. Introducing a TEQ (basically an FIR filter) can thus help minimizing $\nu/N$, keeping the implementation complexity low.

Non-blind (or trained) TEQ methods were the first proposed in [128], [129], whereas blind algorithms, exploiting the redundancy of the cyclic prefix, are only recently becoming popular [130]. Originally, the only concern of TEQ taps calculation and adaptation algorithms was making the impulse response shorter than the cyclic prefix (or guard interval). Maximizing the channel capacity, or alternatively the geometric mean of the SNR, while keeping the impulse response short was first treated in [131] and [132] and is an optimization criterion in all most recent algorithms. An overview and evaluation of TEQ design approaches, including the MMSE TEQ, maximum shortening SNR [133], and per-tone equalization are given in [134].

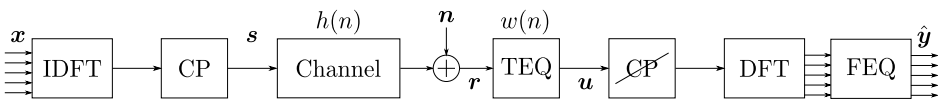


Figure 5.1: DMT system with a time-domain equalizer (TEQ) at the receiver. The serial/parallel conversions are included in the DFT implementation (FFT).

## 5.1 Channel Impulse Response Shortening

A method that can be called classical nowadays is to introduce an equalizer before performing the FFT, with FIR coefficients $\mathbf{w}$ defined such that for the overall effective impulse response $h_{eff}(n) = h(n) \star w(n)$, $L_{h_{eff}} \leq \nu$ is strictly fulfilled. The first algorithms to calculate such a shortening time-domain equalizer (TEQ) for a multi-carrier system were introduced by Chow and Cioffi in [135]. The main idea of this group of algorithms is to introduce a reference system with the desired impulse response and find a solution, which minimizes the minimum squared error (MMSE) between the reference and the actual TEQ output.

Another approach, maximum shortening signal-to-noise ratio (MSSNR), first introduced by Melsa in [133], maximizes the energy in the part of the effective impulse response, covered by the available cyclic prefix ($\mathbf{h}_{win}$), or alternatively minimizes the energy of its tail ($\mathbf{h}_{wall}$), which are defined as (see also Fig. 5.2)

$$\mathbf{h}_{win} = \begin{bmatrix} h_{eff}(\Delta) \\ h_{eff}(\Delta+1) \\ \vdots \\ h_{eff}(\Delta+\nu) \end{bmatrix} \equiv \mathbf{H}_{win}\mathbf{w} \ , \tag{5.1}$$

$$\mathbf{h}_{wall} = \begin{bmatrix} h_{eff}(0) \\ \vdots \\ h_{eff}(\Delta-1) \\ h_{eff}(\Delta+\nu+1) \\ \vdots \\ h_{eff}(L_{h_{eff}}-1) \end{bmatrix} \equiv \mathbf{H}_{wall}\mathbf{w} \ , \tag{5.2}$$

where $\Delta$ is the channel delay.

Quite some other algorithms exist that improve or generalize these two approaches. The paper by Martin et al. [134] is a good reference that not only lists many of those algorithms but also introduces a unified mathematical framework for almost all of them. Considering an optimization problem

$$\hat{\mathbf{w}}_{opt} = \arg \max_{\hat{w}} \frac{\hat{\mathbf{w}}^T\mathbf{B}\hat{\mathbf{w}}}{\hat{\mathbf{w}}^T\mathbf{A}\hat{\mathbf{w}}} \ , \tag{5.3}$$

with vector $\hat{\mathbf{w}}$ containing the estimated optimum TEQ coefficients, the solution turns to be the generalized eigenvector of the matrix pair $(\mathbf{B}, \mathbf{A})$ and requires the computation of $\hat{\mathbf{w}}$, corresponding to the largest generalized eigenvalue $\lambda$

$$\mathbf{B}\hat{\mathbf{w}} = \lambda\mathbf{A}\hat{\mathbf{w}} \ .$$

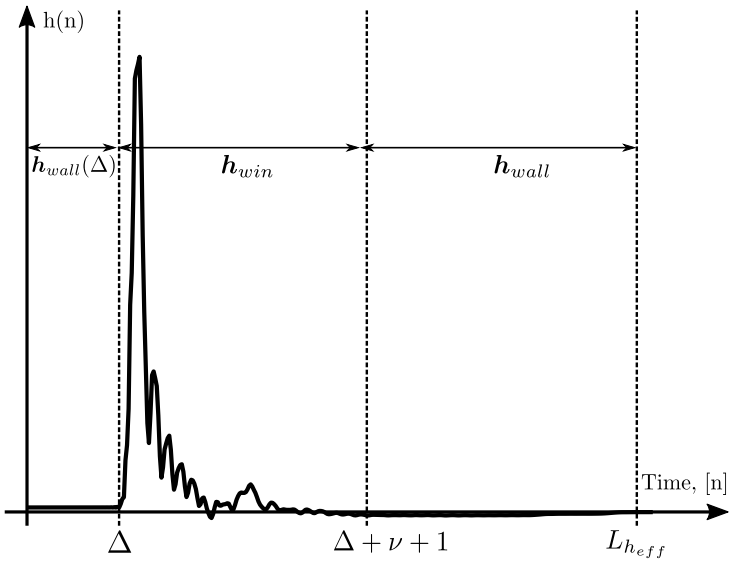


Figure 5.2: Wall and window parts of an impulse response

The values for matrices $(\mathbf{B}, \mathbf{A})$ depend on the channel (attempt to model the sub-channel SNR) and different constraints: the MMSE-TEQ in [135] is described, for instance, by

$$\begin{aligned} \mathbf{A} &= \mathbf{R}_{rr} - \mathbf{R}_{rs}\mathbf{R}_{ss}^{-1}\mathbf{R}_{sr} \ , \\ \mathbf{B} &= \mathbf{e}_j\mathbf{e}_j^T \ , \end{aligned}$$

with elementary vector $\mathbf{e}_j$ and correlation matrices $\mathbf{R}_{ss}$, $\mathbf{R}_{rr}$, $\mathbf{R}_{sr}$, and $\mathbf{R}_{rs}$ of the input $\mathbf{s}$ and channel and noise distorted output $\mathbf{r}$, as defined in Fig. 5.1, respectively. The MSSNR-TEQ is defined by

$$\begin{aligned} \mathbf{A} &= \mathbf{H}_{wall}^T\mathbf{H}_{wall} + \mathbf{R}_{nn} \ , \\ \mathbf{B} &= \mathbf{H}_{win}^T\mathbf{H}_{win} \ , \end{aligned} \tag{5.4}$$

with $\mathbf{H}_{win}$ and $\mathbf{H}_{wall}$ being Toeplitz matrices of the original impulse response in equations (5.1) and (5.2), and $\mathbf{R}_{nn}$ is the noise correlation matrix [134].

## 5.2 Capacity-optimizing TEQ

By shortening the impulse response, a TEQ can indirectly improve the resulting data rate by eliminating the ISI and ICI noise. Some time after the first TEQ designs were introduced, it has been recognized that data rate maximization should be the ultimate goal of a TEQ design. Early attempts to follow this strategy include [131] and [132].

The optimization parameter for a rate-maximizing TEQ is the number of bits $B$ per OFDM/DMT symbol with $N$ sub-carriers at a given fixed symbol rate, which is given by

$$B = \sum_{j=1}^{N} b_i = \sum_{j=1}^{N} \log_2 \left(1 + \frac{\mathrm{SNR}_j}{\Gamma_j}\right) , \tag{5.5}$$

where the SNR-Gap $\Gamma$ is formulated as in Chapter 4, Eq. (4.6). The sub-channel SNR dependency on the TEQ coefficients $\mathbf{w}$ can be in general represented as a generalized Rayleigh quotient

$$\mathrm{SNR}_j = \frac{\mathbf{w}^T \tilde{\mathbf{B}}_j \mathbf{w}}{\mathbf{w}^T \tilde{\mathbf{A}}_j \mathbf{w}} . \tag{5.6}$$

Incorporating this formulation into Eq. (5.5) leads to

$$B(\mathbf{w}) = \sum_{j=1}^{N} \log_2 \left(1 + \frac{\mathrm{SNR}_j}{\Gamma_j}\right) \tag{5.7}$$

$$= \sum_{j=1}^{N} \log_2 \left(\frac{\mathbf{w}^T(\Gamma_j \tilde{\mathbf{A}}_j + \tilde{\mathbf{B}}_j)\mathbf{w}}{\mathbf{w}^T(\Gamma_j \tilde{\mathbf{A}}_j)\mathbf{w}}\right) = \tag{5.8}$$

$$= \log_2 \left(\prod_{j=1}^{N} \frac{\mathbf{w}^T \mathbf{B}_j \mathbf{w}}{\mathbf{w}^T \mathbf{A}_j \mathbf{w}}\right) , \tag{5.9}$$

where $\mathbf{A}_j = \Gamma_j \tilde{\mathbf{A}}_j$ and $\mathbf{B}_j = \Gamma_j \tilde{\mathbf{A}}_j + \tilde{\mathbf{B}}_j$ are model-dependent matrices, used to represent the SNR. In the unified framework of [134], maximizing $B(\mathbf{w})$ is formulated as an optimization problem with multiple generalized Rayleigh quotients

$$\hat{\mathbf{w}}_{opt} = \arg \max_{\hat{w}} \log_2 \left(\prod_{j \in S} \frac{\hat{\mathbf{w}}^T \mathbf{B}_j \hat{\mathbf{w}}}{\hat{\mathbf{w}}^T \mathbf{A}_j \hat{\mathbf{w}}}\right) , \tag{5.10}$$

where $S$ is the set of active data-loaded carriers. An optimum solution to such an optimization problem is not yet formulated, such that the existing algorithms use approximations for SNR model (the examples for $\mathbf{A}_j$ and $\mathbf{B}_j$ can be found in [134]) and gradient-descent strategy to find at least a local optimum.

A similar optimization approach has been used in the one of the first attempts [132] to achieve the highest possible data rate. The algorithm calculates the overall capacity at all carrier locations, taking into account noise

and channel response, shaped by the equalizer. A downhill simplex optimization algorithm is then used to find the FIR coefficients of the equalizer which result in the maximum data rate.

Yet another approach is to maximize the bit rate on every single carrier independently, thus maximizing also an overall capacity – the so-called per-tone equalization [136], [137]. The filters are implemented after the DFT, so that they are, in fact, frequency-domain equalizers. Being possibly an optimal solution in terms of the capacity, it is the most demanding approach in terms of complexity, nevertheless also used as an option for DSL implementations.

## 5.3 Application of TEQ in a DC-PLC System

Simulations with both shortening (MSSNR) and bit-rate maximizing (SIM-TEQ from [132]) TEQs were performed to motivate the application of time-domain equalization in DC-PLC sensor networks, particularly in the new MC-TP bus. The linear bus channel is modeled according to the approach, described in Chapter 3. Two different cable types are used to build the exemplary underwater sensor network (Fig. 5.3): main cable type, used between the branch segments and to connect the bus to a base station (with cable lengths $l_M$ and $l_R$, respectively); branch cable type with length $l_B$. The cable model parameters are given in Table 5.1. The identification for different cable configurations has the form $l_R.l_M.l_B$ for cable lengths in meters. The main goal of such a sensor network is to provide data from spatially distributed sensors to a single base station, so that the data transmission from sensors to a single receiver is considered here.

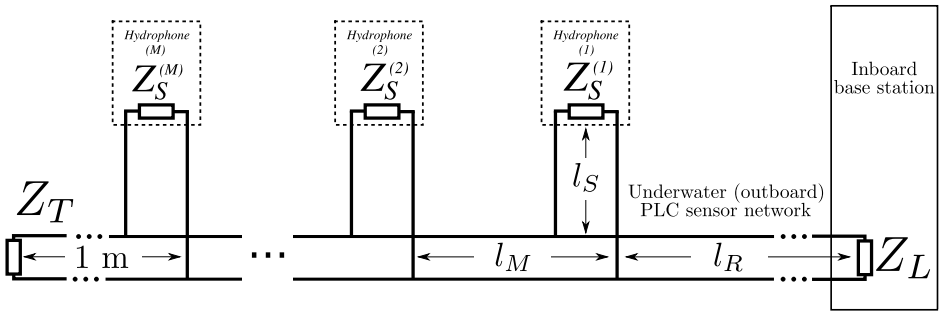


Figure 5.3: An example bus system for simulations

The sensor bus is used in TDMA mode with constant load and termina-

tion impedance $Z_L = Z_T = 100\ \Omega$ and configurable source impedances:

$$\begin{aligned} Z_S^n &= 100\ \Omega\ , \\ Z_S^m &= 30\ \mathrm{k}\Omega\ , \quad m \neq n, \quad m, n \in [1, M]\ , \end{aligned}$$

simulating an active state of the current sensor $n$ in a system with $M + 1$ nodes.

The simulated noise environment includes quantization and clipping from ADC/DAC ($n_{DAC}$) and fixed-point arithmetic ($n_{FP}$) modeled as white noise sources. The main external source of colored noise is the power supply chain, modeled by [89]

$$n_{ext} = -25 \log 10(f_{\mathrm{MHz}}) - 94\ \frac{\mathrm{dBm}}{\mathrm{Hz}}\ , \tag{5.11}$$

Both ISI and ICI ($n_I$) caused by the tail of the effective impulse response, not covered by the cyclic prefix, are modeled according to [138]. The contribution to $\mathbf{R}_{nn}$ in Eq. (5.4) is limited to $n_{ext}$ and $n_{DAC}$.

The achievable bit distribution $b_i\ , i \in [1; N]$ per frame is calculated by an optimum discrete loading algorithm (Levin-Campello, [108]) for a fixed bit error ratio ($10^{-7}$), zero margin and coding gain and $-20$ dBm mean power. The effective data rate in $\left[\frac{\mathrm{bit}}{\mathrm{s}}\right]$

$$R_i = \frac{f_S}{2N + \nu} \sum_{j=1}^{N} b_j\ , \tag{5.12}$$

with sampling frequency $f_S = 250$ MHz takes into account the length of the cyclic prefix $\nu$. An optimum constant cyclic prefix length in samples (see

| MAR-Model Parameter | Main | Branch |
|---|---|---|
| $R_0$, [Ω/km] | 250.76 | 240.94 |
| $L_\infty$, [H/km] | 5.513e-04 | 5.867e-04 |
| $a$ | 2.25 | 2.04 |
| $b$ | 3.35 | 3.33 |
| $c$ | 6.05 | 6.08 |
| $\delta$ | 7.33e-03 | 1.29e-02 |
| $C_{1\mathrm{MHz}}$, [F/km] | 4.83e-08 | 5.10e-08 |

Table 5.1: Cable model parameters

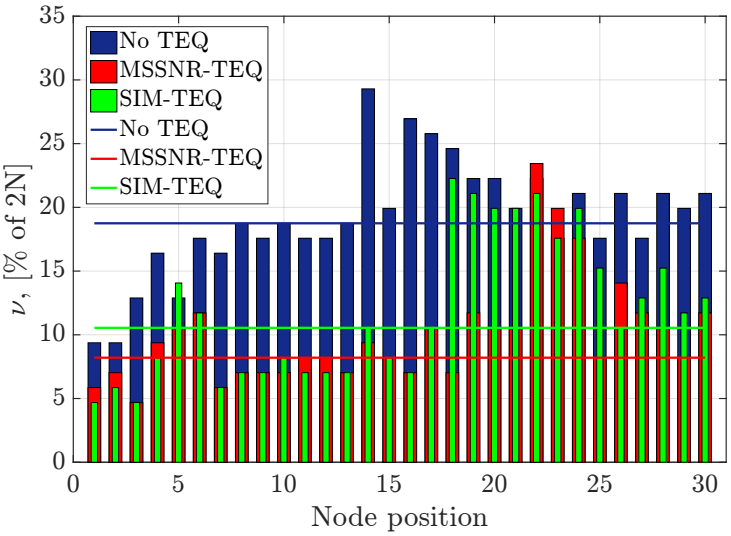


Figure 5.4: Estimated optimum cyclic prefix lengths in a 30 node bus system, cable configuration $l_R.l_M.l_B = 50.1.1$, $N = 128$. The horizontal lines represent the optimum constant length of the cyclic prefix.

Fig. 5.4), common for all nodes, is calculated as

$$\hat{\nu}_{\text{opt}} = \arg\max_{\hat{\nu}} \sum_{i=1}^{M} R_i \ , \tag{5.13}$$

with $R_i$ according to Eq. (5.12).

### 5.3.1 Bus Termination Influence

From transmission line theory, it is known that the far end of a bus system should be terminated ($Z_T$ in Fig. 5.3) to avoid reflections. The absence of termination will result in a longer impulse response but will also increase mean signal power at the receiver, due to avoiding a voltage divider. In case of a termination fault, it is important to be able to retain operation of the sensor network.

A multi-carrier system is flexible enough to cope with such problems and even more so, when a TEQ is used. The comparison of data transmission performance in an exemplary 30 node sensor network with different cable configurations is shown in figures 5.5-5.7.

The optimum $\nu$ in the case of an open-ended system (without termination) is always larger than in a terminated system, as can be seen in

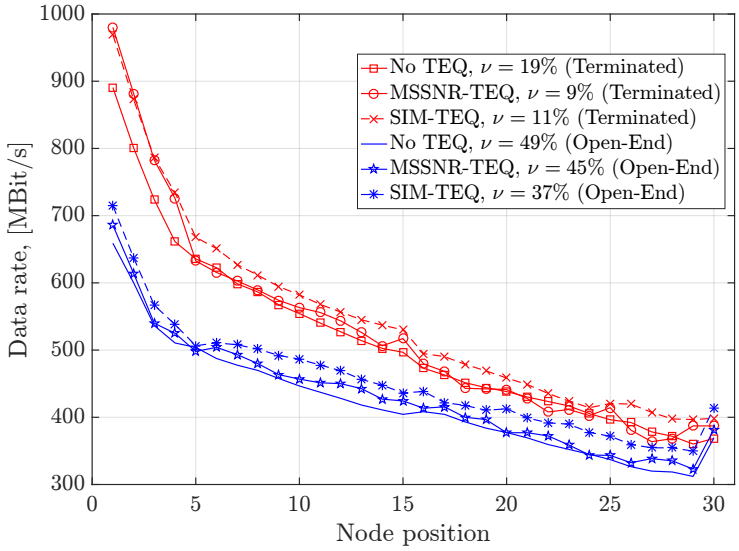


Figure 5.5: Data rates in a 30 node bus system with constant CP, with and without termination, cable configuration $l_R.l_M.l_B = 50.1.1$, $N = 128$

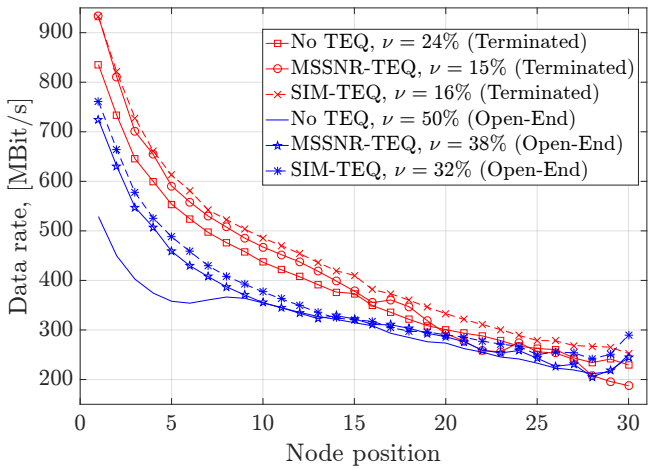


Figure 5.6: Data rates in a 30 node bus system with constant CP, with and without termination, cable configuration $l_R.l_M.l_B = 50.1.2$, $N = 128$

Table 5.2. This is an indirect indication of a longer impulse response, as expected. Obviously, the rate-maximizing SIM-TEQ always outperforms the shortening-only MSSNR-TEQ in a system without termination. Quite the opposite case can be observed for various cable configurations with termination – the MSSNR-TEQ allows a slightly shorter cyclic prefix in this case. Nevertheless, the performance of the SIM-TEQ in terms of the data rate is always better, which is a good demonstration of the statement that a shorter impulse response does not automatically lead to an optimum data rate.

| | | $l_R.l_M.l_B$ | | | | |
|---|---|---|---|---|---|---|
| | | 50.1.1 | 50.1.2 | 50.2.1 | 50.2.2 | 100.1.1 |
| Terminated | No TEQ | 19% | 24% | 11% | 13% | 18% |
| | MSSNR TEQ | 9% | 15% | 4% | 6% | 8% |
| | SIM TEQ | 11% | 16% | 4% | 8% | 9% |
| Open-End | No TEQ | 49% | 50% | 32% | 40% | 50% |
| | MSSNR TEQ | 45% | 38% | 10% | 20% | 45% |
| | SIM TEQ | 37% | 32% | 9% | 10% | 36% |

Table 5.2: Optimum lengths of the cyclic prefix in a 30 node bus system, in percent of DMT symbol length, $N = 128$

Depending on cable configuration, the SIM-TEQ can increase the effective data rate up to 10 %, compared to a system without TEQ (see Fig. 5.8).

Both TEQ designs show higher gains in a non-terminated bus system, but still do not manage to match the performance of a terminated system. The better performing nodes, located closer to the receiver, loosing at most, while the farthest (20 to 30, depending on configuration) can even boost performance with a TEQ.

In a sensor network with equal sensor priorities and data rate demands (e.g. an underwater hydrophone network) the node with the lowest performance limits the overall system performance, if TDMA time slots are equally distributed. In this special case no data rate degradation due to termination fault will occur, if a data-rate maximizing TEQ is used. An optimum scenario seems to be the default usage of termination and a shortening-only TEQ, which can be implemented very efficiently. Switching to a more advanced rate-maximizing TEQ can be a fall-back option when disturbances in the cabling system are detected.

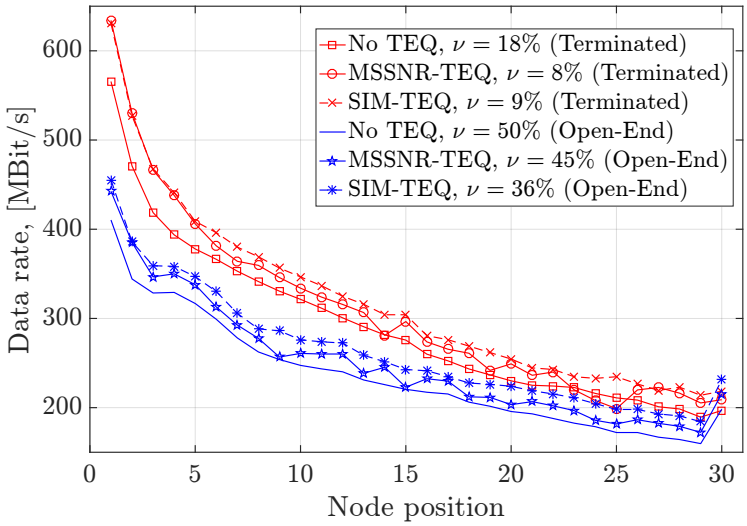


Figure 5.7: Data rates in a 30 node bus system with constant CP, with and without termination, cable configuration $l_R.l_M.l_B = 100.1.1$, $N = 128$

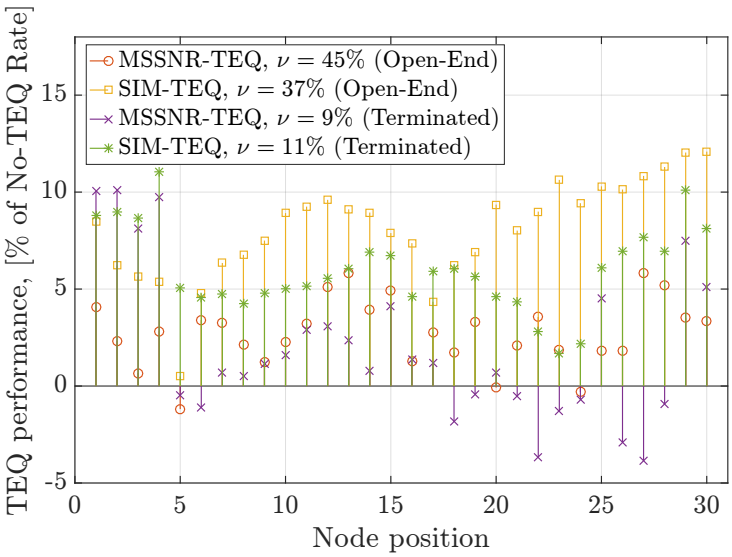


Figure 5.8: Data rate gain with a TEQ compared to the corresponding data rate without TEQ in a 30 node bus system with constant CP, with and without termination, cable configuration $l_R.l_M.l_B = 50.1.1$, $N = 128$

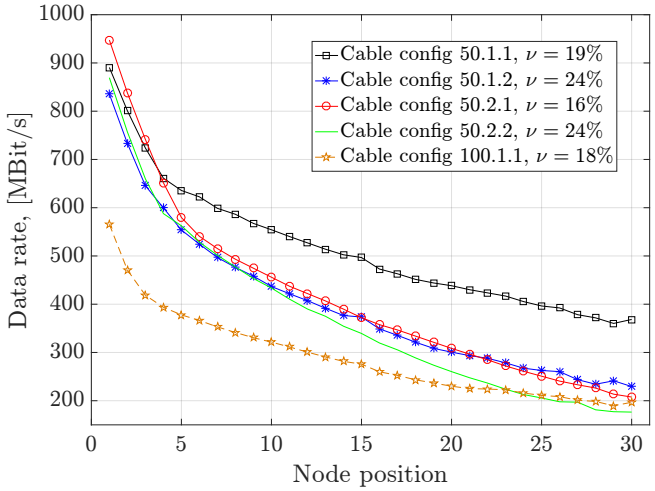


Figure 5.9: Data rates in a 30 node bus system with a fixed and equal cyclic prefix for all nodes, with termination, without TEQ, $N = 128$

### 5.3.2 Bus Configurations

As far as the cable configuration is concerned, the common recommendation for a bus system is to keep the branches or bridged taps as short as possible. This is confirmed in Fig. 5.9. Increasing the segment lengths between the taps has a negative effect, especially on the far nodes, simply due to the higher attenuation. This also holds for a typically longer receiver cable.

The shortening TEQ has shown mixed results in a multipath environment (Fig. 5.10) with a fixed cyclic prefix length on all channels: on the one hand, it boosts the effective data rate of up to 10 % on the channels with shorter impulse response (nodes 1 to 15, closer to receiver); on the other hand, the channels with longer impulse response tend to suffer from data rate degradation with the MSSNR-TEQ. The fixed constant cyclic prefix is the major reason for this behavior. The difference of the node-optimized cyclic prefix length in Fig. 5.4 compared to the calculated fixed length is increasing with the distance between the node and base station receiver. The cabling with longer segments between the branches ($l_M = 2$) has a more uniform optimum cyclic prefix distribution (see Fig. 5.11), which results in a more consistent TEQ performance over all nodes in a system with a fixed cyclic prefix length.

The data rate maximizing SIM-TEQ performs in general much better than the MSSNR-TEQ (Fig. 5.12). The performance gain of 8-10 % is more evenly distributed over the nodes. Bus systems with less interference due

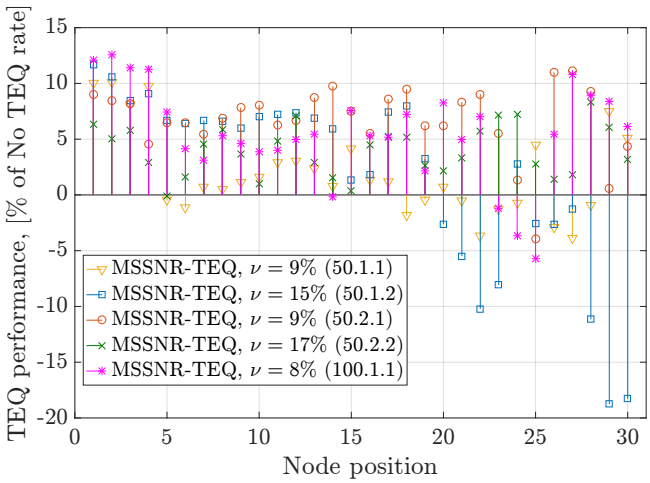


Figure 5.10: Data rate gain of MSSNR-TEQ in a 30 node bus system with constant CP, with termination, $N = 128$

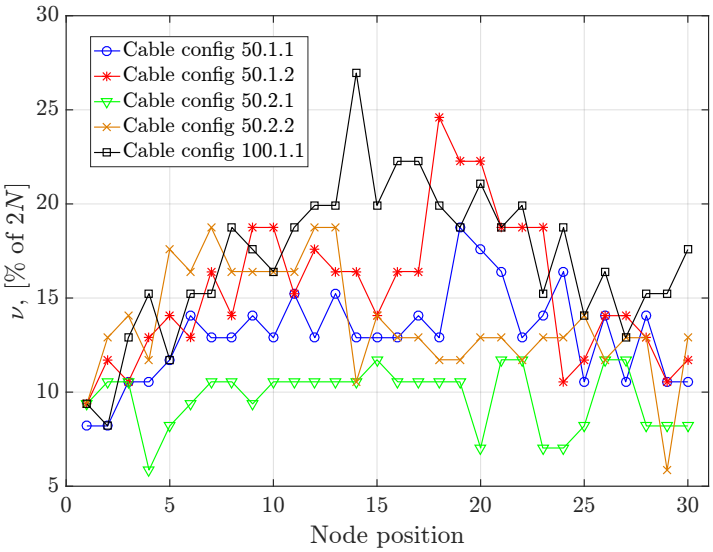


Figure 5.11: Estimated optimum cyclic prefix lengths in a 30 node bus system without TEQ, with termination, $N = 128$

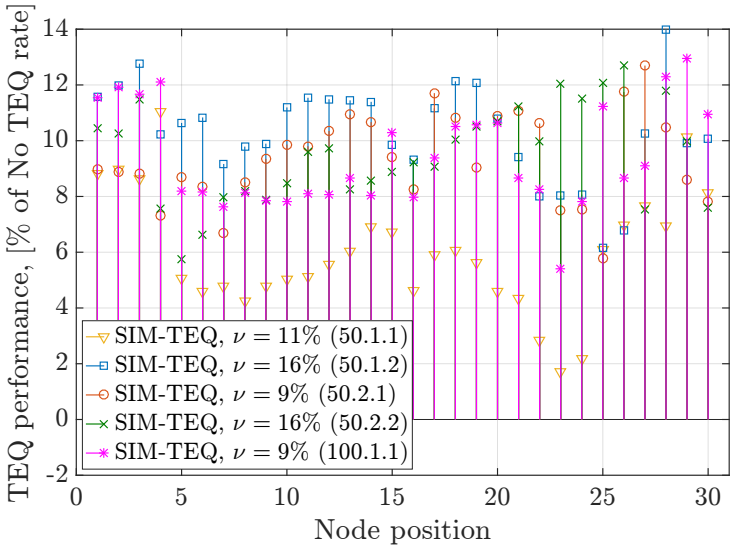


Figure 5.12: Data rate gain of SIM-TEQ in a 30 node bus system with constant CP, with termination, $N = 128$

to multi-path (50.1.1) and higher data rates do not profit much from equalization. Not surprisingly, the cabling with longer bridge taps (50.1.2) offers more gain potential for the SIM-TEQ.

Thus, a TEQ, and especially its data rate maximizing version, provides a way to increase the effective data rate. Another possibility is to utilize a larger number of carriers which results in less overhead due to cyclic prefix but also requires more hardware resources to implement the larger FFT. In a sensor network with a large number of nodes the hardware resources and power consumption of each sensor could be quite limited. Keeping in mind that the FFT is the most demanding part of the digital hardware design, it is very tempting to rather use a much easier to implement FIR filter for a TEQ to meet the data rate requirements.

In Fig. 5.13, the average gap between the system with smaller FFT with SIM-TEQ and the system with double-sized FFT without TEQ is about 5-6 %, depending on the cable configuration and node position. This is generally an acceptable performance degradation as a trade-off for a noticeable implementation complexity reduction.

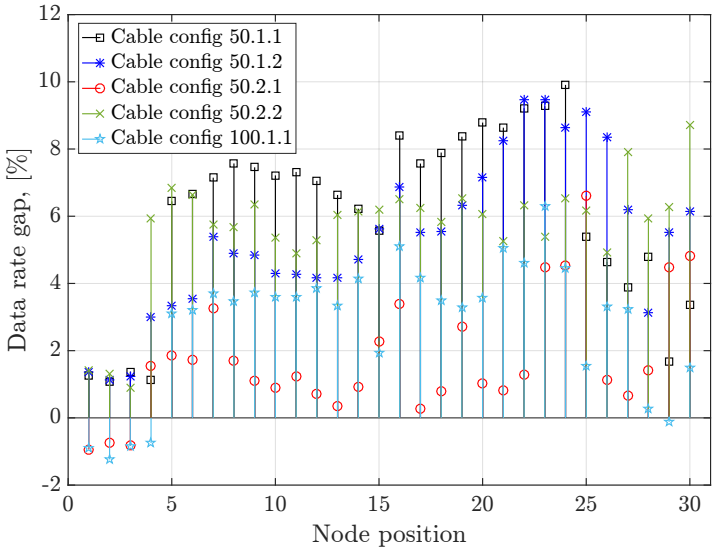


Figure 5.13: Data rate gap between SIM-TEQ enabled system, $N = 128$ and a system without TEQ and twice the FFT size (30 node bus system with constant CP, with termination)

# Chapter 6

# Multi-Carrier Twisted Pair Bus Architecture

A batch of technological insights, given in the previous chapters, provide the foundation for a new broadband DC-PLC transmission system, which will be called MC-TP. This chapter gives an overview of the practical realization of the DC-PLC concept and presents the first MC-TP transceiver (modem) design prototype in the last section.

## 6.1 Physical Layer

The MC-TP is conceptually a linear bus system (as shown in Fig 6.1) with asymmetrical up- and downstream channels. A wide bandwidth upstream channel (2-95 MHz) is shared between numerous sensors (End-Points, EP). The EPs are constantly sending (uploading) the data to a common receiver (Base Station, BS). The BS can send (download) some data to the EPs through the narrow bandwidth (0.2-1.953125 MHz) downstream channel. Both channels share the same medium (two wires in a twisted-pair cable) using frequency division duplexing (FDD).

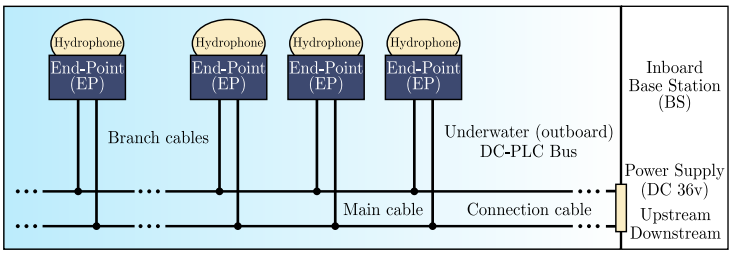


Figure 6.1: MC-TP linear bus topology

### 6.1.1 Transmission Medium

The linear bus topology in Fig. 6.1 is formed by the main and branch cable pieces (up to 2 m long), connected to the BS by a typically longer (up to 100 m) connection cable. Different types of cables can be mixed, with a requirement for twisted-pairs to correspond to category Cat5e (characteristic impedance around 100 Ω) at least. The cable bundles consist of at least two pairs, with only one being actively used and the other one reserved for future applications (backup or data rate doubling). Terminating the bus on the far end is not obligatory, but advisable. If it is used, AC-coupled termination is required, because of the DC power transmission requirements.

The multi-user multi-access upstream channel is used in TDMA mode, giving EPs equal priorities. It is not only the implementation simplicity that speaks for this solution – the passive high-impedance mode of all currently unused transceivers allows the active transceiver to achieve higher data rates due the lower bus load. The simulations show that the higher bus load can hardly be compensated in the FDMA case, when transceivers' output impedances are chosen to be static and real.

The downstream channel is a broadcast channel, with BS being the single active transmitter. This channel is actively used during the initialization phase and also to poll the EPs, if the BS is used in the bus master mode and the autonomous EP synchronization is turned off.

### 6.1.2 Modulation

It is an obvious choice to use multi-carrier modulation in the form of baseband DMT (Chapter 4) – in the frequency-selective channel of a multi-path linear bus. DMT can quite easily be adapted to any changing channel conditions (see Chapter 3 for details), achieving a high data rate at low implementation cost. Both up- and downstream channels use baseband DMT. The upstream transceiver does not use the low-frequency carriers, which are reserved for the downstream transceivers.

The lengths of the FFT (up to 2048) and the cyclic prefix are defined by estimating the longest expected channel impulse response, the system has to cope with. Incorporating a time-domain equalizer (TEQ) allows for a very short cyclic prefix, as was shown in previous chapter, and a smaller FFT – thereby saving hardware resources.

### 6.1.3 Synchronization

Both blind (using cyclic prefix redundancy) and the data-aided Schmidl-Cox method are used for symbol and sampling frequency synchronization. The data-aided method with special designed frames is responsible for the initial or course synchronization, particularly in a system with TEQ – where the cyclic prefix is very short. The blind method is used after acquiring initial synchronization, to observe and correct deviations without reducing the effective data rate.

## 6.2 Prototype Realization

The transceiver of the MC-TP prototype (see Fig. 6.2) consists of an analog and a digital front-end. The readily available integrated solutions for DSL or PLC applications do not cover the available bandwidth and currently cannot simply be adopted for a DC-PLC application in an optimum way. Hence, the analog part is build of discrete differential elements: low-noise voltage-controlled amplifier and attenuator as an input to a high-speed ADC; high voltage-swing amplifier at the output of a high-speed DAC as cable driver. The reconstruction and anti-aliasing filters are passive – which are not too complex in case of oversampling.

The prototype includes some test logic within the digital part and the analog part is made symmetrical with a possibility to switch between the upstream or downstream filter and ADC/DAC configurations on the same board. Although this design does not exploit the possible hardware complexity reduction (reserved for the next prototype), it makes the transceiver prototype more flexible to be used either at sensor (EP) or at the base station (BS) side.

### 6.2.1 Analog Front-End (AFE)

The AFE, shown in Fig. 6.2, provides an interface to the cable using a coupler, which consists of a high-pass filter and a 1:2 impedance transformer to match the characteristic impedance of the cable to other analog components. A hybrid network, connected to the transformer, ensures that the outgoing signal, amplified by the TxDriver, will not saturate the input amplifier RxLNA, which expects a rather low level signal. The interface to the digital front-end consists of the transmitter TxDAC and receiver RxADC.

The downstream DAC and ADC are used in an interpolating and oversampled way (at 15.625 MSPS or $4 - \times$ oversampling) to relax the requirements for the analog filters. This is unfortunately hard to achieve with the

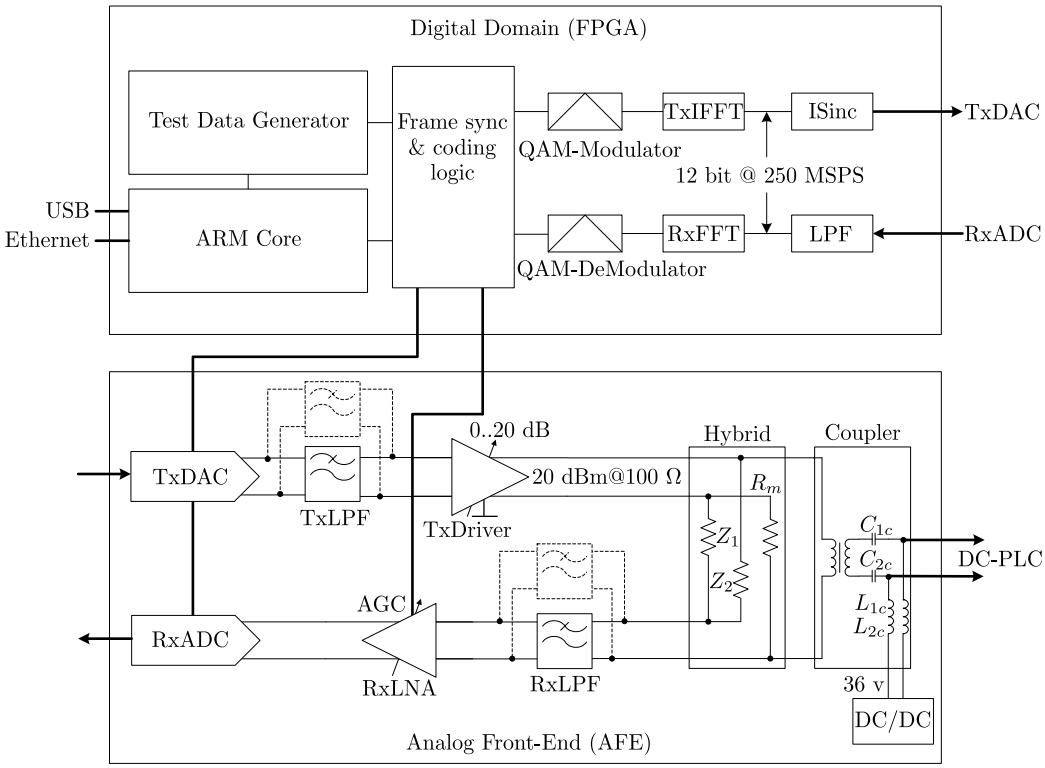


Figure 6.2: Transceiver block diagram

upstream channel (200 MSPS Nyquist rate) without very expensive components. The problem is partially solved in MC-TP system by using a higher bandwidth with a fractionally sampling frequency of 250 MHz (250 MSPS ADC, 500 MSPS DAC with $2 - \times$ oversampling) for upstream and zeroing the DMT sub-carriers over 95 MHz. Due to asymmetrical data rates (and thus also bandwidth) for downstream and upstream, the requirements for EP and BS transceivers are actually quite different: EPs have a wideband transmitter and narrow band receiver, whereas BS has a wideband receiver and a narrow band transmitter, mirroring the EP requirements. Consequently, the parameters for analog components are different for EP and BS transceivers and for the final realization are proposed to be:

- EP transceiver:
  - TxDAC: $\geq$12 bit, 500 MSPS
  - RxADC: $\geq$12 bit, 15.625 MSPS
  - TxDriver gain range: 20 dB
  - TxLPF: passband 0-95 MHz; passband ripple 0.1 dB; stopband 155 MHz; stopband attenuation 27 dB
  - RxLPF: passband 0-1.953125 MHz; passband ripple 0.1 dB; stopband 13.5 MHz; stopband attenuation 20 dB
- BS transceiver:
  - TxDAC: $\geq$12 bit, 15.625 MSPS
  - RxADC: $\geq$12 bit, 250 MSPS
  - TxDriver gain range: 20 dB
  - TxLPF: passband 0-1.953125 MHz; passband ripple 0.1 dB; stopband 13.5 MHz; stopband attenuation 80 dB
  - RxLPF: passband 0-95 MHz; passband ripple 0.1 dB; stopband 125 MHz; stopband attenuation 27 dB

As was stated above, the current prototype does not use the lower bandwidth components for the downstream, but rather supplies the high-speed DAC/ADC with lower clock and provides switches to choose the corresponding filter configuration for either EP or BS.


Figure 6.3: Transceiver prototype

### 6.2.2 Digital Back-End

The digital design is FPGA based (Xilinx ZYNQ, see Fig. 6.3), covering the tasks of digital modulation (DMT) and filtering and providing a high-speed DDR-LVDS interface to DAC and ADC. The parameters of frequency-domain QAM modulation (max. 10 bit constellations) and FFT (between 256 and 2048) and the cyclic prefix size are chosen according to the available analog components (12 bit DAC) and the channel conditions, respectively. An important part of the digital design is the frame and sampling frequency synchronization.

All high-speed functions are implemented using VHDL: QAM modulator/demodulator, iFFT/FFT, FEQ, DAC/ADC interfaces. All blocks are packed into separate IP-Cores, using Xilinx Vivado, and are interconnected by a well-known AXI-Stream interface. An ARM processor core on the FPGA fabric is used to run software, providing a simple and flexible configuration interface to the MC-TP hardware. It is also used to generate and evaluate the input/output raw data. Some system features are also part of the software package (MC-TP driver): initialization of synchronization and channel measurement runs, to name the most important.

The optional TEQ (a shortening-only MSSNR-TEQ) is implemented as a simple FIR filter, with 16 coefficients. Its configuration can be dynamically changed through a special interface, provided by the IP-Core.

# Chapter 7

# Conclusion

It is a great challenge to develop a new transmission system from scratch, even if a very solid foundation provided by the long history of communication research is at hand. This work is the first step on the way to an efficient DC-PLC sensor network – the Multi-Carrier-Twisted-Pair (MC-TP) bus. The research was structured keeping in mind a number of practical requirements, dictated by the application of an underwater network for a sonar array.

The efficiency of data transmission in an acoustical sensor network can be improved even before a single bit has found its way to the medium – by reducing the size of the original message, applying source coding. The data, generated by the acoustical sensors, was shown to be redundant. Using the methods of (audio) lossless compression, particularly linear prediction coding, a source coding scheme was introduced. The single channel linear predictor case was extended to cope with the multi-channel data, resulting from the physically combined sensors. A subexponential code was proven to be the most efficient universal variable-length code for both cases. It provides better matching of the probability distribution of the residuals, generated by the linear prediction, than the other codes. The new methods were shown to be more effective than the existing compression schemes and can achieve an average lossless compression ratio of roughly 15 % for this particular type of data. Further compression can be achieved by lossy compression methods, but this requires adaptation to the signal processing algorithms (e.g., direction-of-arrival estimation) used.

The characterization of the special channel of a PLC-like linear bus, built for the underwater application using specifically designed cables was an important part of this research work. The appropriate models for cabling, as well as for the whole bus system were introduced and the methods for determining their parameters, from measurement results, were described. The cabling in sonar systems is exposed to a quite aggressive underwater envi-

ronment, most notably high static and dynamic pressure. Its influence on the cable characteristics and on the overall transfer function in a linear bus PLC system was studied and the models were fitted accordingly to match the changes. Despite its frequency-selective nature, the investigated channel is considered to be rather well-controlled and transmission-friendly, because the topology is usually fixed and the active bus node as well as the base station are rather well impedance-matched. This is very similar to a typical channel in DSL applications, which also explains some design choices being inspired by those existing systems. The cabling is especially designed to cope with high DC currents and has low resistance and attenuation. Nevertheless, a large number of nodes (up to 100, all passive nodes have high input impedance) introduce a high level of interference due to multi-path and changing characteristic impedance of cabling under pressure. Besides, the overall insertion loss is shown to increase by roughly 10 % at high pressure of around 70 bar.

Multi-carrier modulation is known to be very efficient on frequency selective channels and is the chosen transmission scheme for the MC-TP bus, as the name suggests. Its baseband version (DMT) requires, however, a double-size FFT in the final implementation. The application of a time-domain equalizer is proposed to reduce the implementation complexity. Either solely concentrating on the reduction of the impulse response length (shortening TEQ) or directly improving the resulting data rate (rate-maximizing TEQ) reduces the required size of the cyclic prefix, its ratio to the frame size and hence increases the resulting effective data rate. The around 10 % gain in data rate can make up for losses due to a smaller FFT size, which is preferred to reduce the hardware complexity.

The above results were directly used in the MC-TP architecture specification and in the first MC-TP modem prototype implementation. In the absence of high-bandwidth integrated solutions for DC-PLC, the analog part was a complete new discrete design, while the digital part is FPGA-based. The performance of the prototype clearly exceeded the minimum requirements and shows great potential to become a standard transmission method for sonar. Besides underwater networks, especially aerospace applications can profit from reduced cabling weight and cost, keeping higher data rates. A modern microsatellite or an unmanned aerial vehicle are the best examples of such applications.

# Bibliography


[1] L. Lanbo, Z. Shengli, and C. Jun-Hong, "Prospects and problems of wireless communication for underwater sensor networks," *Wirel. Commun. Mob. Comput.*, vol. 8, pp. 977–994, Oct. 2008.

[2] "IEEE standard for Ethernet," December 2012. IEEE Std 802.3TM-2012.

[3] J. D. I. Bogdan M. Wilamowski, ed., *Industrial Communication Systems*. Taylor and Francis, 2014.

[4] S. Parkes, P. Armbruster, and M. Suess, "The spacewire on-board data-handling network," tech. rep., European Space Agency, 2011.

[5] P.-E. Eriksson and B. Odenhammar, "VDSL2: Next important broadband technology," *Ericsson Review*, 2006.

[6] H. Latchman, S. Katar, L. Yonge, and S. Gavette, *Homeplug AV and IEEE 1901: A Handbook for PLC Designers and Users*. Wiley, 2013.

[7] S. Gault, P. Ciblat, and W. Hachem, "An OFDMA based modem for powerline communications over the low voltage distribution network," in *2005 International Symposium on Power Line Communications and Its Applications*, pp. 42–46, April 2005.

[8] "HomePlug AV2 technology white paper," in *Connected Home Summits*, HomePlug Powerline Alliance, 2013.

[9] O. Elgezabal and A. Sanz, "Modeling and simulating power line communications on civil aircraft: First steps," in *2010 IEEE/AIAA 29th Digital Avionics Systems Conference (DASC)*, pp. 5.B.5–1–5.B.5–16, October 2010.

[10] J. O'Brien and A. Kulshreshtha, "Distributed and remote control of flight control actuation using power line communications," in *2008.*

*IEEE/AIAA 27th Digital Avionics Systems Conference, 2008. DASC*, pp. 1.D.4–1–1.D.4–12, October 2008.

[11] S. Dominiak, H. Widmer, M. Bittner, and U. Dersch, "A bifilar approach to power and data transmission over common wires in aircraft," in *2011 IEEE/AIAA 30th Digital Avionics Systems Conference (DASC)*, pp. 7B4–1–7B4–13, October 2011.

[12] T. Huck, J. Schirmer, T. Hogenmuller, and K. Dostert, "Tutorial about the implementation of a vehicular high speed communication system," in *2005 International Symposium on Power Line Communications and Its Applications*, pp. 162–166, April 2005.

[13] F. Nouvel and P. Tanguy, "Flexible OFDM waveform for PLC/RF in-vehicle communications," in *2012 15th Euromicro Conference on Digital System Design (DSD)*, pp. 463–468, September 2012.

[14] Y.-C. Chen, S.-H. Tsai, K.-J. Yang, P.-F. Ho, K.-F. Tseng, and H.-S. Chen, "Vehicular signal transmission using power line communications," in *Signal Information Processing Association Annual Summit and Conference (APSIPA ASC), 2012 Asia-Pacific*, pp. 1–4, December 2012.

[15] F. Nouvel and P. Tanguy, "Towards power line communication in vehicle," in *2011 XXXth URSI General Assembly and Scientific Symposium*, pp. 1–4, August 2011.

[16] E. Wade and H. Asada, "Design of a broadcasting modem for a DC PLC scheme," *IEEE/ASME Transactions on Mechatronics*, vol. 11, pp. 533–540, October 2006.

[17] D. Yang, A. Verl, S. Schmitz, and K. H. Wurst, "Implementation of a new communication system for reconfigurable mechatronic modules," in *2010 2nd International Asia Conference on Informatics in Control, Automation and Robotics (CAR)*, vol. 2, pp. 33–36, March 2010.

[18] J. A. C. Bingham, "Multicarrier modulation for data transmission: an idea whose time has come," *IEEE Communications Magazine*, vol. 28, pp. 5–14, May 1990.

[19] M. Zimmermann and K. Dostert, "A multi-path signal propagation model for the powerline channel in the high frequency range," in *ISPLC99*, 1999.

[20] J. Proakis, *Digital Communications*. Electrical engineering series, McGraw-Hill, 2001.

[21] D. Salomon and G. Motta, *Handbook of Data Compression*. Springer Publishing Company, Incorporated, 5th ed., 2009.

[22] P. S. Naidu, *Sensor Array Signal Processing, Second Edition*. Boca Raton, FL, USA: CRC Press, Inc., 2nd ed., 2009.

[23] T. Wiegand and H. Schwarz, "Source coding: Part I of fundamentals of source and video coding," *Foundations and Trends in Signal Processing*, vol. 4, no. 12, pp. 1–222, 2011.

[24] J. Makhoul, "Linear prediction: A tutorial review," *Proceedings of the IEEE*, vol. 63, pp. 561–580, April 1975.

[25] J. Benesty, M. M. Sondhi, and Y. A. Huang, *Springer Handbook of Speech Processing*. Secaucus, NJ, USA: Springer-Verlag New York, Inc., 2007.

[26] A. Papoulis and S. U. Pillai, *Probability, Random Variables, and Stochastic Processes*. McGraw-Hill Higher Education, 4 ed., 2002.

[27] T. M. Cover and J. A. Thomas, *Elements of Information Theory (Wiley Series in Telecommunications and Signal Processing)*. Wiley-Interscience, 2006.

[28] K. Sayood, ed., *Lossless Compression Handbook*. Communications, Networking and Multimedia, San Diego: Academic Press, 2003.

[29] S. Golomb, "Run-length encodings," *IEEE Transactions on Information Theory*, vol. IT-12, pp. 399–401, July 1966.

[30] R. Rice, "Some practical universal noiseless coding techniques," *JPL Publication 79-22*, March 1979.

[31] A. B. Kiely, "Selecting the Golomb parameter in Rice coding," *IPN Progress Report*, vol. 42-159, Nov. 2004.

[32] J. Teuhola, "A compression method for clustered bit-vectors," *Information Processing Letters*, vol. 7, no. 6, pp. 308–311, 1978.

[33] A. Said, "On the determination of optimal parameterized prefix codes for adaptive entropy coding," in *2005 Data Compression Conference, Snowbird*, March 2005.

[34] E. R. Fiala and D. H. Greene, "Data compression with finite windows," *Commun. ACM*, vol. 32, pp. 490–505, Apr. 1989.

[35] S. Pigeon, "Start/stop codes," in *2001 Data Compression Conference (DCC 01)*, p. 511, 2001.

[36] L. Bin and M. Qinggang, "An improved spiht wavelet transform in the underwater acoustic image compression," in *Proceedings of 2013 2nd International Conference on Measurement, Information and Control*, vol. 02, pp. 1315–1318, Aug 2013.

[37] D. H. Kil and F. B. Shin, "Reduced dimension image compression for remotely distributed underwater signal processing," in *OCEANS '95. MTS/IEEE. Challenges of Our Changing Global Environment. Conference Proceedings.*, vol. 2, pp. 1183–1188, Oct 1995.

[38] W. Chen, F. Yuan, and E. Cheng, "Adaptive underwater image compression with high robust based on compressed sensing," in *2016 IEEE International Conference on Signal Processing, Communications and Computing (ICSPCC)*, pp. 1–6, Aug 2016.

[39] L. S. Wong, G. E. Allen, and B. L. Evans, "Sonar data compression using non-uniform quantization and noise shaping," in *2014 48th Asilomar Conference on Signals, Systems and Computers*, pp. 1895–1899, Nov 2014.

[40] A. Chybicki, M. Moszynski, and P. Pocwiardowski, "Applications of compression techniques for reducing the size of multibeam sonar records," in *2008 1st International Conference on Information Technology*, pp. 1–4, May 2008.

[41] S. Gazor and W. Zhang, "Speech probability distribution," *IEEE Signal Processing Letters*, vol. 10, pp. 204–207, July 2003.

[42] V. K. Goyal, "Theoretical foundations of transform coding," *IEEE Signal Processing Magazine*, vol. 18, pp. 9–21, Sep 2001.

[43] B. E. Usevitch, "A tutorial on modern lossy wavelet image compression: foundations of JPEG 2000," *IEEE Signal Processing Magazine*, vol. 18, pp. 22–35, Sep 2001.

[44] M. D. Adams and F. Kossentni, "Reversible integer-to-integer wavelet transforms for image compression: performance evaluation and analysis," *IEEE Transactions on Image Processing*, vol. 9, pp. 1010–1024, Jun 2000.

[45] M. F. Schilling, A. E. Watkins, and W. Watkins, "Is human height bimodal?," *The American Statistician*, vol. 56, no. 3, pp. 223–229, 2002.

[46] R. Orta, "Lecture notes on transmission line theory." Department of Electronics, Politecnico di Torino, March 2012.

[47] S. J. Orfanidis, *Electromagnetic Waves and Antennas*. ECE Department, Rutgers University, 2013.

[48] G. H. Owyang, *Review of Transmission Line Theory*. Springer New York, 1989.

[49] P. Boets, M. Zekri, and L. V. Biesen, "On the identification of cables for metallic access networks," in *IEEE Instrumentation and Measurement Technology Conference*, 2001.

[50] J. Zhang, J. Drewniak, D. Pommerenke, M. Koledintseva, R. DuBroff, W. Cheng, Z. Yang, Q. Chen, and A. Orlandi, "Causal RLGC($f$) models for transmission lines from measured $S$-parameters," *IEEE Transactions on Electromagnetic Compatibility*, vol. 52, pp. 189–198, February 2010.

[51] R. F. van den Brink, "Cable reference models for simulating metallic access networks," tech. rep., ETSI, 1998.

[52] P. Boets and L. V. Biesen, "Metallic 2-wire parametric line models, a survey," in *XVIII Imeko World Congress*, 2006.

[53] J. M. L. Heylen, "Cable models predict physically impossible behaviour in time domain," in *ETSI TM6 Meeting, Amsterdam*, November 1999.

[54] J. Musson, "Maximum likelihood estimation of the primary parameters of twisted pait cables," tech. rep., Marconi S.p.A., 1998.

[55] F. Lindqvist, P. O. Börjesson, P. Ödling, S. Hst, K. Eriksson, and T. Magesacher, "Low-order and causal twisted-pair cable modeling by means of the Hilbert transform," *MMWP08/RVK08, 2008-06-09/11*, 2008.

[56] K. Lu, "An efficient method for analysis of arbitrary nonuniform transmission lines," *IEEE Transactions on Microwave Theory and Techniques*, vol. 45, pp. 9–14, January 1997.

[57] M. M. Al-Asadi, A. Duffy, K. Hodge, and A. Willis, "Analysis and modelling of structured wiring communication channels," *IEEE Proceedings - Science, Measurement and Technology*, vol. 148, pp. 129–136, May 2001.

[58] T. Nordström, "A model for an Austrian PE04 cable," 2003.

[59] P. J. Rousseeuw, "Least median of squares regression," *Journal of the American Statistical Association*, 1984.

[60] C. Tofallis, "Least squares percentage regression," *Journal of Modern Applied Statistical Methods*, 2009.

[61] J. Fox, *Robust Regression*, 2002. Appendix to an R and S-PLUS Companion to applied regression.

[62] M. Zimmermann and K. Dostert, "A multipath model for the powerline channel," *IEEE Transactions on Communications*, vol. 50, pp. 553–559, April 2002.

[63] T. Banwell and S. Galli, "A new approach to the modeling of the transfer function of the power line channel," in *International Symposium on Power Line Communications and its Applications, ISPLC 2001*, pp. 4–6, 2001.

[64] T. Banwell and S. Galli, "On the symmetry of the power line channel," in *International Symposium on Power Line Communications and its Applications, ISPLC 2001*, pp. 325–330, 2001.

[65] A. Rennane, C. Konate, and M. Machmoum, "A simplified deterministic approach for accurate modeling of the indoor power line channel," in *ICSNC'08 3rd International Conference on Systems and Networks Communications*, pp. 121–126, October 2008.

[66] P. J. Pupalaikis, "The relationship between discrete-frequency *S*-parameters and continuous-frequency responses," in *DesignCon 2012*, 2012.

[67] S. Huss and J. Bennett, "An efficient model for twisted-pair cables with discontinuities and stubs for discrete time simulations," in *The 2001 IEEE International Symposium on Circuits and Systems*, vol. 4, pp. 254–257, May 2001.

[68] B. Tan and J. Thompson, "Powerline communications channel modelling methodology based on statistical features," *CoRR*, vol. abs/1203.3879, 2012.

[69] Agilent, "Understanding the fundamental principles of vector network analysis," tech. rep., Agilent Technologies, 2012.

[70] Agilent, "10 hints for making better network analyzer measurements," tech. rep., Agilent Technologies, 2001.

[71] T. Magesacher, W. Henkel, G. Tauböck, and T. Nordström, "Cable measurements supporting future DSL technologies," *ÖVE-Zeitschrift E & I*, Feb. 2002.

[72] E. J. Brito, "A methodology for measurements of the ADSL copper loop parameters," in *VI International Telecommunications Symposium (ITS2006)*, 2006.

[73] L. Cepa, M. Kozak, and J. Vodrazka, "Innovation of methods for measurement and modelling of twisted pair parameters," *Information and Communication Technologies and Services*, vol. 9, no. 5, 2011.

[74] "Commercial building telecommunications cabling standard TIA/EIA-568-B.2," May 2001. Part 2: Balanced Twisted-Pair Cabling Components.

[75] J. Nelder and R. Mead, "A simplex method for function minimization," *The Computer Journal*, 1965.

[76] A. C. Cameron and F. A. Windmeijer, "An $R$-squared measure of goodness of fit for some common nonlinear regression models," *Journal of Econometrics*, 1997.

[77] Agilent, "De-embedding and embedding $S$-Parameter networks using a vector network analyzer. Application note 1364-1," tech. rep., Agilent Technologies, 2006.

[78] D. Rytting, "Network analyzer error models and calibration methods," tech. rep., Agilent Technologies, 2010.

[79] K. Silvonen, H. Zhu, and Y. Liu, "A 16-term error model based on linear equations of voltage and current variables," *IEEE Transactions on Microwave Theory and Techniques*, Apr. 2006.

[80] T. Starr, J. M. Cioffi, and P. J. Silverman, *Understanding Digital Subscriber Line Technology*. Prentice Hall PTR, 1999.

[81] H. Meng, Y. Guan, and S. Chen, "Modeling and analysis of noise effects on broadband power-line communications," *IEEE Transactions on Power Delivery*, vol. 20, pp. 630–637, April 2005.

[82] R. Hashmat, P. Pagani, A. Zeddam, and T. Chonavel, "MIMO communications for inhome PLC networks: Measurements and results up to 100 MHz," in *2010 IEEE International Symposium on Power Line Communications and Its Applications (ISPLC)*, pp. 120–124, March 2010.

[83] M. Antoniali, M. De Piante, and A. Tonello, "PLC noise and channel characterization in a compact electrical car," in *2013 17th IEEE International Symposium on Power Line Communications and Its Applications (ISPLC)*, pp. 29–34, March 2013.

[84] V. Degardin, M. Lienard, P. Degauque, E. Simon, and P. Laly, "Impulsive noise characterization of in-vehicle power line," *IEEE Transactions on Electromagnetic Compatibility*, vol. 50, pp. 861–868, November 2008.

[85] J. Cortés, M. Cerdá, L. Díez, and F. Cañete, "Analysis of the periodic noise on in-vehicle broadband power line channels," in *2012 16th IEEE International Symposium on Power Line Communications and Its Applications (ISPLC)*, pp. 334–339, March 2012.

[86] S. Barmada, M. Raugi, M. Tucci, and T. Zheng, "Power line communication in a full electric vehicle: Measurements, modelling and analysis," in *2010 IEEE International Symposium on Power Line Communications and Its Applications (ISPLC)*, pp. 331–336, March 2010.

[87] F. Grassi, S. Pignari, and J. Wolf, "Channel characterization and EMC assessment of a PLC system for spacecraft DC differential power buses," *IEEE Transactions on Electromagnetic Compatibility*, vol. 53, pp. 664–675, August 2011.

[88] M. Tlich, P. Pagani, and G. Avril, "ICT-213311 OMEGA report: PLC channel characterization and modelling," 2009.

[89] S. Galli, T. Banwell, and D. Waring, "Power line based LAN on board the NASA Space Shuttle," in *IEEE 59th Vehicular Technology Conference*, vol. 2, pp. 970–974, May 2004.

[90] V. Raghav, V. Gowtham, H. Jamadagni, and T. Prabhakar, "Data throughput maximization for broadband over Power Line," in *2014 Sixth International Conference on Communication Systems and Networks (COMSNETS)*, pp. 1–6, January 2014.

[91] D. J. G. Mestdagh, P. Spruyt, and B. Biran, "Analysis of clipping effect in DMT-based ADSL systems," in *IEEE International Conference on Communications, 1994. ICC '94*, vol. 1, pp. 293–300, May 1994.

[92] T. Araujo and R. Dinis, "Performance evaluation of quantization effects on multicarrier modulated signals," *IEEE Transactions on Vehicular Technology*, vol. 56, pp. 2922–2930, September 2007.

[93] D. Dardari, "Joint clip and quantization effects characterization in OFDM receivers," *IEEE Transactions on Circuits and Systems I: Regular Papers*, vol. 53, pp. 1741–1748, August 2006.

[94] D. Langford, B. Tesch, B. Williams, G. Nelson, R. Ross, G. Bechtel, and M. Lewis, "A BiCMOS analog front-end circuit for an FDM-based ADSL system," in *1997. Proceedings of the Bipolar/BiCMOS Circuits and Technology Meeting*, pp. 180–182, September 1997.

[95] D. Tse and P. Viswanath, *Fundamentals of Wireless Communication*. New York, NY: Cambridge University Press, 2005.

[96] T. J. Starr, J. M. Cioffi, and P. Silverman, *Understanding Digital Subscriber Line Technology*. Prentice Hall, 1999.

[97] P. Golden, H. Dedieu, and K. S. Jacobsen, *Fundamentals of DSL Technology*. Auerbach Publications, 2004.

[98] J. Cioffi, *EE379C Course Notes*. Stanford University, 2000.

[99] J. Tan and G. Stuber, "Constant envelope multi-carrier modulation," in *MILCOM 2002. Proceedings*, vol. 1, pp. 607–611, October 2002.

[100] P. Tan and N. Beaulieu, "A comparison of DCT-based OFDM and DFT-based OFDM in frequency offset and fading channels," *IEEE Transactions on Communications*, vol. 54, pp. 2113–2125, November 2006.

[101] L. Goldfeld, V. Lyandres, and D. Wulich, "Minimum BER power loading for OFDM in fading channel," *IEEE Transactions on Communications*, vol. 50, pp. 1729–1733, November 2002.

[102] K. Al-Mawali, A. Sadik, and Z. Hussain, "Simple discrete bit-loading for OFDM systems in power line communications," in *2011 IEEE International Symposium on Power Line Communications and Its Applications (ISPLC)*, pp. 267–270, April 2011.

[103] E. Bedeer, O. Dobre, M. Ahmed, and K. Baddour, "Joint optimization of bit and power loading for multicarrier systems," *Wireless Communications Letters*, vol. 2, pp. 447–450, August 2013.

[104] A. Garcia-Armada, "SNR gap approximation for $M$-PSK-based bit loading," *IEEE Transactions on Wireless Communications*, vol. 5, pp. 57–60, January 2006.

[105] P. S. Chow, "Bandwidth optimized digital transmission techniques for spectrally shaped channels with impulse noise, PhD thesis," 1993.

[106] P. Chow, J. Cioffi, and J. A. C. Bingham, "A practical discrete multitone transceiver loading algorithm for data transmission over spectrally shaped channels," *IEEE Transactions on Communications*, vol. 43, pp. 773–775, February 1995.

[107] D. Hughes-Hartogs, "Ensemble modem structure for imperfect transmission media," 1989.

[108] J. Campello, "Practical bit loading for DMT," in *1999. ICC '99. 1999 IEEE International Conference on Communications*, vol. 2, pp. 801–805, 1999.

[109] A. M. Wyglinski, F. Labeau, and P. Kabal, "An efficient bit allocation algorithm for multicarrier modulation," in *2004. WCNC. 2004 IEEE Wireless Communications and Networking Conference*, vol. 2, pp. 1194–1199, March 2004.

[110] L. Piazzo, "Optimal fast algorithm for power and bit allocation in OFDM systems," *IEEE Transactions on Vehicular Technology*, vol. 60, pp. 1263–1265, March 2011.

[111] A. Mahmood and J. C. Belfiore, "An efficient algorithm for optimal discrete bit-loading in multicarrier systems," *IEEE Transactions on Communications*, vol. 58, pp. 1627–1630, June 2010.

[112] K. S. Hassan, *Unequal Error Protection Adaptive Modulation in Multicarrier Systems*. Shaker Verlag, 2010.

[113] R. Bauml, R. F. H. Fischer, and J. Huber, "Reducing the peak-to-average power ratio of multicarrier modulation by selected mapping," *Electronics Letters*, vol. 32, pp. 2056–2057, October 1996.

[114] J. Tellado and J. M. Cioffi, "PAR reduction in multicarrier transmission systems," *ANSI Document, T1E1.4 Technical Subcommittee*, vol. 4, pp. 97–367, 1998.

[115] W. Henkel and V. Zrno, "PAR reduction revisited: An extension to tellado's method," 6th International OFDM-Workshop, 2001.

[116] W. Henkel, A. Wakeel, and M. Taseska, "Peak-to-average ratio reduction with Tone Reservation in multi-user and MIMO OFDM," in *1st IEEE International Conference on Communications in China (ICCC)*, pp. 372–376, August 2012.

[117] C. Williams, M. Beach, and S. McLaughlin, "Robust OFDM timing synchronisation," in *2006. VTC 2006-Spring. IEEE 63rd Vehicular Technology Conference*, vol. 4, pp. 1947–1950, May 2006.

[118] H. Minn, V. Bhargava, and K. Letaief, "A robust timing and frequency synchronization for OFDM systems," *IEEE Transactions on Wireless Communications*, vol. 2, pp. 822–839, July 2003.

[119] T. Schmidl and D. Cox, "Robust frequency and timing synchronization for OFDM," *IEEE Transactions on Communications*, vol. 45, pp. 1613–1621, December 1997.

[120] D. Lee and K. Cheun, "Coarse symbol synchronization algorithms for OFDM systems in multipath channels," *IEEE Communications Letters*, vol. 6, pp. 446–448, October 2002.

[121] J.-J. van de Beek, M. Sandell, and P. Borjesson, "ML estimation of time and frequency offset in OFDM systems," *IEEE Transactions on Signal Processing*, vol. 45, pp. 1800–1805, July 1997.

[122] D. Landstrom, S. Wilson, J.-J. van de Beek, P. Odling, and P. Borjesson, "Symbol time offset estimation in coherent OFDM systems," in *1999. ICC '99. 1999 IEEE International Conference on Communications*, vol. 1, pp. 500–505, 1999.

[123] H. Zhou, A. Malipatil, and Y.-F. Huang, "Synchronization issues in OFDM systems," in *IEEE Asia Pacific Conference on Circuits and Systems, 2006 (APCCAS 2006)*, pp. 988–991, December 2006.

[124] T. Keller, L. Piazzo, P. Mandarini, and L. Hanzo, "Orthogonal frequency division multiplex synchronization techniques for frequency-selective fading channels," *IEEE Journal on Selected Areas in Communications*, vol. 19, pp. 999–1008, June 2001.

[125] M. Speth, F. Classen, and H. Meyr, "Frame synchronization of OFDM systems in frequency selective fading channels," in *IEEE 47th Vehicular Technology Conference, 1997*, vol. 3, pp. 1807–1811, May 1997.

[126] B. Eghbalkhah, B. Bornoosh, Z. Amini-Sheshdeh, and A. Afzali-Kusha, "A new preamble-less timing synchronization method for OFDM systems under multi-path channels," in *2007. DTIS. International Conference on Design Technology of Integrated Systems in Nanoscale Era*, pp. 196–199, September 2007.

[127] M. Speth, S. Fechtel, G. Fock, and H. Meyr, "Optimum receiver design for OFDM-based broadband transmission: A case study," *IEEE Transactions on Communications*, vol. 49, pp. 571–578, April 2001.

[128] D. Falconer and F. Magee, "Adaptive channel memory truncation for maximum likelihood sequence estimation," *The Bell System Technical Journal*, vol. 52, pp. 1541–1562, November 1973.

[129] M. Van Bladel and M. Moeneclaey, "Time-domain equalization for multicarrier communication," in *1995. Conference record. Communication Theory Mini-Conference, GLOBECOM '95., IEEE Global Telecommunications Conference*, pp. 167–171, November 1995.

[130] B. Berriah, M. Bouziani, and S. Elahmar, "New blind, adaptive channel shortening TEQ for multicarrier modulation systems," *IET Communications*, vol. 8, pp. 210–216, January 2014.

[131] N. Al-Dhahir and J. Cioffi, "Optimum finite-length equalization for multicarrier transceivers," in *IEEE Global Telecommunications Conference, 1994. GLOBECOM '94. Communications*, vol. 3, pp. 1884–1888, Nov 1994.

[132] W. Henkel and T. Kessler, "Maximizing the channel capacity of multicarrier transmission by suitable adaptation of the time-domain equalizer," *IEEE Transactions on Communications*, vol. 48, pp. 2000–2004, December 2000.

[133] P. Melsa, R. Younce, and C. Rohrs, "Impulse response shortening for discrete multitone transceivers," *IEEE Transactions on Communications*, vol. 44, pp. 1662–1672, December 1996.

[134] R. Martin, K. Vanbleu, M. Ding, G. Ysebaert, M. Milosevic, B. Evans, M. Moonen, and C. Johnson, "Unification and evaluation of equalization structures and design algorithms for discrete multitone modulation systems," *IEEE Transactions on Signal Processing*, vol. 53, pp. 3880–3894, October 2005.

[135] J. Chow and J. Cioffi, "A cost-effective maximum likelihood receiver for multicarrier systems," in *IEEE International Conference on Communications, 1992. ICC '92, SUPERCOMM/ICC '92, Discovering a New World of Communications*, vol. 2, pp. 948–952, June 1992.

[136] M. Milosevic, L. F. C. Pessoa, B. L. Evans, and R. Baldick, "DMT bit rate maximization with optimal time domain equalizer filter bank architecture," in *Conference on Signals, Systems and Computers, 2002. Conference Record of the Thirty-Sixth Asilomar*, vol. 1, pp. 377–382, Nov 2002.

[137] G. Leus, I. Barhumi, and M. Moonen, "Per-tone equalization for MIMO-OFDM systems," in *Conference on Communications, 2003. ICC '03. IEEE International*, vol. 4, pp. 2345–2349, May 2003.

[138] W. Henkel, G. Tauböck, P. Ödling, P. O. Borjesson, and N. Petersson, "The cyclic prefix of OFDM/DMT - an analysis," in *International Zürich Seminar on Broadband Communications, 2002. Access, Transmission, Networking. 2002*, pp. 22–1–22–3, 2002.

# Glossary

**$S$-parameters** are scattering parameters, used to model a two-port network in terms of incident and reflected waves

**ABCD-parameters** are chain (or cascade) parameters, used to model a two-port network in terms of input and output voltages and currents

**balun** is a balanced/unbalanced converter, using a high-frequency transformer

**OST-calibration** is a calibration method, using open, short, and termination standards

# Acronyms

**A/D** Analog-to-Digital

**AC** alternating current

**ADSL** Asymmetric Digital Subscriber Line

**AWG** American wire gauge

**AWGN** Additive White Gaussian Noise

**BC** Broadcast Channel

**BER** bit-error ratio

**BNC** Bayonet Neill-Concelman connector

**BPSK** Binary Phase Shift Keying

**BS** Base Station

**CDMA** Code-Division Multiple Access

**D/A** Digital-to-Analog

**DC** direct current

**DCT** Discrete Cosine Transform

**DFT** Discrete Fourier Transform

**DMT** Discrete Multi-Tone modulation

**DUT** Device Under Test

**EL-FEXT** Equal-Level Far-End Crosstalk

**EMI** Electro Magnetic Interference

**EP** End-Point

**FDMA** Frequency-Division Multiple Access

**FEQ** Frequency-domain Equalizer

**FEXT** Far-End Crosstalk

**FFT** Fast Fourier Transform

**FIR** Finite-Impulse Response

**HF** High-Frequency

**IDCT** Inverse Discrete Cosine Transform

**IDFT** Inverse Discrete Fourier Transform

**IL** Insertion Loss

**ISI** Inter-Symbol Interference

**LMS** Least Median of Squares

**LSP** Least Squares Percentage

**LTE** Long-Term Evolution

**M-LVDS** Multipoint Low-Voltage Differential Signalling

**MAC** Multiple Access Channel

**MAPE** Mean Absolute Percentage Error

**MC-TP** Multi-Carrier Twisted Pair

**MIMO** Multiple-Input Multiple-Output

**ML** Maximum Likelihood

**MMSE** Minimum Mean-Squared Error

**NEXT** Near-End Crosstalk

**OFDM** Orthogonal Frequency Division Multiplexing

**OFDMA** Orthogonal Frequency Division Multiple Access

**OLS** Ordinary Least-Squares

**OSI** Open Systems Interconnection model

**PAM** Pulse Amplitude Modulation

**PAR** Peak-to-Average Ratio

**PHY** Physical Interface

**PLC** Power-Line Communication

**PSD** Power Spectral Density

**PSK** Phase Shift Keying

**QAM** Quadrature Amplitude Modulation

**RL** Return Loss

**RMS** Root Mean Square

**SER** symbol error ratio

**SMD** Surface-Mount Technology

**SNR** Signal-to-Noise Ratio

**SOLT** Short-Open-Load-Through

**SVD** Singular Value Decomposition

**TDMA** Time-Division Multiple-Access

**TEM** Transverse Electro-Magnetic (wave)

**TEQ** Time-domain Equalizer

**VCO** Voltage-Controlled Oscillator

**VDSL** Very High Speed Digital Subscriber Line

**VNA** Vector Network Analyser